LEIBNIZ-INSTITUT FÜR ATMOSPHÄREN PHYSIK IAP

An Idealized Radiative Transfer Scheme for Use in an Atmospheric General Circulation Model From the Surface up to the Mesopause Region

von
Rahel Knöpfel, geb. am 20.10.1975 in Thun, Schweiz

Dieser Forschungsbericht wurde als Dissertation von der
Mathematisch-Naturwissenschaftlichen Fakultät der Universität Rostock
angenommen

Gutachter: Prof. Dr. Erich Becker (Universität Rostock)
Prof. Dr. Ulrich Achatz (Johann Wolfgang Goethe-Universität Frankfurt am Main)

eingereicht am: 29.06.2011
verteidigt am: 11.11.2011

urn:nbn:de:gbv:28-diss2011-0172-7

Contents

Abstract

The main purpose of this work is to develop a new continuous radiation scheme of medium complexity for use in atmospheric general circulation models. In addition the primitive equations and the radiative transfer equation, which are solved by such models, are derived in a unified manner from statistical mechanics and therewith put into a broader theoretical and conceptual framework. The radiation parameterization consists of each one set of idealized transfer equations for the long-wave and short-wave regime. These transfer equations extend continuously from the surface up to the lower thermosphere, including deviations from the gray limit and local thermodynamic equilibrium in the long-wave regime, as well as the complete surface energy budget. The strategy is to account for the fundamental differences between the troposphere and middle atmosphere with regard to the radiative transfer problem in a general and straight-forward fashion, i.e., by one set of transfer equations that holds for the entire altitude range. This new approach avoids the calculation of complicated transmission functions and allows to obtain radiative fluxes and heating rates at the same high numerical resolution that is applied for the dynamics of the model. Applying the new radiation scheme in a mechanistic general circulation model together with prescribed concentrations of the radiatively active constituents shows quite reasonable results. The north-south asymmetry in planetary wave sources is found to be a plausible explanation for the pronounced annual cycle of the radiation budget at the top of the atmosphere that is seen in the model. In the vicinity of the summer mesopause, doubling the CO_2 amount leads to an upward shift of the residual circulation which counteracts the raditively induced positive temperature change.

Zusammenfassung

Hauptziel dieser Arbeit ist die Entwicklung einer neuen Strahlungsparametrisierung mittlerer Komplexität für die Anwendung in globalen atmosphärischen Zirkulationsmodellen. Um den Gültigkeitsbereich solcher Modelle aufzuzeigen, wurden die hydrodynamischen Gleichungen sowie die Strahlungstransfergleichung aus der statistischen Physik hergeleitet und in einem allgemeineren theoretischen Zusammenhang betrachtet. Die neue Strahlungsparameterisierung setzt sich zusammen aus jeweils einem System von Transfergleichungen für den langwelligen und den kurzwelligen Frequenzbereich. Für die langwellige Strahlung werden Abweichungen vom lokalen thermodynamischen Gleichgewicht und vom grauen Grenzfall allgemein berücksichtigt und die Bodenenergiebilanz wird mitberechnet. Das neue Konzept der Strahlungsparametirisierung ist, mit nur einem einzigen Satz von Transfergleichungen, der für den gesamten Höhenbereich gültig ist, die grundsätzlich unterschiedlichen physikalischen Prozesse und Bedingungen in der Troposphäre und der mittleren Atmosphäre zu beschreiben. So kann auf die sonst übliche Auswertung von komplizierten Transmissionsfunktionen verzichtet werden und die Strahlungsflüsse und Heizraten können mit derselben hohen numerischen Auflösung, die für die Dynamik verwendet wird, berechnet werden. Erste Anwendungen der neuen Strahlungsparameterisierung in einem mechanistischen Modell mit vorgeschriebenen Absorberkonzentrationen zeigen vielversprechende Resultate. Der aus ersten Simulationen erhaltene Jahresgang der Ernergiebilanz an der Atmosphärenobergrenze kann mit der Nord-Südasymmetrie der planetaren Wellen in der Troposphäre erklärt werden. Bei einer Verdoppelung des CO_2-Gehaltes verschiebt sich die residuelle Zirkulation im Bereich der Sommermesopause nach oben und wirkt damit der positiven strahlungsbedingten Temperaturänderung entgegen.

Chapter 1

Introduction

In this work, a new radiation parameterization is presented to extend the concept of physically consistent modeling of atmospheric processes using mechanistic general circulation models (GCMs) to new areas of application. To correctly extract the relevant physical mechanisms that determine the dynamical behavior or other phenomena observed in the atmosphere, it is of paramount importance that the conservation laws for mass, energy, linear and angular momentum are preserved by the methods chosen to numerically solve the governing equations and the parameterizations of physical processes. In order to consistently study coupling processes between distinct regions of the atmosphere, it is indispensable that the parameterizations for different processes are applied to the whole model domain and accommodate self-consistently the prevailing thermodynamic and dynamical state of the atmosphere at any time. In addition, to correctly simulate the interactions between processes of different kinds and scales, all physical parameterizations should be calculated using the same numerical resolution and time step that is applied to solve the dynamical equations. Finally, to facilitate high resolution simulations, a numerically efficient implementation of the physical parameterizations is needed. Due to the fact that existing comprehensive radiation schemes applied in middle atmospheric general circulation models do not conform to the aforementioned requirements [Richter et al., 2008; Garcia et al., 2007; Schmidt et al., 2006; Wehrbein and Leovy, 1982; Fomichev et al., 2002; Collins et al., 2004; Fomichev and Blanchet, 1998; Roeckner et al., 2003], a new concept to parameterize radiative transfer in atmospheric circulation models is designed and validated in this work.

In the remainder of this introduction, a general motivation for using numerical models in atmospheric sciences is given first. Then, the importance of radiative processes for the climate system as a whole and the atmosphere in particular is discussed and the vertical structure of the atmosphere is explained. In the last section of this chapter, previous studies applying the mechanistic model concept are discussed and an overview of the new radiation scheme is presented.

1.1 General circulation models in studies of the atmosphere

Earth's atmosphere is a complex and complicated physical system composed of a huge number of gaseous, liquid, and solid constituents. It's thermodynamic state and dynamical evolution are determined by a large number of physical processes and interactions. Conversely to other more manageable physical systems that can be studied by doing systematic experiments and whose state can be fully characterized by measurements, the situation concerning the atmosphere is very different. Since the state of the atmosphere and the presence and strength of

the different forcing mechanisms can not be controlled directly, systematic experimental tests to understand the relevant processes governing the observed behavior of the atmosphere are not feasible. Only limited parts of the atmospheric flow can be reconstructed by laboratory experiments. For example, baroclinic flow leading to the succession of high and low pressure systems, as observed in the middle latitudes, can be simulated by rotating cylindrical annuli experiments [Hignett et al., 1985]. In these experiments, the differential diabatic heating leading to baroclinic instability is imitated by maintaining artificially a radial temperature gradient. An additional problem in studies of the atmosphere is raised by the very inhomogeneous spatial and temporal data coverage by measurements. Considering the geographical distribution of available meteorological data one finds that the southern hemisphere, the polar regions, and large parts of the oceans are poorly covered, depending on the measurement method considered [ECMWF, 2010].

Concerning the middle and upper atmosphere data from in-situ measurements are expensive and sparsely distributed due to the fact that the instruments must be deployed by launching sounding rockets. Known techniques for such measurements are for example inflatable spheres, ionization gauges or optical methods such as photometers to investigate the neutral atmosphere or Langmuir sondes and Farraday cups to probe the ionosphere. Remote sensing techniques such as lidars, different instruments mounted on satellites or ionosondes, riometers and radars to probe the ionosphere can achieve a broader data coverage but have their own limitations [Schunk and Nagy, 2001].

To overcome the specific difficulties mentioned in studying the atmosphere, general circulation models (hereafter: GCMs) are indispensable tools. Depending on the problem that is to be solved, atmospheric GCMs can be subdivided into comprehensive models, which constitute the basis for numerical weather prediction and climate simulations, and into mechanistic (or conceptual) models, whose purpose is to gain insight into the relevant physical and dynamical processes that govern the observed properties of the atmosphere. Comprehensive GCMs generally consist of a so-called dynamical core to solve an appropriate version of the hydrodynamical equations [Simmons and Burridge, 1981] and are completed by parameterizations for non-resolved scales such as turbulent diffusion e.g. [Becker, 2003a; Becker and Burkhardt, 2007], and convection [Scinocca and McFarlane, 2004], as well as for physical processes such as phase transitions [Tiedke, 1988] and radiative transfer [Thomas and Stamnes, 2002]. Particularly the radiation parameterization consumes most of the computation time of a comprehensive GCM [Roeckner et al., 2003]. Mechanistic models usually consist of a dynamical core equivalent to that of a comprehensive model, but the additional parameterizations are more or less simplified. This leads to the advantage that the effects of the parameterized physical processes can be clearly separated. Thus, by doing "numerical experiments" it is possible to extract the most relevant physical mechanism and coupling processes needed to explain certain phenomena. In addition, mechanistic models constitute an ideal playground for testing new physical parameterizations before implementing them in comprehensive GCMs. Due to the often better numerical performance of a mechanistic compared to a comprehensive model, it is possible using higher numerical resolution to explicitly resolve small-scale processes such as the interaction between the mesoscale dynamics and the mean flow [Koshyk and Hamilton, 2000; Hamilton and Ohfuchi, 2008] or the radiation field, applying a simplified model concept [Fels, 1982, 1984; Zhu and Strobel, 1991; Zhu, 1993; Imamura and Ogawa, 1995].

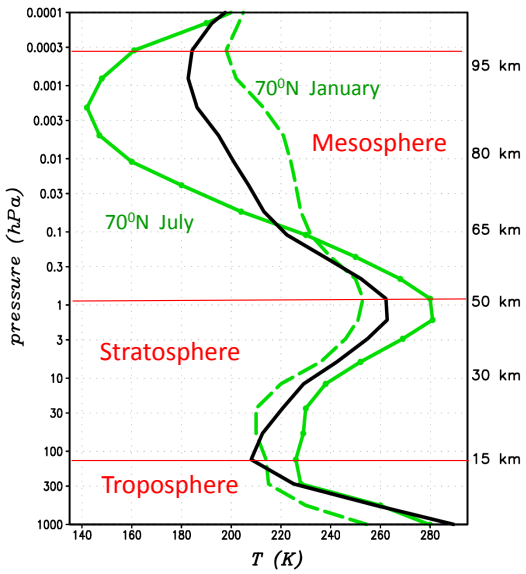

Figure 1.1: Vertical temperature structure of the atmosphere. The black line corresponds to the global annual mean temperature profile. Monthly mean temperature profiles for January and July at $70N$ are displayed by the green lines. The date are taken from the COSPAR International Reference Atmosphere (CIRA) [Fleming et al., 1990].

1.2 Impact of radiative processes on the climate system and the atmosphere

Looking at Earth from space, solar (or short-wave, hereafter: SW) radiation with it's maximum in the visible spectral region constitutes the only noteworthy external source of energy. In the atmosphere, a part of the incoming solar radiation is intercepted due to absorption by gaseous constituents and aerosols or due to reflection on clouds and aerosols. The solar radiation transmitted directly to the ground is partly absorbed there leading to a warming of the surface and a part of it is reflected back to space. In addition, energy can be exchanged with other parts of Earth's climate system at the surface. According to it's temperature, the surface emits thermal (or long-wave, hereafter: LW) radiation with the maximum lying in the infrared spectral region back to the atmosphere. A part of this upward emitted LW radiation is absorbed by the atmosphere and re-emitted into all directions. The downward emission of the atmosphere leads the observed global mean surface temperature to be about 30 K higher than the temperature calculated neglecting this greenhouse effect of the atmosphere. Above the tropopause, the upward emission of LW radiation generally leads to a cooling of the atmosphere. Both the tropospheric and the middle atmospheric LW radiative transfer depend on the amount of radiative active constituents present. In climatological equilibrium the same amount of SW energy absorbed by the earth must go out as LW radiation at the top of the atmosphere (hereafter: TOA). Any imbalance in the global annual-mean radiative energy budged, usually termed as radiative forcing, causes the climate system to move towards another steady state [Hartmann, 1994]. It is evident that radiative processes are among the most important drivers of Earth's climate system as a whole. Therefore a physically consistent parameterization of radiation in numerical models is of paramount importance to study the atmosphere and the climate system.

Based on the observed vertical temperature structure, the atmosphere can be subdivided into different layers as shown in Figure 1.1 [Andrews et al., 1987]. Considering the different layers thus defined, specific physical and dynamical processes are relevant in each height region to determine the observed thermal and dynamical state. The combined effects of radiative processes, latent heat fluxes, and ocean currents usually cause the surface temperature to be

higher than the temperature of the overlying atmosphere. Together with convection which relaxes any (moist) statically unstable temperature gradients to the (moist) adiabatic lapse rate of about -6 K/km, this leads to a hypothetical state of radiative-convective equilibrium T_{rc} [Held et al., 1993; Lorenz, 1964]. The resulting meridional temperature distribution is baroclinically unstable [Holton, 1992] and the so-called available potential energy contained in this temperature structure gets adiabatically transferred to baroclinic waves. Finally the kinetic energy contained in the atmospheric motions is converted to non-available potential energy by dissipation. This so-called Lorenz energy cycle can be visualized by describing the troposphere as a thermodynamic heat engine. The baroclinic waves lead to a meridional energy redistribution such that temperature is reduced in low latitudes and increased in high latitudes compared to T_{rc}. Comparing the latitudinal distribution of the absorbed solar radiation to the emitted thermal radiation then leads to an excess in the tropics and to a deficit in polar regions of the TOA radiative energy budget.

In addition, the troposphere is the region, where most of the atmospheric waves such as gravity waves, planetary waves, or tides are excited due to different processes. Possible excitation mechanisms for gravity waves are convection, jet stream instability, flow over mountains, and geostrophic adjustment [Fritts and Alexander, 2003]. Land-see contrasts or large scale flow around mountains are well-known forcing mechanisms for planetary waves. The diurnal cycle of solar insolation leads to the excitation of tides by absorption of visible radiation by water vapor in the troposphere, absorption of UV radiation by ozone in the stratosphere and by the daily cycle of cumulus convection in the troposphere [Lindzen, 1990]. These atmospheric waves are important to determine the structure of the middle atmosphere and the dynamical coupling between different height regions. Above the temperature minimum characterizing the tropopause, temperature increases with height mostly due to absorption of solar radiation in the stratospheric ozone layer. Except for the polar night region, the thermal state of the stratosphere approximately corresponds to the radiatively determined state, resulting from the balance between the solar energy absorbed by ozone and the thermal radiation emitted in the CO_2 15 μm band and the O_3 9,6 μm band [Shine, 1987]. In the mesosphere, deposition of energy and momentum by atmospheric (mostly gravity) waves leads to strong deviations from the radiatively determined state. Among the most remarkable effects are the dynamically induced cold summer mesopause and the warm winter mesosphere and winter stratopause. The structure of the thermosphere beginning above the mesopause is controlled by a number of additional processes such as dissociation of molecular oxygen, chemical heating, ion drag, and tides [Fomichev et al., 2002].

Alternatively from using the temperature to classify the atmospheric height regions, the atmosphere can be divided into the well mixed homosphere from the surface to about 100 km and the overlying heterosphere, characterized by vertical separation of the atmospheric constituents due to molecular diffusion. Above a height of about 60 km, ionizing processes caused by absorption of solar EUV radiation, interaction of the atmospheric constituents with solar wind particles and cosmic gamma radiation, or precipitating meteors lead to the presence of charged ions and electrons (ionosphere). Therefore, Maxwell‘s equations should be added to the system of governing equations [Schunk and Nagy, 2001] to completely describe the atmosphere at these heights. Very important to a physically consistent description of the LW and SW radiative fluxes and heating rates from the surface up to the lower thermosphere is to account for the decoupling between the radiation field and the kinetic temperature due to the exponentially decreasing air density. In this case, the absorbed radiative energy can not completely be converted into kinetic energy and thermal emission is less efficient. These differences to radiative transfer in the troposphere are known as deviations from LTE usually abbreviated as non-LTE [Thomas and Stamnes, 2002].

1.3 Extension of the mechanistic model concept to the middle atmosphere

Mechanistic models have already been used successfully to gain valuable insights into dynamical processes governing the atmosphere when using temperature relaxation as a simplistic surrogate for radiative transfer calculations.

A well-known setup for a mechanistic GCM was proposed by Held and Suarez [Held and Suarez, 1994] and has been used as a standard benchmark for dynamical cores since then. In this Held-Suarez benchmark test, the orography is omitted, the boundary layer is represented by Rayleigh friction, and the combined effect of all diabatic heating rates is parameterized in terms of temperature relaxation towards an equilibrium temperature T_E. This tropospheric T_E is assumed to represent some radiative-convective equilibrium state. When the middle atmosphere (i.e., the height range from about 10 to 110 km consisting of the stratosphere, the mesosphere, and the mesopause region) is considered, temperature relaxation can be used as a simple surrogate for radiative heating [Andrews et al., 1987; Semeniuk and Shepherd, 2001]. The middle atmospheric T_E then represents the radiatively determined state [Shine, 1987]. Corresponding mechanistic models with temperature relaxation in the middle atmosphere have led to worthwhile insight into the large-scale dynamics [Körnich et al., 2006; Shaw and Shepherd, 2007; Semeniuk and Shepherd, 2002] or have allowed for a high spatial resolution to resolve gravity waves up to the mesopause region [Becker and Fritts, 2006; Becker, 2009].

Explicit, though idealized, representations of radiative transfer, water vapor transport, and condensation/convection have already been developed for tropospheric mechanistic GCMs [Frierson et al., 2006, 2007; Fraedrich et al., 1998]. Such methods were successfully applied, for example, in order to interpret the climate response of comprehensive climate-change simulations with regard to the hydrological cycle [Frierson et al., 2006, 2007]. Explicit radiative transfer schemes of intermediate complexity may also be applied to extend the concept of mechanistic GCMs into the middle atmosphere. This would represent a significant improvement of the mechanistic model concept since the observed deviations from the radiatively determined state are substantial in the winter stratosphere and summer upper mesosphere and the corresponding radiative heating rates are therefore presumably highly nonlinear rather than linear in these deviations meaning that temperature relaxation does not apply.

The idealized approach pursued in the present study allows for radiative transfer calculations that extend continuously from the surface up to the lower thermosphere. The basic idea for the LW-regime derives from the aforementioned approach of Frierson and Held [Frierson et al., 2006, 2007] who used a highly idealized heating due to solar insolation and a broad-band Eddington approximation for the LW regime in the gray limit. Their approach for the LW-regime (see also [Held, 1982]) is equivalent to the 2-stream approximation and results in simple RTEs for the upward and downward energy flux densities that can be solved with negligible computational costs.

To extend this concept into the middle atmosphere, several approximations must be relaxed and corresponding parameterizations must be specified. For example, when using the Eddington approximation for the directional dependence of the LW radiation, the single scattering albedo must be retained as a dynamic variable in order to properly represent non-LTE effects. Furthermore, the broad-band approximation must be relaxed and certain frequency bands that represent the most important absorbers for the structure of the middle atmosphere (CO_2, O_3, and H_2O) must be specified for the LW energy flux densities. As a consequence, one also has to abolish the gray-limit approximation and to parameterize the covariance terms which result from frequency variations of the intensity and absorption coefficient within a band. Nonetheless, as the final formal result of the new concept for the

LW-regime, a set of simplified RTEs is obtained. As a last step, these simplified RTEs are integrated numerically with regard to the vertical discretization of the circulation model in order to obtain the LW radiative energy flux densities and corresponding heating rates. The fact that all of the approximations and parameterizations needed are introduced before performing the vertical integration of the resulting RTEs as a last step is the major difference of the new LW transfer scheme to the more comprehensive Curtis-matrix or Lambda-Iteration methods [Kutepov et al., 1998], which work quite the other way round. Other differences are due to the very simple choice of broad frequency bands, application of the simple Elsasser band model, and the assumption of the Eddington approximation to integrate over the zenith angle. Non-LTE is included by the single scattering albedo which is calculated from the two-level model for each band. To obtain the SW heating rates, the solar flux is split into four broad energetically defined bands for O_3, mesospheric O_2 and H_2O and is subject to absorption according to the simple Beer-Bougert-Lambert law. The continuous computation of the LW and SW radiative energy flux densities allows to take the surface energy budget consistently into account. Differences between land and sea surfaces are given by different heat capacities.

In the next section (2), some theoretical considerations such as a derivation of the governing equations describing both the atmosphere and the radiation field, the physical meaning of the LTE assumption and it‘s range of application, and conventional solution methods of the radiative transfer problem are presented. In section (3) the new continuous radiation scheme is described in detail. Afterwards, some low-resolution results applying the new radiation scheme in a general circulation model are presented (4). In the last section (5), the most important points are summarized and discussed.

Chapter 2

Theoretical background of the physical processes included in a climate model

In the first part of this chapter, both the primitive equations (PE) governing the dynamics of the atmosphere and the radiative transfer equation (RTE) describing the energy change of a light beam passing trough the atmosphere will be derived from general principles of statistical physics. To be acquainted with the broader foundations and to know the assumptions inherent in the specific description of the physical processes included may be useful to extend the physical scope or spatial range of a climate model or to further improve existing parameterizations. For example, when extending the vertical domain farther up into the thermosphere, a number of so far not considered processes become important and some of the basic presumptions that held at lower altitudes break down. As mentioned in the introduction, the atmosphere consists of a large number of particles such that a statistical description using time-dependent mean values of the relevant quantities that characterize the state of the atmosphere is necessary. The time evolution of such a large system cannot be calculated by solving the Hamilton equations for each particle. Instead, a better conception is to describe the atmosphere as an open system in a steady state far from equilibrium. Dissipative processes always tend to restore thermodynamic equilibrium which corresponds to the most likely state of the system with maximum entropy. In this context, the hydrodynamic equations can be derived as evolution equations for the mean quantities describing the state of the atmosphere. Translating these considerations to a monochromatic light beam, the radiative transfer equation can be obtained analogously [Callies and Herbert, 1988a, b; Herbert and Pelkowski, 1990].

In the second part of this chapter, some important definitions concerning the thermodynamic state of the atmosphere and the radiation field will be clarified. For the atmosphere, thermodynamic equilibrium (TE) is never realized. Local thermodynamic equilibrium (LTE) can be assumed up to a height of about 500 km, such that the ideal gas law and the Maxwell velocity distribution can be applied in the whole model domain considered here. Above this height the breakdown of LTE (nonequilibrium) leads to transport equations which are considerably more complicated than the primitive equations. A transport system applicable in this situation could for example be obtained by using the 20-moment-approximation [Schunk and Nagy, 2001]. Though the atmospheric radiation field itself is generally in a strong nonequilibrium state, radiative transfer calculations can be considerably simplified in the majority of cases, where the efficiency of inelastic collisions is sufficient to maintain a Boltzmann dis-

tribution of the number density of the energy levels of the absorbers. This situation is called LTE in the literature of radiative transfer [Thomas and Stamnes, 2002; Liou, 2002]. A state of local thermodynamic equilibrium in analogy to its definition for matter does not exist for the radiation field.

To highlight the specific advantages of the new radiation parameterization and to explain some general issues which complicate the solution of the radiative transfer problem in the atmosphere, a short outline of conventional solution methods based on the analytically integrated RTE will be presented at the end of this chapter.

2.1 Derivation of the hydrodynamic equations and the radiative transfer equations from statistical physics

In the first part of this section, a short discussion of the general problem of describing the state and the evolution of large classical systems (such as the atmosphere) or quantum systems (such as the radiation field) is presented. If not cited otherwise the discussion mainly follows the textbooks of Nolting [Nolting, 2004] and Röpke [Röpke, 1987]. Due to the fact that its not feasible to solve the Hamilton or Schrödinger equation for large systems with many degrees of freedom, only mean values of the characteristic variables that describe the system can practically be calculated. These time-dependent mean variables are obtained by applying time-dependent distribution functions for classical systems or density operators for quantum systems. The time-dependence of the classical distribution function and the quantum mechanical statistical operator are given by the Liouville equation and the von-Neumann equation, respectively [Nolting, 2004]. In case of thermodynamic equilibrium, the right-hand sides of these equations correspond to conserved currents and vanish. For more general nonequilibrium states the dissipative terms appearing on the right-hand-sides lead to an evolution of the system towards its thermal equilibrium characterized by a maximum of its entropy. Noting that the atmosphere can be considered as a dilute gas and that low energy photons can not interact with each other such that correlations can be neglected in both systems, only the time-dependence of the single-particle distribution function or the single-particle statistical operator is needed to obtain the evolution equations. Closing the resulting infinitely large system of evolution equations for the distribution functions of different orders (BBGKY hierarchy) by considering only two-particle collisions to describe the dissipative terms leads to the Boltzmann equation, which can be compared to Reynolds transport theorem [Serin, 1959].

After these general considerations, the volume density, the momentum density and the energy density of the atmosphere are inserted into the transport theorem which leads to the hydrodynamic equations. Application of some further scaling assumptions and transforming to geophysical spherical coordinates leads to the primitive equations (PE) that are solved by the general circulation model applied in this work. Taking the time and zonal mean of the PE and applying corrections due to the Stokes drift, the transformed Eulerian mean equations (TEM) needed to describe the interaction between atmospheric waves and the mean flow are obtained, see Appendix A.

In the last section of this chapter, the radiative transfer equation (RTE) is derived. Assuming that the wavelengths contained in the spectrum of the electromagnetic waves are sufficiently small such that diffraction effects can be neglected [Liou, 2002], the radiation field can be described as a superposition of monochromatic light beams. In analogy to the derivation of the transport equations for the atmosphere, the radiative transfer equation can then be obtained by inserting the monochromatic energy flux density of a monochromatic

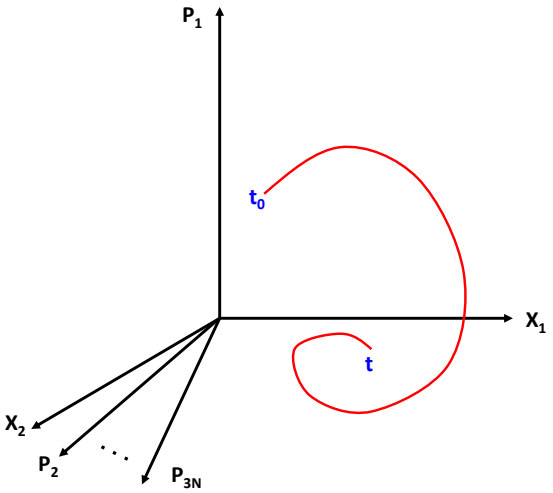

Figure 2.1: Phase space $\Gamma(x_1, p_1, x_2, p_2, \ldots x_{3N}, p_{3N})$ together with a trajectory that describes the evolution of a system from its initial state at t_0 to a later state at t. Note that for the purpose of illustration the axes $x_2, p_2 ... p_{3N}$ are projected into the horizontal plane.

light beam divided by the speed of light into the transport theorem. The processes of absorption, emission and scattering appearing on the right-hand side of this equation correspond to the dissipative source terms which result in energy changes of the monochromatic light beam.

2.1.1 Statistical description of the atmosphere as a large classical and the radiation field as a quantum system

In classical mechanics, the microstate of a closed system of N particles is characterized by the (generalized) positions and (canonical) momenta of each particle. This microscopic state can be visualized as a point in the 6N dimensional phase space Γ spanned by the individual components of the position and momentum vectors of the N particles. Provided that the initial values for all of the position x_i and the momentum components p_i are known at a certain time t_0, the time evolution of the system can be calculated by solving the 6N Hamilton equations [Landau and Lifschitz, 2004]

$$\frac{dx_i}{dt} = \frac{\partial H}{\partial p_i} \tag{2.1}$$

$$\frac{dp_i}{dt} = -\frac{\partial H}{\partial x_i}. \tag{2.2}$$

$H(x_1, p_1 \ldots x_{3N}, p_{3N})$ is the Hamilton function and describes the total (kinetic plus potential) energy of the system. The evolution of the system from its initial state at some initial time t_0 to its state at a later time t can be visualized as a trajectory in the phase space (see Figure 2.1).

In quantum mechanics the concept of describing the microstate of a system as a point and its evolutions as a trajectory in phase space can no longer be applied due to the uncertainty principle. Instead, the state $|\psi\rangle$ of a quantum system is an element (vector) of the Hilbert space and its time evolution is governed by the Schrödinger equation

$$i\hbar\frac{d}{dt}|\psi(t)\rangle = i\hbar\frac{d}{dt}\widehat{U}(t, t_0)|\psi(t_0)\rangle = \widehat{H}|\psi(t)\rangle. \tag{2.3}$$

The unitary evolution operator $\widehat{U}$ promotes the system from its initial state at time t_0 to its state at a later time t

$$|\psi(t)\rangle = \widehat{U}(t, t_0)|\psi(t_0)\rangle. \tag{2.4}$$

and equals the identity operator at time t_0

$$\widehat{U}(t_0, t_0) = 1. \tag{2.5}$$

The Schrödinger equation can be solved in principle if the initial state $|\psi(t_0)\rangle$ and the Hamilton operator of the system are known.

For complex systems with a large number of degrees of freedom the initial state needed to solve the Hamilton or Schrödinger equation is not available. In addition, forced dissipative systems like the atmosphere are usually unstable in the sense that small errors in the initial conditions grow exponentially with time. Trajectories which start from a narrow region in phase space will strongly diverge at a later time [Lorenz, 1963]. In such cases, the solution of the microscopic equations is not practicable. Instead the macroscopic state and evolution is obtained by calculating mean values for the characteristic properties. To calculate these mean values, an ensemble of identical systems governed by the same Hamiltonian is considered. The individual systems of such an ensemble are assumed to start from slightly different initial states which are however compatible with a given set of conserved macroscopic quantities which correspond to the global symmetries of the system [Landau and Lifschitz, 2004]. Usually applied examples are the micro canonical ensemble valid for isolated systems (energy and number of particles exactly conserved), the canonical ensemble for systems exchanging energy with the surroundings (only number of particles exactly conserved), or the grand canonical ensemble for which fluctuations in the energy and the number of particles due to exchanges with the surroundings are allowed.

The time-dependent mean value $\langle A(t)\rangle$ of a classical microscopic dynamic quantity $a(\vec{x}_1, \vec{p}_1; \ldots \vec{x}_N, \vec{p}_N)$ can be obtained by weighting it with the corresponding distribution function $f_N(\vec{x}_1, \vec{p}_1; \ldots \vec{x}_N, \vec{p}_N; t)$ and taking the integral over the whole phase space Γ

$$\langle A(t)\rangle = \int d\Gamma a(\vec{x}_1, \vec{p}_1; \ldots; \vec{x}_N, \vec{p}_N) f_N(\vec{x}_1, \vec{p}_1; \ldots; \vec{x}_N, \vec{p}_N; t). \tag{2.6}$$

In general, the N-particle distribution function f_N depends on the positions and momenta of all particles and is defined as

$$f_N(\vec{x}_1, \vec{p}_1; \ldots \vec{x}_N, \vec{p}_N; t) = N! h^{3N} P(\vec{x}_1, \vec{p}_1; \ldots \vec{x}_N, \vec{p}_N; t). \tag{2.7}$$

It has the meaning of a probability density to find the system in a small volume element at a certain point in the phase space Γ. The factor $N!h^{3N}$, which contains Planck's constant h, takes into account Heisenberg's uncertainty principle [Landau and Lifschitz, 1979] and the fact that individual particles are indistinguishable from each other. Multiplication of the distribution function with the phase space element $d\Gamma$

$$d\Gamma = \frac{d^{3N}x d^{3N}p}{N! h^{3N}} \tag{2.8}$$

gives the probability to find the system in the phase space element $d\Gamma$ around the point $(\vec{x}_1, \vec{p}_1; \ldots \vec{x}_N, \vec{p}_N)$ at time t. The normalization of the distribution function f_N

$$\int d\Gamma f_N = 1, \tag{2.9}$$

ensures that the system can be located somewhere in the phase space at any time t. To calculate mean values of quantities that depend not on all of the N particles, the general reduced s-particle distribution function f_s can be obtained by integration of f_N over the position and momentum coordinates corresponding to the particles numbered from $s+1$ to N

$$f_s(\vec{x}_1, \ldots, \vec{p}_s, t) = \int \frac{d^3\vec{x}_{s+1} \ldots d^3\vec{p}_N}{(N-s)!h^{3(N-s)}} f_N(\vec{x}_1, \ldots, \vec{p}_N, t). \tag{2.10}$$

This so-called reduced distribution function is normalized such that the integration over the whole phase space corresponds to the number of possibilities to choose s particles from the total number available N

$$\int \frac{d^3\vec{x}_1 \ldots d^3\vec{p}_s}{s!h^{3s}} f_s(\vec{x}_1, \ldots, \vec{p}_s, t) = \binom{N}{s}. \tag{2.11}$$

To interprete the ensemble average underlying the definition of the distribution function f_s used to calculate macroscopic mean values (2.6) as observable time mean values the ergodic principle must hold for the system under consideration (see Chapter 1.2 of [Nolting, 2004]). It says that the trajectory of the system approaches each point in the phase space after a finite time interval such that the ensemble average of a dynamic quantity can be set equal to its time average.

To calculate macroscopic mean values for a large quantum system it is not sufficient to calculate just the statistical or ensemble average over a family of systems described by the same Hamilton operator $\widehat{H}$ and starting from different initial conditions. Rather the fact that for a single quantum system the outcome of taking a measurement of an observable A can only be predicted with a specific probability must be considered. This can be done by taking first the quantum average over the possible values a_n of the quantity A into account to obtain the time-dependent mean values describing a large quantum system. The possible measurable values a_n of a observable A are the eigenvalues of the corresponding hermitian operator $\widehat{A}$

$$\widehat{A}|\phi_n\rangle = a_n|\phi_n\rangle. \tag{2.12}$$

The measurement process projects the system from an arbitrary state $|\psi\rangle$ to the eigenstate $|\phi_n\rangle$ which corresponds to the eigenvalue a_n of $\widehat{A}$. The probability w_n of obtaining a certain value a_n when the quantity A is measured is given by the square of the corresponding probability amplitude $\langle\phi_n|\psi\rangle$

$$w_n = \langle\phi_n|\psi\rangle^2. \tag{2.13}$$

The quantum mechanical expectation value $\bar{A}$ for a single system can then be calculated as sum over all of the possible eigenvalues weighted with the corresponding probability

$$\overline{A} = \sum_n a_n w_n = \sum_n a_n |\langle\phi_n|\psi\rangle|^2 = \langle\psi|\widehat{A}|\psi\rangle. \tag{2.14}$$

To finally obtain the macroscopic time-dependent ensemble mean value $\langle A(t)\rangle$ of a large quantum system, the probability P_i that the systems of an appropriately chosen ensemble are found in a certain quantum state $|\psi_i\rangle$ must be taken into account. It can then be written as the statistical average of the quantum average (2.14) by applying the probabilities P_i

$$\langle A(t)\rangle = \sum_i P_i \langle\psi|\widehat{A}|\psi\rangle = \sum_{i,j} \langle\psi_i|\psi_j\rangle P_j \langle\psi_j|\widehat{A}|\psi_i\rangle = Tr\{\hat{\rho}\widehat{A}\}. \tag{2.15}$$

Here, the definition of the statistical operator

$$\widehat{\rho} = \sum_i P_i |\psi_i\rangle\langle\psi_i| \tag{2.16}$$

has been applied and Tr denotes the trace. Representing the statistical operator by its matrix using the basis $|\psi_i\rangle$ it can be seen that the diagonal elements of the resulting density matrix ρ just contain the probabilities P_i, i.e.,

$$\rho_{im} = \langle\psi_i|\widehat{\rho}|\psi_m\rangle = \sum_n \langle\psi_i|\psi_n\rangle P_n \langle\psi_n|\psi_m\rangle = P_i\delta_{im}. \tag{2.17}$$

Therefore the statistical operator is normalized such that the sum over the diagonal elements (trace) equals one

$$Tr\{\widehat{\rho}\} = 1. \tag{2.18}$$

Hence for quantum systems the classical distribution function is replaced by the statistical operator $\hat{\rho}(t)$ which takes both of the two averages into account. Mean values of macroscopic quantities are then obtained by calculating the trace of the statistical operator multiplied by the operator of the quantity $\widehat{A}$

$$\langle A(t)\rangle = Tr\{\widehat{\rho}(t)\widehat{A}\}. \tag{2.19}$$

According to the second law of thermodynamics, the equilibrium distribution function or the statistical operator can be found by maximizing the entropy of the system, including the globally conserved quantities and the normalization condition as constraints. The entropy of a system can be thought of as a measure for the ignorance of its exact state. This ignorance corresponds to the volume in phase space $\Delta\Gamma$ to which the state of a classical system can be constrained. A natural definition of the entropy is therefore any function which increases monotonically with the phase space volume, for example $S = k_B \ln\Delta\Gamma$. Considering a classical system defined by an uniform probability distribution inside a certain phase space volume and zero outside, its distribution function f_N is given by $f_N = 1/\Delta\Gamma$. This connection to the entropy of the system $S = k_B \ln\Delta\Gamma = -k_B \ln(1/\Delta\Gamma) = -k_B \ln f_N$ is generally valid for any distribution function. For systems with a large number of degrees of freedom, only the mean value of this quantity is available which finally (using (2.6)) leads to the following definition of the (coarse grained) entropy as

$$S = -k_B \int d\Gamma\, f_N \ln f_N. \tag{2.20}$$

To describe the entropy of a quantum system the distribution function is replaced by the statistical operator and the integral in (2.20) becomes a summation (trace). The entropy of a quantum system is then given by

$$S = -k_B\, Tr\{\widehat{\rho}\ln\widehat{\rho}\}. \tag{2.21}$$

In the equations above the arguments of the distribution function and the statistical operator are neglected and k_B denotes the Boltzmann constant.

In thermodynamic equilibrium, the distribution function or the statistical operator respectively are independent of time. They depend only on the constant thermodynamic parameters (lagrange multipliers) conjugated to the mean quantities used as constraints to maximize the entropy of the system. Considering a system described by the canonical ensemble for example, the mean value of the energy is used as constraint which leads to a dependence on temperature of the distribution function. Adding the mean value of the number of particles as additional constraint results in the grand canonical distribution function which depends on temperature and on the chemical potential of the system [Nolting, 2004] .

In reality, external forcing processes can drive a system far away from equilibrium. Considering an extreme case of nonequilibrium in the classical case, the state of the system must

be described using the information contained in the full N-particle distribution function f_N. In analogy, the statistical operator of a quantum system depends on an infinite number of parameters in this case. Once the external forcings are switched off, irreversible processes are triggered which tend to bring the system across a sequence of intermediate states to its thermodynamic equilibrium. For a classical system, in the course of this time evolution the entropy increases from a small initial value corresponding to a single point in phase space to its maximum corresponding to a larger volume in phase space. The information (number of parameters) needed to describe the actual state is continuously reduced from the N-particle distribution function to a simple equilibrium distribution. This process is illustrated in Figure (2.2). Starting from a nonequilibrium state containing s-particle clusters described by $f_s(\vec{x}_1, \ldots, \vec{p}_s, t)$, the system evolves by decay of these clusters to the kinetic state. In this state, the particles move uncorrelated such that the system is fully characterized applying the single-particle distribution function $f_1(\vec{x}_1, \vec{p}_1, t)$. If the elastic collision time is shorter than the time needed to cover the distance of the mean free path, the momenta of the particles are redistributed to Maxwell's velocity distribution

$$f^M(\vec{v}) = \left(\frac{m}{2k_B T\pi}\right)^{3/2} \vec{v}^2 \exp\left(-\frac{m\vec{v}^2}{2k_B T}\right) \tag{2.22}$$

with the mass and the velocity of the particles denoted by m and $\vec{v}$ respectively. This state is defined as local thermodynamic equilibrium (LTE) [Schunk and Nagy, 2001]. The momentum dependence of the single-particle distribution function can then be eliminated by applying Maxwell's velocity distribution which depends solely on the local temperature $\mathrm{T}(\vec{x}, t)$. This leads the LTE distribution function $f_1^{LTE}(\vec{x}, t)$ to depend solely on position and time. In fluid dynamics, the assumption of LTE means that each fluid parcel can be described by a single set of variables such as temperature, pressure or velocity [Batchelor, 2001]. The position dependence of the thermodynamic variables in LTE initiates diffusive processes which reduce the existing spatial gradients. Such a system can be described phenomenologically by de Groot's theory of irreversible thermodynamics [de Groot, 1960]. Finally, after the spatial gradients are removed, the system has reached thermodynamic equilibrium (TE). It is now completely characterized by the globally conserved quantities which depend neither on position nor on time.

The canonical ensemble formalism mentioned above to derive equilibrium distribution functions and statistical operators can in principle be extended to more general nonequilibrium states anywhere in the succession described in Figure (2.2) [Röpke, 1987; Vasconcellos et al., 2005; Luzzi et al., 1997b; Madureira et al., 1998; Casas-Vazquez and Jou, 2003; Luzzi et al., 1997a; Eu and Mao, 1992]. The concept underlying this approach is again to maximize the information entropy including additional constraints to derive a relevant statistical operator or distribution function to approximately describe nonequilibrium states of the systems. Although there exist a number of studies applying these ideas to the radiation field [Vasconcellos et al., 2001, 1996; Fort and Lebot, 1998; Fort et al., 1999c, 1998; Fort, 1997; Fort et al., 1999a; Fort, 1999b, a] this approach can at the most be used to describe deviations less than 10% from thermal equilibrium as discussed in some detail in Appendix B. Generally, to describe nonequilibrium states arbitrarily far away from equilibrium, an infinite number of constraints must be included. This fact is mirrored in the appearance of higher order distribution functions f_{N+1} in the evolution equation for f_N which will be illustrated when the evolution equation of the 1-particle distribution function is discussed below. This leads to an infinite hierarchy of equations that must be solved to describe the evolution of the system. To keep the calculations practicable, the hierarchy of variables or equation must be truncated applying appropriate assumptions to close the system [Fort et al., 1999b; Luzzi

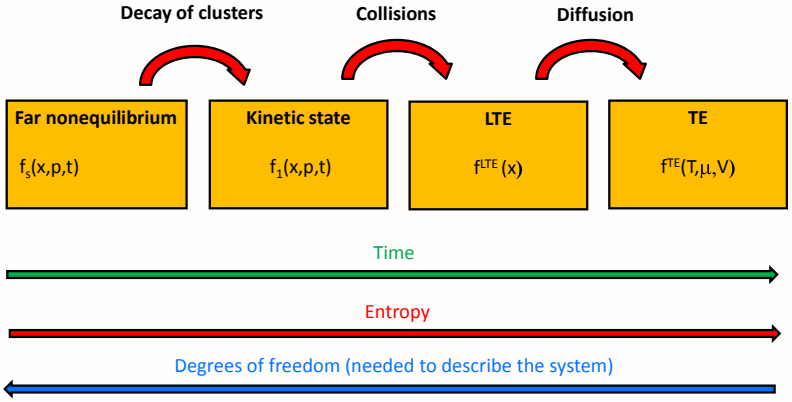

Figure 2.2: The evolution of a thermodynamic system from nonequilibrium to thermodynamic equilibrium. In the course of time, the information needed to describe the state of the system decreases from the full N-particle distribution function f_N to the equilibrium distribution function f^{TE}. In other words, the number of degrees of freedom is reduced from the 6N position and momentum components to the globally conserved quantities. Conversely the entropy increases to its maximum value in thermodynamic equilibrium.

et al., 1998]. This constricts the strength of the deviations from thermal equilibrium that can be described. In principal, the farther away from equilibrium the system considered, the more variables or evolution equations must be retained to describe its state.

The time-dependence of the quantities describing the system, see (2.6) and (2.15), is desribed by the time-dependence of the distribution function or the statistical operator. Therefore the equations of motion for the distribution function or the statistical operator are needed.

The total or convective derivative of the distribution function $f_N(\vec{x}_1, \vec{p}_1; \ldots \vec{x}_N, \vec{p}_N; t)$, which denotes some kind of a "Lagrangian derivative" experienced by an observer moving with the system on its trajectory in phase space, can be written as

$$\frac{df_N}{dt} = \frac{\partial f_N}{\partial t} + \sum_i^N \left(\frac{\partial f_N}{\partial \vec{x}_i} \dot{\vec{x}}_i + \frac{\partial f_N}{\partial \vec{p}_i} \dot{\vec{p}}_i \right). \tag{2.23}$$

The arguments of the distribution function are suppressed to simplify the notation. Defining the phase space velocity $\vec{v}_\Gamma$, the 2N dimensional gradient ∇_Γ and the current density $\vec{J}_\Gamma$ of points in phase space

$$\vec{v}_\Gamma \doteq (\dot{\vec{x}}_1, \ldots, \dot{\vec{p}}_N), \tag{2.24}$$

$$\vec{\nabla}_\Gamma \doteq \left(\frac{\partial}{\partial \vec{x}_1}, \ldots, \frac{\partial}{\partial \vec{p}_N} \right), \tag{2.25}$$

and

$$\vec{J}_\Gamma \doteq f_N \vec{v}_\Gamma \tag{2.26}$$

the total derivative of the distribution function f_N (2.23) can be rewritten in flux form

$$\frac{df_N}{dt} = \frac{\partial f_N}{\partial t} + \sum_i^N \left(\dot{\vec{x}}_i \frac{\partial f_N}{\partial \vec{x}_i} + \dot{\vec{p}}_i \frac{\partial f_N}{\partial \vec{p}_i} \right) + f_N \sum_i^N \left(\frac{\partial}{\partial \vec{x}_i} \dot{\vec{x}}_i + \frac{\partial}{\partial \vec{p}_i} \dot{\vec{p}}_i \right) = \frac{\partial f_N}{\partial t} + \nabla_\Gamma \vec{J}_\Gamma. \quad (2.27)$$

Applying the Hamilton equations (2.1) and (2.2) it can be seen that the last term in the middle expression is zero. It would only contain contributions due to irreversible processes which are not contained in the Hamilton dynamics. Neglecting this irreversible term Liouville's equation (2.28) for the time-evolution of f_N is obtained

$$\frac{df_N}{dt} = \frac{\partial f_N}{\partial t} + \sum_{i=1}^N \left(\frac{\partial f_N}{\partial \vec{x}_i} \dot{\vec{x}}_i + \frac{\partial f_N}{\partial \vec{p}_i} \dot{\vec{p}}_i \right) = \frac{\partial f_N}{\partial t} + \sum_{i=1}^N \left(\frac{\partial H}{\partial p_i} \frac{\partial f_N}{\partial x} - \frac{\partial H}{\partial x_i} \frac{\partial f_N}{\partial p} \right) = 0. \quad (2.28)$$

The right hand side is zero due to the fact that the number of systems contained in the ensemble can not change in the course of time. This is equivalent to the statement that the volume of a region in the phase space occupied by the ensemble systems at an initial time t_0 remains constant in the course of the time evolution following (2.1) and (2.2) (Liouville's theorem, [Nolting, 2004]). The remaining sum in the above equation is a so-called Poisson bracket $\{H, X\}$; it vanishes if X is a conserved quantity [Landau and Lifschitz, 2004]. From the above consideration it is evident that the initial micro state has the same probability as each of the subsequent micro states of the system such that the so-called fine grained entropy does not increase for a system following the reversible Hamilton dynamics (compare 2.20). Conversely considering the more general evolution of a system starting from a state away from thermodynamic equilibrium (Figure 2.2) irreversible processes must be included into the evolution equation. The tendency of the system to maximize its coarse grained entropy is mirrored in the increase of the coarse grained volume in phase space occupied by the ensemble system. In this case, the distribution function f_N is not conserved but satisfies an inhomogeneous Liouville equation containing dissipative source and loss terms on the right hand side. These dissipative processes lead to an increase of the coarse grained entropy with time in agreement with the second law of thermodynamics [Röpke, 1987]

Considering now the description and evolution of a quantum system, the statistical operator takes the role played by the distribution function for classical systems

$$\widehat{\rho} = \sum_i P_i |\psi_i\rangle\langle\psi_i|. \quad (2.29)$$

The evolution of the system is governed by Schrödingers equation (2.3) and, remembering (2.4), the solutions can be described using the definition of the unitary evolution operator $\widehat{U}(t, t_0)$. Inserting (2.4) into (2.3) it can be seen that the evolution operator too satisfies Schrödinger's equation with the formal solution

$$\widehat{U}(t, t_0) = \exp\left(-\frac{i}{\hbar} \widehat{H}(t - t_0) \right). \quad (2.30)$$

The inverse of the evolution operator $\widehat{U}^{-1}$ acts on the covector $\langle\psi|$ of the state vector $|\psi\rangle$

$$\langle\psi(t)| = \langle\psi(t_0)| \, \widehat{U}^{-1}(t, t_0) \quad (2.31)$$

and its time-dependence can be written as

$$\widehat{U}^{-1}(t, t_0) = \exp\left(\frac{i}{\hbar} \widehat{H}(t - t_0) \right). \quad (2.32)$$

Inserting (2.4) and (2.31) into (2.29) the statistical operator is given by

$$\widehat{\rho} = \sum_i \widehat{U}(t,t_0)|\psi(t_0)\rangle p_i \langle\psi(t_0)|\,\widehat{U}^{-1}(t,t_0) = \exp\Big(-\frac{i}{\hbar}\widehat{H}(t-t_0)\Big)p(t_0)\exp\Big(\frac{i}{\hbar}\widehat{H}(t-t_0)\Big). \tag{2.33}$$

Taking the time derivative of this equation finally leads to the von Neumann equation which corresponds to the Liouville equation for classical systems

$$\frac{\partial\widehat{\rho}}{\partial t} - \frac{1}{i\hbar}(\widehat{H}\widehat{\rho} - \widehat{\rho}\widehat{H}) = \frac{\partial\widehat{\rho}}{\partial t} - \frac{1}{i\hbar}[\widehat{H},\widehat{\rho}] = 0. \tag{2.34}$$

In analogy to the meaning of the Poisson bracket for classical systems the commutator $[\widehat{H},\widehat{\rho}]$ is zero if $\widehat{\rho}$ is conserved following the reversible dynamics of the Schrödinger equation.

Both the Liouville and the von Neumann equation can be rewritten as

$$\frac{\partial\rho}{\partial t} + iL\rho = 0. \tag{2.35}$$

when the definition of the Liouville operator L is used. For a classical system, ρ denotes the distribution function and L is identified by a Poisson bracket

$$iL\rho = \{H,\rho\}. \tag{2.36}$$

For a quantum system on the other hand ρ is the statistical operator and L is determined by the commutator

$$iL\rho = -\frac{1}{i\hbar}[H,\rho]. \tag{2.37}$$

In both cases, the right hand side of (2.35) is zero for a reversible evolution of the system. Source and loss terms appear on the right-hand side of (2.35) when dissipative processes are included.

As a first step toward the goal of applying these general considerations concerning the evolution and statistical description of large systems to the atmosphere and the radiation field, we note that the (dry) atmosphere can be described as a dilute gas. Therefore, the kinetic state is appropriate to describe its state and dynamics, compare Figure 2.2. The atmospheric constituents move uncorrelated such that it is sufficient to apply the single-particle distribution function $f_1(\vec{x}_1,\vec{p}_1)$ to calculate mean values of characteristic quantities

$$\langle A(t)\rangle = \int d^3\vec{x}_1 d^3\vec{p}_1 f_1(\vec{x}_1,\vec{p}_1,t)a(\vec{x}_1,\vec{p}_1). \tag{2.38}$$

To determine the time-dependence of these mean values, the evolution equation of the distribution function $f_1(\vec{x}_1,\vec{p}_1)$ is sought. Calculating the total derivative of the single-particle distribution function in analogy to (2.27) leads to

$$\frac{df_1}{dt} = \frac{\partial f_1}{\partial t} + \underbrace{\dot{\vec{x}}_1\frac{\partial f_1}{\partial\vec{x}_1} + \dot{\vec{p}}_1\frac{\partial f_1}{\partial\vec{p}_1}}_{\text{conservative}} + \underbrace{f_1\left(\frac{\partial}{\partial\vec{x}_1}\dot{\vec{x}}_1 + \frac{\partial}{\partial\vec{p}_1}\dot{\vec{p}}_1\right)}_{\text{irreversible}} = \frac{\partial f_1}{\partial t} + \nabla\vec{J}_\Gamma. \tag{2.39}$$

$\dot{\vec{x}}_1$ corresponds to the velocity $\vec{v}_1$ and $\dot{\vec{p}}_1$ to the force $\vec{F}_1$ per unit mass. The force can be subdivided into a conservative part due to external forces $\vec{F}_1^{ext}$ and an irreversible part $\vec{F}_1^{col}$ due to collisions between the constituents of the system. With these definitions (2.39) can be rewritten as

$$\frac{df_1(\vec{x}_1,\vec{p}_1,t)}{dt} = \frac{\partial f_1(\vec{x}_1,\vec{p}_1,t)}{\partial t} + \frac{\partial f_1(\vec{x}_1,\vec{p}_1,t)}{\partial\vec{x}_1}\vec{v}_1 + \frac{\partial f_1(\vec{x}_1,\vec{p}_1,t)}{\partial\vec{p}_1}\vec{F}_1^{ext} + \frac{\partial f_1(\vec{x}_1,\vec{p}_1,t)}{\partial\vec{p}_1}\vec{F}_1^{col}. \tag{2.40}$$

with

$$\frac{\partial f_1(\vec{x}_1,\vec{p}_1,t)}{\partial \vec{p}_1}\vec{F}_1^{col} \doteq f_1\left(\frac{\partial}{\partial \vec{x}_1}\dot{\vec{x}}_1 + \frac{\partial}{\partial \vec{p}_1}\dot{\vec{p}}_1\right). \tag{2.41}$$

This definition of the irreversible force term is motivated by comparing (2.39) and (2.40) and applying the Hamilton equations (2.1) and (2.2). Assuming that the irreversible interactions involve only binary elastic collisions and can be described by a short range interaction potential $U(\vec{x}_1 - \vec{x}_2)$ the collision term (2.41) can be written as

$$\frac{\partial f_1(\vec{x}_1,\vec{p}_1,t)}{\partial \vec{p}_1}\vec{F}_1^{col} = \int \frac{\partial U(\vec{x}_1-\vec{x}_2)}{\partial \vec{x}_1}\frac{d^3\vec{x}_2 d^3\vec{p}_2}{h^3} f_2(\vec{x}_1,\vec{p}_1,\vec{x}_2,\vec{p}_2,t) \doteq \left(\frac{\partial f_1}{\partial t}\right)_{col}. \tag{2.42}$$

To solve (2.40) including this collision term, an evolution equation for the two-particle distribution function $f_2(\vec{x}_1,\vec{p}_1,\vec{x}_2,\vec{p}_2,t)$ is needed which in turn would contain the three-particle distribution function f_3 and so on (BBGKY hierarchy). The need to solve an evolution equation for f_2 can be circumvented by calculating the collision term $\left(\frac{\partial f_1}{\partial t}\right)_{col}$ from the balance between only binary elastic collisions which increase or decrease the probability density $f_1(\vec{x}_1,\vec{p}_1,t)$ respectively. Assuming molecular chaos and neglecting correlations between the collision partners, the infinite hierarchy of equations can then be truncated by replacing the two-particle distribution function by a product of single particle distribution functions as explained for example in [Röpke, 1987]

$$\left(\frac{\partial f_1}{\partial t}\right)_{col} = \int d^3\vec{v}_2 \int d\Omega \frac{d\sigma}{d\Omega}|\vec{v}_1 - \vec{v}_2|\Big(\underbrace{f_1(\vec{x}_1,\vec{v}_1',t)f_1(\vec{x}_1,\vec{v}_2',t)}_{\text{Gain}} - \underbrace{f_1(\vec{x}_1,\vec{v}_1,t)f_1(\vec{x}_1,\vec{v}_2,t)}_{\text{Loss}}\Big). \tag{2.43}$$

The primes denote the velocities after the collision and $\frac{d\sigma}{d\Omega}$ is the differential scattering cross section. Applying this collision term in the evolution equation for the single-particle distribution function (2.40) leads to the *Boltzmann equation*

$$\frac{df_1}{dt} = \frac{\partial f_1}{\partial t} + \frac{\partial f_1}{\partial \vec{x}_1}\vec{v}_1 + \frac{\partial f_1}{\partial \vec{p}_1}\vec{F}_1^{ext} = -\left(\frac{\partial f_1}{\partial t}\right)_{col}. \tag{2.44}$$

Remembering that the collision term from its definition parameterizes the effects of irreversible forces, and that $\vec{F}_1^{ext}$ contains only the conservative forces, the Boltzmann equation can be rewritten in "flux form" with nonzero right-hand side due to irreversible entropy producing processes

$$\frac{df_1}{dt} = \frac{\partial f_1}{\partial t} + \nabla\vec{J} = -\left(\frac{\partial f_1}{\partial t}\right)^{col}. \tag{2.45}$$

In the atmosphere, LTE holds up to a height of about 500 km (exobase) [Schunk and Nagy, 2001]. Therefore, the Maxwell distribution can be assumed for the velocity or momentum distribution respectively such that the momentum dependence of the single-particle distribution function can be replaced by the dependence on the local temperature $\mathrm{T}(\vec{x}_1)$ of the Maxwell distribution. Hence the momentum dependence of the single-particle distribution function $f_1(\vec{x}_1,\vec{p}_1,t)$ can be eliminated. Applying the Boltzmann equation (2.45) for the time-dependence of the distribution function the macroscopic time-dependent mean value of

a microscopic dynamic quantity a($\vec{x}$) is given by

$$\begin{aligned}\frac{\langle A(t)\rangle}{dt} &= \int \frac{df_1(\vec{x}_1,t)}{dt} a(\vec{x}_1) d\vec{x}^3 \\ &= \int \left(\frac{\partial f_1(\vec{x}_1,t)}{\partial t} a(\vec{x}_1) + \nabla(\vec{v}_1 f_1(\vec{x}_1,t) a(\vec{x})) \right) d\vec{x}^3 \\ &= \int -\left(\frac{\partial f_1}{\partial t}\right)^{col} a(\vec{x}_1)\, d\vec{x}^3.\end{aligned} \tag{2.46}$$

Defining the volume density of a flow variable $X(\vec{r},t) = f_1(\vec{x}_1,t)a(\vec{x}_1)$ and rewriting the spatial integration as volume integral over the volume in phase space occupied by the ensemble systems the so-called transport equation (2.46) can be rewritten as

$$\frac{d}{dt}\int\limits_V X(\vec{r},t)dV = \int\limits_V \left(\frac{\partial X(\vec{r},t)}{\partial t} + \nabla(\vec{v}(\vec{r},t)X(\vec{r},t)) \right) dV = \text{sources and sinks.} \tag{2.47}$$

Identification of this volume with the volume of a fluid parcel moving along with the fluid (2.47) corresponds to Reynolds' transport theorem [Serrin, 1959]. Another motivation for the correspondence between the transport equation and the transport theorem is that the Liouville equation (2.28) can be perceived as a continuity equation describing the incompressible flow of system points through phase space [Nolting, 2004].

2.1.2 Derivation of the hydrodynamic equations

In the following paragraphs the transport theorem (2.47) will be used to derive the hydrodynamic equations by identifying X with the density of mass, linear momentum and total energy of a fluid parcel moving with the flow. Together with the thermodynamic equation of state for an ideal gas and after a transformation to geophysical spherical coordinates, this leads to the primitive equations (PE). This set of equations is numerically solved by the mechanistic model used in this study. In Appendix A the interaction between atmospheric waves and the mean flow will be discussed using the transformed Eulerian mean equations.

The continuity equation can be obtained by itentifying X in the transport theorem with the mass density. Noting that the mass is exactly conserved, and that the transport theorem is valid for every control volume V, the volume integration in (2.47) can be "omitted" by taking the limit of $V \to 0$

$$\frac{d\rho}{dt} = \frac{\partial \rho}{\partial t} + \nabla(\rho\vec{v}) = \frac{\partial \rho}{\partial t} + (\nabla\rho)\vec{v} + \rho\nabla\vec{v} = \dot{\rho} + \rho\nabla\vec{v} = 0. \tag{2.48}$$

A flow is called incompressible if $\nabla\vec{v} = 0$ such that the total time derivative of the density $\dot{\rho} = -\rho\nabla\vec{v}$ vanishes. As can be seen by rewriting the total derivative of the density as a thermodynamic state variable which depends on pressure p and the entropy density s

$$\dot{\rho} = \left(\frac{\partial\rho}{\partial p}\right)_s \dot{p} + \left(\frac{\partial\rho}{\partial s}\right)_p \dot{s} \tag{2.49}$$

ideal fluids with $\left(\frac{\partial\rho}{\partial p}\right)_s = 0$ are not strictly incompressible. In addition a strictly incompressible flow must be isentropic such that the net entropy change of a fluid parcel vanishes ($\dot{s} \doteq \frac{\partial s}{\partial t} + \vec{v}\nabla s$).

The momentum equation can be derived by considering the conservation law for linear momentum and setting X to the volume density of linear momentum $X \doteq \rho\vec{v}$ in the transport

theorem (2.47). In fluid dynamics, the forces altering the momentum density of the control volume are usually subdivided into body forces acting throughout the volume and surface forces acting on the surfaces of the control volume. The only body force relevant in this case is gravity, which can be written as the gradient of the gravitational potential $\Phi = gz$ assuming that the height z is sufficiently small such that position dependence of the sufficiently weak gravitational field can be neglected. The surface forces $(\overleftrightarrow{S} - pI)d\vec{f}$ acting on the surface orthogonal to $d\vec{f}$ can be further subdivided into the normal pressure force (given by the unity tensor multiplied by pressure) and the shear forces (defined by the stress tensor $\overleftrightarrow{S}$) that act on a surface element $d\vec{f}$ of the control volume. Inserting these definitions into the transport theorem leads to

$$\frac{d}{dt}\int\limits_V \rho\vec{v}dV = -\int\limits_V \rho\nabla\Phi dV + \int\limits_{\partial V} \rho(\overleftrightarrow{S} - pI)d\vec{f} \tag{2.50}$$

To convert this integral equation into the differential momentum equation Gauss' theorem can be used to transform the surface integral into a volume integral. After taking into account the continuity equation (2.48), noting that the stress tensor $\overleftrightarrow{S}$ must be symmetric $\overleftrightarrow{S}=\overleftrightarrow{S^T}$ such that the conservation of angular momentum is guaranteed, and letting again $V \to 0$, the momentum equation can be written as

$$\frac{\partial\vec{v}}{\partial t} + (\vec{v}\cdot\nabla)\vec{v} = -\frac{\nabla p}{\rho} - \nabla\Phi + \frac{1}{\rho}\nabla\overleftrightarrow{S}\,. \tag{2.51}$$

The first two terms on the right hand side describe conservative processes since they do not change the entropy. In contrast the last expression which contains the stress tensor is an irreversible process which tends to reduce the existing velocity gradients due to internal friction and is accompanied by entropy production. The continuity equation (2.48) together with the momentum equation (2.51) are called *Euler equations* if the stress tensor $\overleftrightarrow{S}$ vanishes. They are known as *Navier-Stokes equations* if the stress tensor describes the molecular friction [Landau and Lifschitz, 1986]

$$\overleftrightarrow{S} = \rho\,\nu\{\nabla\circ\vec{v} + (\nabla\circ\vec{v})^T\} + \rho\,\eta I(\nabla\cdot\vec{v}). \tag{2.52}$$

The coefficients η and ν here denote the dynamic and the kinematic viscosity respectively and $\circ$ is the outer (or tensor) product of two tensors.

Setting X to the total energy density composed of the kinetic and the internal energy of the control volume assuming $X \doteq \rho(e + \frac{\vec{v}^2}{2})$ in the transport theorem (2.47), the thermodynamic (or energy) equation can be derived. The total energy of the control volume can be changed due to interactions between the radiation field and the absorbers (Q_{rad}), phase transitions (Q_{lat}), motion along the gradient of the geopotential $\nabla\Phi$, heat fluxes $\vec{J}$ crossing the boundary ∂V of the control volume, by work done by frictional forces or due to adiabatic conversion

$$\frac{d}{dt}\int\limits_V \rho(e + \frac{\vec{v}^2}{2})dV = \int\limits_V \rho(Q_{rad} + Q_{lat})dV \tag{2.53}$$

$$-\int\limits_V \rho\vec{v}\cdot\nabla\Phi\,dV - \int\limits_{\partial V}\vec{J}d\vec{f} + \int\limits_{\partial V}\vec{v}(\overleftrightarrow{S} - pI)d\vec{f}. \tag{2.54}$$

Applying again Gauss' theorem, the symmetry of the stress tensor, the momentum (2.51) and the continuity equation (2.48), and using again $V \to 0$, the differential thermodynamic

equation is given by

$$\frac{d}{dt}e = \frac{p}{\rho^2}\frac{d}{dt}\rho + Q_{rad} + Q_{lat} - \frac{1}{\rho}\nabla\vec{J} + \frac{1}{\rho}(\overleftrightarrow{S}\ \nabla)\cdot\vec{v}. \tag{2.55}$$

The last term is the frictional heating or dissipation ϵ which must be positive definite according to the second law of thermodynamics

$$\epsilon = \frac{1}{\rho}(\overleftrightarrow{S}\ \nabla)\cdot\vec{v}. \tag{2.56}$$

Neglecting the frictional heating in atmospheric general circulation models leads to an unrealistic global annual mean warming corresponding to a climate forcing of about 2 Wm^{-2} [Becker, 2003a]. Applying the definition of the enthalpy $H = U + pV$ the thermodynamic equation can be rewritten as transport equation for the enthalpy density $h = e + \frac{p}{\rho}$ of the control volume

$$\begin{aligned} \frac{d}{dt}h &= \frac{d}{dt}\left(\frac{p}{\rho}\right) + Q_{rad} + Q_{lat} - \frac{1}{\rho}\nabla\vec{J} + \epsilon \\ &= \frac{d}{dt}\left(\frac{p}{\rho}\right) + T\frac{d}{dt}s. \end{aligned} \tag{2.57}$$

From this equation it can be seen that radiative heating, phase transitions and heat fluxes are irreversible processes, that would together with the dissipation appear in the collision term of the Boltzmann equation whereas the first term (adiabatic conversion) on the right-hand side is conservative.

To model the dynamics of the atmosphere in a general circulation model, the continuity equation (2.48), the momentum equation (2.51) and the thermodynamic equation (2.55) are transformed to geophysical spherical coordinates (z, λ, ϕ) where z is the height above the surface of the earth, λ is the longitude and ϕ is the latitude. The distance from the origin of the coordinate system is defined as $r = a + z$ with the earth radius a = 6378 km. The geometry of this coordinate system is visualized in Figure 2.3. To calculate the derivatives appearing in the hydrodynamic equations in the new curvilinear coordinate system (z, λ, ϕ), the spatial dependence of the local cartesian coordinate system spanned by the unit base vectors in the azimuthal, latitudinal and vertical direction must be considered. Details are given in [Holton, 1992].

Transforming to geophysical coordinates (Figure 2.3) and applying the appropriate scaling assumptions and the traditional approximation for large scale flow, the hydrodynamic equations can be further simplified [Phillips, 1966, 1973; Pichler, 1986]. Including the coriolis force (which appears due to the fact that rotating earth is a non-inertial reference frame) in the momentum equation results in the system of the primitive equations (PE) given in vertical height coordinates here. These equations are solved by the mechanistic model using hybrid-coordinates [Simmons and Burridge, 1981]. For the purpose of diagnostics, the PE are given in p-coordinates below

$$\begin{aligned} \frac{\partial}{\partial t}\vec{v} &= \vec{v}\times(f+\xi)\vec{e}_z - \omega\frac{\partial}{\partial p}\vec{v} - \nabla\left(\Phi + \frac{\vec{v}^2}{2}\right) + \vec{R} \\ \frac{\partial}{\partial p}\Phi &= -\frac{1}{\rho} = -\frac{RT}{p} \\ 0 &= \nabla\cdot\vec{v} + \frac{\partial}{\partial p}\omega \\ c_p\frac{d}{dt}T &= \frac{\omega}{\rho} + Q_{rad} + Q_{lat} + \eta + \epsilon. \end{aligned} \tag{2.58}$$

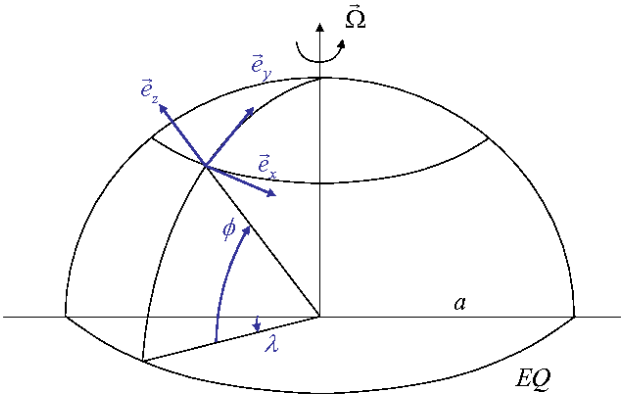

Figure 2.3: The geophysical spherical coordinate system. z is the height above the surface of the earth, ϕ is the latitude and λ is the longitude. The unit vectors, spanning a local cartesian coordinate system at a point of the surface are denoted as $\vec{e}_x$ (longitudinal direction), $\vec{e}_y$ (latitudinal direction) and $\vec{e}_z$ (vertical) direction.

The anelastic approximation is assumed applying the height dependent reference density profile $\rho_r = \rho_r(z)$ For the vertical velocity kinematic boundary conditions are specified using the topographic height as a lower boundary. The dynamical boundary conditions for the stress tensor $\overleftrightarrow{S}$ needed for the dissipation ϵ and the latent and sensible heat fluxes contained in η, compare (2.55) are specified further in the boundary layer model [Becker, 2003b]. To solve these equations by the mechanistic model vertical hybrid coordinates are applied [Simmons and Burridge, 1981].

Deviations from the radiatively determined state of the climatological temperature and wind distributions observed up to the lower thermosphere are essentially determined by interactions between atmospheric waves and the mean flow. The real wave-mean-flow interaction is described by the transformed Eulerian mean equations (TEM) which are further discussed in the appendix.

2.1.3 The radiative transfer equation as an evolution equation for the energy density of a monochromatic light beam

In atmospheric GCMs, the hydrodynamic equations described in the previous sections are solved numerically to calculate the time evolution of the state of the atmosphere. As mentioned in the introduction, absorption of solar radiation and emission of thermal radiation provide the most important contribution to the differential heating in the troposphere and are important for the structure of the whole atmosphere. Changes of the downward solar short-wave (S) and the long-wave thermal (upward U and downward D) radiative energy fluxes due to the interaction of the radiation field with the atmosphere lead to radiative heating rates (Q_{rad}) and accordingly to radiative temperature changes $\left(\frac{\partial T}{\partial t}\right)_{rad}$. These effects must be considered in the energy equation (2.53) and in the surface energy balance, see Chapter 4.1. On the other hand, the thermodynamic state of the atmosphere given for example by the temperature and pressure field as well as the air density in turn impact the propagation of radiative energy.

The radiative temperature change in the atmosphere is determined by the divergence of the radiative energy fluxes. Here, the plane-parallel approximation and pressure coordinates are

applied as usual (see Section 2.3 for further explanations),

$$\left(\frac{\partial T}{\partial t}\right)_{rad} = \frac{g}{c_p}\frac{\partial}{\partial p}(U - D - S). \tag{2.59}$$

The surface is heated by the absorbed part $(1-\alpha)S$ of the solar flux and the downward long-wave flux D whereas cooling takes place due to thermal emission in the long-wave regime. Here we distinguish between the flux that is subject to absorption and emission in the atmosphere, U, and the flux that goes directly to space, $(\sigma T_s^4 - U)$,

$$\left(\frac{\partial T_s}{\partial t}\right)_{rad} = \frac{1}{C_{surf}}\left[(1-\alpha)S + D - U - (\sigma T_s^4 - U)\right]_{surf}. \tag{2.60}$$

The radiative temperature tendencies (2.59) and (2.60) result from the changes that the radiative energy fluxes experience due to interactions with the atmosphere and the surface. Since the thermal emission spectra of the sun (maximum in the visible frequency range) and the earth (maximum in the infrared region) are clearly separated, the radiative heating rates due to short-wave and long-wave radiation can be calculated separately [Liou, 2002].

Propagation of radiative energy through the atmosphere can be calculated by describing the radiation field as a superposition of monochromatic light beams characterized by a certain frequency (i.e. energy) and a specific direction of propagation. To calculate the radiative energy fluxes appearing in the radiative temperature tendencies, the non conservative propagation of radiative energy through the atmosphere must be considered. This can be done by solving the evolution equation for the energy density of a monochromatic light beam and integrating over all directions of propagation for the upper and lower half space to get the upward and downward spectral radiative energy flux densities.

The energy equation for a monochromatic light beam can be derived by setting the velocity $\vec{v}$ to $\vec{n}c$ (c is the speed of light) and X to $\frac{I_\nu(\vec{r},\vec{n},t)}{c}$ in the transport equation (2.47). This leads to the so-called radiative transfer equation (RTE) [Callies and Herbert, 1988b; Chandrasekhar, 1960],

$$\frac{1}{c}\frac{\partial I_\nu(\vec{r},\vec{n},t)}{\partial t} + \vec{n}\cdot\frac{\partial I_\nu(\vec{r},\vec{n},t)}{\partial \vec{r}} = \rho(\vec{r},t)\kappa_\nu(\vec{r},t)\left\{-I_\nu(\vec{r},\vec{n},t) + S_\nu(\vec{r},\vec{n},t)\right\}. \tag{2.61}$$

$I_\nu(\vec{r},\vec{n},t)\cos\Theta\, d\nu\, df\, d\Omega\, dt$ at the position $\vec{r}$ is defined as the radiative energy in the frequency interval $\nu, \nu + d\nu$ transported through the surface element df into the solid angle element $d\Omega$ enclosing the direction $\vec{n}$ during a time increment dt, see the left part of Figure 2.4. The source terms on the right hand side of (2.61) correspond to the collision term in the Boltzmann equation [Eu and Mao, 1992] and describe the reduction of the energy of a monochromatic light beam by absorption (absorption coefficient $\kappa_\nu(\vec{r},t)$) and the increase by the competing processes of scattering (single scattering albedo $\omega_\nu(\vec{r})$) and thermal emission (emissivity $1 - \omega_\nu(\vec{r})$). The unit vector $\vec{n} = \vec{n}(\vartheta,\varphi)$ depends on the zenith angle ϑ and the azimuthal angle φ, compare the right panel in Figure 2.4. Scattering and thermal emission are usually subsumed in the source function $S_\nu(\vec{r},\vec{n},t)$, which must not be confused with the solar energy flux density in (2.59) and (2.60). The relative importance of both processes is given by the single scattering albedo ω_ν, and the directional dependence of scattering is contained in the phase function $P_\nu(\vec{n},\vec{n}')$,i.e.,

$$S_\nu(\vec{r},\vec{n},t) = \omega_\nu \int_0^{4\pi} I_\nu(\vec{r},\vec{n}',t)\frac{P_\nu(\vec{n},\vec{n}')}{4\pi}d\Omega' + (1-\omega_\nu)B_\nu(T). \tag{2.62}$$

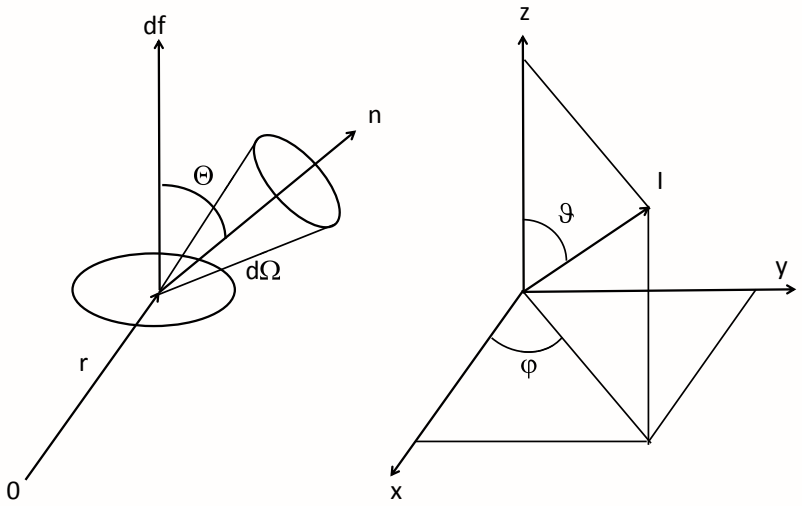

Figure 2.4: Left part: Geometry used to define the intensity of the monochromatic radiation field at a position r as the radiative energy in a frequency interval transported through the surface element df into the solid angle element $d\Omega$ enclosing the direction n during a time increment. Right part: Coordinate system for the plane-parallel approximation. The position dependence of the intensity reduces to some vertical coordinate z and the direction is given in polar coordinates (ϑ, φ).

$d\Omega' = d\varphi' \sin\vartheta' d\vartheta'$ is the solid angle element corresponding to the direction $\vec{n}'$. The phase function describes the probability that a light beam of frequency ν is scattered from another direction $\vec{n}'$ into the direction $\vec{n}$ of the beam considered. The phase function is normalized such that

$$\int_0^{4\pi} \frac{P_\nu(\vec{n}, \vec{n}')}{4\pi} d\Omega' = 1. \tag{2.63}$$

$B_\nu(T)$ is Planck 's law for the thermal emission of a black body,

$$B_\nu(T) = u^*_\nu(T)\frac{c}{4\pi} = \frac{2\pi h\nu^3}{c^3}\frac{1}{\exp\left(\frac{h\nu}{k_B T}\right) - 1} \tag{2.64}$$

Here, $u^*_\nu(T)$ is the spectral energy density of the radiation field in thermodynamic equilibrium,

$$u^*_\nu(T) = \frac{8\pi h\nu^3}{c^3}\frac{1}{\exp\left(\frac{h\nu}{k_B T}\right) - 1}. \tag{2.65}$$

The next section shows that this equilibrium spectral density applied in Planck's law (2.64) can be derived by considering the radiation field as an ultrarelativistic ideal Bose gas.

Due to the large value of the speed of light c, the first term on the left hand side of the RTE (2.61) can be neglected and the stationary form is used to do radiative transfer calculations in atmospheric applications

$$\vec{n} \cdot \frac{\partial I_\nu(\vec{r}, \vec{n})}{\partial \vec{r}} = \rho(\vec{r})\kappa_\nu(\vec{r}) \left\{-I_\nu(\vec{r}, \vec{n}) + S_\nu(\vec{r}, \vec{n})\right\}. \tag{2.66}$$

Considering only thermal radiation and clear air calculations in the LW regime, the source function (2.62) consists of thermal emission and isotropic scattering ($P_\nu(\vec{n},\vec{n}') = 1$) and can be simplified as

$$S_\nu(\vec{r}) = (\,1 - \omega_\nu(\vec{r})\,)\, B_\nu(T(\vec{r})) + \omega_\nu(\vec{r})\,(4\pi)^{-1} \int I_\nu(\vec{r},\vec{n})\, d\Omega\,. \tag{2.67}$$

Assuming furthermore that the electric field vectors are not correlated when the radiation field is described by electromagnetic waves, polarization effects can be neglected. Therefore the intensity is the only component of the more general Stokes vector (I, Q, U, V) that must be retained to describe a monochromatic light beam (Liou [2002]).

2.2 Thermodynamic state of the radiation field and simplifications applied to determine the radiative heating rates

The primitive equations together with the radiative transfer equation describe the time development of the atmosphere and the radiation field as well as their mutual interaction. From a thermodynamical point of view, the whole system is composed of the atmosphere with its gaseous constituents and the radiation field as distinct thermodynamic systems [Callies and Herbert, 1988a, b; Herbert and Pelkowski, 1990; Kutepov et al., 1998]. In order to obtain the correct heating and cooling rates which result from the interaction between the radiation field and the absorbers it is important, particularly in the middle atmosphere, to apply the proper assumptions concerning the thermodynamic state of both subsystems. In the last section definitions such as TE, LTE and nonequilibrium have been defined, see Figure (2.2). In this section the meaning of these definitions for the radiation field and their use in radiative transfer calculations will be clarified. Considering the atmosphere LTE can usually be assumed up to about 500 km [Schunk and Nagy, 2001]. Hence, the ideal gas law and Maxwell's velocity distribution can safely be applied when the model domain ranges from the surface to about 120 km. Describing the radiation field as an ultra-relativistic Bose gas, its thermodynamic equilibrium spectral energy density can be derived by using the corresponding statistical operator which is obtained by maximizing the entropy and applying the total energy as constraint. To allow for small deviations from thermodynamic equilibrium, additional constraints can be included to derive corrections to Planck's law for thermal emission. Alternatively, describing the radiation field as a superposition of monochromatic light beams, nonequilibrium states can be described by considering each light beam as a distinct thermodynamic subsystem characterized by its specific radiation temperature [Callies and Herbert, 1988a, b; Herbert and Pelkowski, 1990; Kutepov et al., 1998]. Concerning radiative transfer calculations in the atmosphere, the radiation field strongly deviates from TE, such that Planck's law is in general not valid. Nevertheless, assuming a sufficient frequency of inelastic collisions which maintains the Boltzmann distribution of the ratio of number densities of the energy levels of a radiative transition considered, radiative transfer calculations can widely be simplified. In this case, which is denoted as LTE in the radiative transfer literature [Thomas and Stamnes, 2002], the source function in (2.61) contains only the emission term given by Planck's law (2.64). Conversely, in situations where the Boltzmann distribution can not be maintained due to an insufficient number of inelastic collisions, an additional scattering term must be included into the source function whereas thermal emission is reduced (non-LTE). A motivation for the parameterization of non-LTE effects using the single scattering albedo applied in this work will be given by comparing the macroscopic RTE to the two-level statistical equilibrium equation for the number densities of the energy levels of a transition.

2.2.1 The energy density of the equilibrium radiation field

Considering the radiation field as an ideal ultra-relativistic Bose gas that consists of N photons (with no mass), the microstate of the radiation field can be described by the occupation numbers n_{p_i} of one particle momentum states $|p_i\rangle$

$$\psi = |n_{p_1} n_{p_2} \dots n_{p_N}\rangle = |n_{p_1}\rangle |n_{p_2}\rangle \dots |n_{p_N}\rangle. \tag{2.68}$$

The total energy E of the radiation field is the eigenvalue obtained from solving the eigenvalue equation $\widehat{H}\psi = E\psi$ of the Hamilton operator $\widehat{H} = \sum_i \frac{\widehat{p_i}^2}{2m}$. In second quantization it can be calculated as the sum of all photon energies ($\varepsilon_{p_i} = h\nu_i = cp_i$) corresponding to the momentum states $|p_i\rangle$ weighed by the mean occupation number $\langle n_{p_i}\rangle$

$$E = \sum_i \varepsilon_{p_i} \langle n_{p_i}\rangle. \tag{2.69}$$

As explained before the mean occupation number of a momentum state $|n_{p_i}\rangle$ can be obtained from (2.15) leading to

$$\langle n_p\rangle = Tr\{\widehat{\rho}\,\hat{n}_p\}. \tag{2.70}$$

Here $\hat{n}_p = \hat{a}_p^\dagger \hat{a}_p$ is the occupation number operator defined as the product of the creation operator $\hat{a}_p^\dagger$ times the annihilation operator $\hat{a}_p$ [Röpke, 1983]. Noting that the radiation field can lose and gain photons via absorption and emission such that the number of photons is not fixed, it is appropriate to describe it by a grand canonical ensemble. Accordingly the mean energy $\langle E\rangle$ and the mean number density $\langle N\rangle$ are applied as constraints in the maximization of the entropy to obtain the statistical operator $\widehat{\rho}$ of the photon gas in thermodynamic equilibrium (2.21). This leads to

$$\widehat{\rho} = \frac{1}{Z_{gk}} \exp\{\beta(\widehat{H} - \mu\widehat{N})\} \tag{2.71}$$

with the number operator $\widehat{N} = \sum_i \hat{n}_{p_i}$ and $\beta = \frac{1}{k_B T}$. Invoking the indistinguishability of identical particles in a quantum system and applying a symmetric wavefunction (2.68) to the radiation field described as boson gas, the grand canonical partition function Z_{gk} is given by

$$Z_{gk} = \prod_i \frac{1}{1 - \exp\{\beta(\varepsilon_p - \mu)\}}. \tag{2.72}$$

Specifically, for the non-selfinteracting photons the chemical potential μ which corresponds to the energy needed to add additional photons to the radiation field vanishes such that the distribution of the mean occupation numbers can be written as

$$\langle n_p\rangle = \frac{1}{\exp(\beta\varepsilon_p) - 1}. \tag{2.73}$$

Inserting this into (2.69) and converting the summation over all of the momentum states into an integral

$$\sum_p = \frac{2 \cdot V}{(2\pi\hbar)^3} \int d^3p \tag{2.74}$$

the total energy of the radiation field can be written as

$$E = \frac{2 \cdot V}{(2\pi\hbar)^3} \int d^3p \frac{\varepsilon_p}{\exp\{\beta\varepsilon_p\} - 1}. \tag{2.75}$$

Here the denominator of the ratio in front of the integral takes again the quantization of the momentum spaces due to Heisenberg's uncertainty principle into account (compare (2.7),V is the volume containing the photon gas and the factor 2 allows for the two polarizations of the photon [Zee, 2003]. Solving this integral, dividing by the volume V, and transforming from momentum to frequency space, the thermodynamic equilibrium monochromatic energy density $u_\nu^*(T)$ can be defined as

$$\frac{E}{V} = \int u_\nu^*(T)\, d\nu \tag{2.76}$$

with

$$u_\nu^*(T) = \frac{8\pi h\nu^3}{c^3} \frac{1}{\exp\left(\frac{h\nu}{k_B T}\right) - 1}. \tag{2.77}$$

Inserting this equilibrium spectral energy density into (2.64) leads to Planck's law for thermal emission .

2.2.2 The nonequilibrium radiation field

The method applied in the previous section to derive the equilibrium spectral energy density of the radiation field can in principle be extended to nonequilibrium states [Vasconcellos et al., 2005; Röpke, 1987]. However, to calculate the mean occupation numbers from (2.70), the grand canonical equilibrium statistical operator (2.71) must be replace by a more general time-dependent statistical operator. In general, this nonequilibrium statistical operator $\widehat{\rho}_\epsilon(t)$ depends on all of the previous states of the system. The past states at times t_1 with $t_0 \leq t_1 \leq t$ are described by the so-called relevant statistical operator $\widehat{\rho}_0(t_1)$, which depends, conversely to the equilibrium case, on additional variables apart from the conserved quantities needed to describe the system in thermodynamic equilibrium. The importance of the contribution of each past state is assumed to decrease exponentially with time (fading memory [Vasconcellos et al., 2005])

$$\widehat{\rho}_\epsilon(t) = \frac{1}{t - t_0} \int_{t_0}^{t} e^{i(t_1 - t)L} \widehat{\rho}_0(t_1) dt_1. \tag{2.78}$$

Here, L is again the Liouville operator (compare its definition in (2.35)) and $\widehat{\rho}_\epsilon(t)$ satisfies an inhomogeneous von Neumann equation with a dissipative term appearing on the right hand side

$$\frac{\partial \widehat{\rho}_\epsilon(t)}{\partial t} + iL\widehat{\rho}_\epsilon(t) = -\epsilon(\widehat{\rho}_\epsilon(t) - \widehat{\rho}_0(t)). \tag{2.79}$$

The relevant statistical operator $\rho_0(t)$ can be considered as a generalization of the grand canonical statistical operator (2.71). Apart from the mean energy and the mean number density it depends on additional quantities A_n which are needed to describe a state of the system which deviates from its thermodynamic equilibrium (compare Figure 2.2)

$$\widehat{\rho}_0(t) = e^{-\Phi(t) - \sum\limits_n F_n(t) A_n}. \tag{2.80}$$

The $\mathrm{F}_n(\mathrm{t})$ are the thermodynamic parameters (Lagrange multipliers) which correspond to the variables A_n. $\Phi(t)$ is the Messieux-Planck function which takes the role of a thermodynamic potential [Röpke, 1987]

$$\Phi(t) = \ln Tr \left\{ e^{-\sum\limits_n F_n(t) A_n} \right\}. \tag{2.81}$$

Comparing (2.80) to (2.71), $e^{\Phi(t)}$ can be regarded as a generalized partition function which is applicable for nonequilibrium states.

At an initial time t_0 it is assumed that the relevant statistical operator contains the complete information needed to describe the system such that $\widehat{\rho}_\epsilon(t_0) = \widehat{\rho}_0(t_0)$. Time dependent mean values of system properties A_n can be calculated from $\widehat{\rho}_0(t)$ at any time in analogy to (2.19) as

$$\langle A(t)\rangle = Tr\{\widehat{\rho}_0(t)\widehat{A}_n\}. \tag{2.82}$$

To obtain the relevant statistical operator $\widehat{\rho}_0(t)$, the procedure of maximizing the entropy can be extended to nonequilibrium situations. But now the information entropy $S_I(t)$ defined by the relevant statistical operator is maximized [Vasconcellos et al., 2005]

$$S_I(t) = -k_B Tr\{\widehat{\rho}_0(t)\ln\widehat{\rho}_0(t)\} \tag{2.83}$$

and additional constraints given by the mean values of relevant quantities A_n apart from the conservation laws must be considered. The corresponding Lagrange multipliers $F_n(t)$ then appear in (2.80).

The so-called nonequilibrium statistical operator method [Vasconcellos et al., 2005] as outlined above can be applied to a multitude of physical systems. With this formalism, the definition of temperature can be expanded to a wide variety of nonequilibrium systems for example in the context of nuclear collisions, ideal and real gases, granular systems, glasses, sheared fluids, amorphous semiconductors and turbulent fluids [Casas-Vazquez and Jou, 2003]. Another example is the application of nonequilibrium statistical operators to study heat transport in a system of bosons [Vasconcellos et al., 1996] or to investigate the transport of energy in fluids for a system of fermions interacting with a boson system [Jou et al., 2001]. Luzzi and coauthors apply this approach to obtain optical properties of highly excited plasmas in semiconducters [Luzzi et al., 1997a, b].

Considering applications of nonequilibrium statistical operators to the radiation field [Vasconcellos et al., 2001; R.Vasconcellos et al., 2001], the Wien displacement law for example can be generalized to nonequilibrium situations [Fort, 1999a]. Treating nonequilibrium radiation as a nonequilibrium photon gas interacting with matter a set of Boltzmann equations for this mixture can be derived [Eu and Mao, 1992]. In this case the Boltzmann collision term contain the irreversible processes such as elastic and inelastic (Compton scattering), collisions between a photon and a matter particle, and emission and absorption processes. With regard to applications in radiation calculations for the atmosphere, the idea of obtaining an anisotropic nonequilibrium emission function by deriving corrections to Plancks law from the statistical oparator method looks promising. Details about a specific example where such corrections are calculated by considering a highly absorbing cavity with a temperature gradient applied [Fort et al., 1999b] are given in Appendix B. However, as is explained there, these corrections to the Planck function are only valid for small deviations of the radiation field from thermodynamic equilibrium [Fort, 1997]. To describe the strong deviations from equilibrium observed in the atmosphere, it would be necessary to retain higher order correction terms or to include additional constraints other than the heat flux and the photon flux discussed in Appendix B [Ramos et al., 2000; Luzzi et al., 1998]. While this procedure is valid in principle, the complexity of the corresponding analytical or numerical calculations prohibit its application to the real atmosphere.

In summary it can be said that the nonequilibrium statistical operator methods based on statistical physics are useful to investigate a number of specific nonequilibrium systems. However, such calculations for the atmospheric nonequilibrium radiation field as illustrated by Fort' s corrections to the Planck function are restricted to weak deviations from thermodynamic equilibrium. Therefore to describe the radiation field in the atmosphere which is

generally far away from thermodynamic equilibrium another approach to simplify the radiation calculations is pursued. As further explained in the next section 2.2.3, if enough inelastic collisions occur to maintain the Boltzmann distribution of the ratio of the number densities of absorber energy levels, the source function equals the Planck function which largely simplifies the radiation calculations. Deviations from this situations are parameterized as isotropic scattering with the single scattering albedo derived from the two-level model.

2.2.3 Deviations from thermodynamic equilibrium; simplifications applied in radiative transfer calculations

In the following, the physical meaning of the concepts of TE, LTE and non-LTE as applied in radiative transfer calculations will be clarified and elucidated. Assuming isotropic scattering (usually valid in clear air calculations [Thomas and Stamnes, 2002], the RTE (2.66) can be written as

$$\vec{n} \cdot \frac{\partial I_\nu(\vec{r},\vec{n})}{\partial \vec{r}} = \rho(\vec{r})\kappa_\nu(\vec{r}) \left\{ -I_\nu(\vec{r},\vec{n}) + \frac{\omega_\nu}{4\pi} \int_0^{4\pi} I_\nu(\vec{r},\vec{n}')d\Omega' + (1-\omega_\nu)B_\nu(T) \right\} \tag{2.84}$$

A general relationship between the monochromatic energy flux density $I_\nu(\vec{r},\vec{n})$ and the spectral energy density of the radiation field is given by [Chandrasekhar, 1960]

$$c\, u_\nu(\vec{r}) = \int_0^{4\pi} I_\nu(\vec{r},\vec{n}')d\Omega'. \tag{2.85}$$

Assuming a hypothetical state of thermodynamic equilibrium (TE) for some fluid and the radiation field such that no gradients of any quantities occur (compare Figure 2.2), the right-hand side of equation (2.84) is zero, the spectral energy density of the radiation field is given by the isotropic black body radiation $u^*_\nu(T)$, and the fluid is described by a global-mean value for temperature and pressure. Comparing (2.64) with (2.85) it can be seen that the intensity of the radiation field corresponds to the Planck function everywhere $[I_\nu(T) = B_\nu(T)]$ in this case. Furthermore, in thermodynamic equilibrium, the source function contains only the thermal emission part and the scattering part vanishes. No radiative heating or cooling rates occur.

Considering a realistic situation, both the atmosphere and the radiation field are in a state far from thermodynamic equilibrium. This means that the spectral energy density is not given by $u^*_\nu(T)$ but would rather depend on a large number of additional parameters, compare Section 2.2.2. Therefore the intensity of the radiation field can no longer be equated to the Planck function. As mentioned in the introduction, the atmosphere too is in a state far from equilibrium due to external solar forcing and other diabatic and dynamic processes. Nevertheless, as already discussed in Section 2.1.1, local thermodynamic equilibrium can be assumed such that the ideal gas law and Maxwell's velocity distribution are valid.

To obtain the radiative energy flux densities (compare (2.59)), the calculations can usually be simplified, at least in the troposphere and lower stratosphere. If the inelastic collision rate between the absorbers and some other molecules in the atmosphere is sufficient to maintain the Boltzmann distribution of the population numbers of the energy levels [Thomas and Stamnes, 2002],

$$\left(\frac{n_2}{n_1}\right)^* = \frac{g_2}{g_1} \exp\left(-\frac{E_2 - E_1}{k_B T}\right), \tag{2.86}$$

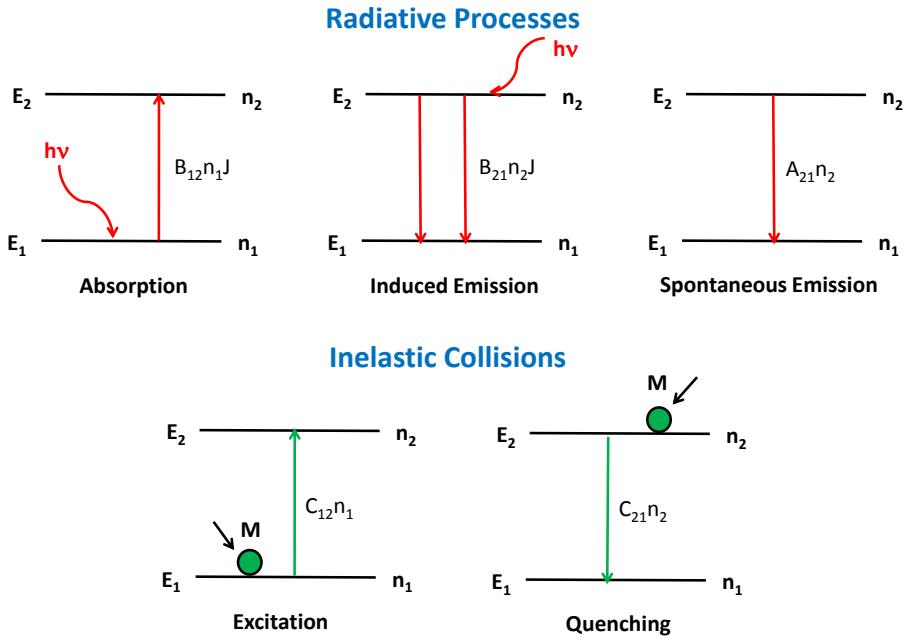

Figure 2.5: Illustration of the processes considered in the statistical equilibrium equation for the two-level model (2.87). J is defined in (2.89) and corresponds to the isotropic scattering part of the source function.

the source function is still given by the Plank function and there is no scattering contribution. In (2.86) T is the temperature of the atmosphere, n_2 is the population number, E_2 the energy and g_2 the statistical weight of the excited state whereas the analog quantities of the ground state are denoted by the lower index taking a value of one. This situation is defined as LTE in the radiative transfer literature. Note that the population numbers n_i of an energy level E_i must not be confused with the occupation numbers of the momentum states of the radiation field in second quantization applied in Chapter 2.2.1.

Due to the exponential decrease of the air density with height the inelastic collisions are less frequent in the middle atmosphere such that (2.86) is no longer valid above the stratopause. In this case, an additional term in the form of isotropic scattering appears in the source function at the expense of thermal emission, leading to a situation termed non-LTE. A motivation for parameterizing non-LTE effects as isotropic scattering is given below by applying the two-level model. By comparing the statistical equilibrium equation for the two-level model to the macroscopic radiative transfer equation, an expression for the single scattering albedo ω_ν is derived. This parameter describes the relative importance of the thermal emission compared to the scattering contribution in the source function. This is the method used to include non-LTE in the new radiation scheme presented in this work, as will be described in Chapter 3.3.

The derivation of the source function of the two-level model follows the text of Thomas and Stamnes [Thomas and Stamnes, 2002]. In the two-level model only two energy levels (ground state 1 and the excited state 2) are considered to model a monochromatic transition. The population numbers of these two energy levels are assumed to depend on the three radiative processes of (induced) absorption, induced emission, and spontaneous emission as well as on collisional excitation and quenching (see Figure 2.5). The population number of the excited

state is obtained from the so-called statistical equilibrium equation

$$n_1 C_{12} + n_1 B_{12} \int_0^\infty d\nu \Phi(\nu) \bar{I}_\nu = n_2 C_{21} + n_2 B_{21} \int_0^\infty d\nu \Phi(\nu) \bar{I}_\nu + n_2 A_{21}. \tag{2.87}$$

The interpretation of (2.87) is as follows. The excited level 2 can be populated by collisional excitation or absorption of radiation (left-hand side); and it gets depleted by the processes of collisional quenching, induced emission and spontaneous emission (right-hand side). Here, $\bar{I}_\nu$ denotes the monochromatic intensity averaged over all directions,

$$\bar{I}_\nu(\vec{r}, t) = \frac{1}{4\pi} \int_{4\pi} I_\nu(\vec{r}, \vec{n}, t) d\Omega, \tag{2.88}$$

ν is the frequency which corresponds to the energy difference $h\nu$ between the two levels considered, and $\Phi(\nu)$ is the line profile. The n_i are the population numbers of the energy levels, C_{12} and C_{21} are the inelastic collision rates for excitation and quenching, B_{12} and B_{21} are Einstein's coefficients for induced absorption and emission, respectively, and A_{21} is Einstein's coefficient of spontaneous emission. Defining

$$J \doteq \int_0^\infty d\nu \Phi(\nu) \bar{I}_\nu(\vec{r}, t), \tag{2.89}$$

which, as will be seen below, corresponds to the isotropic scattering contribution to the source function, the Einstein coefficients B_{21} multiplied by J gives the transition probability w_{21} per second from the excited level 2 to the ground state 1 due to induced emission,

$$w_{21} = B_{21} J. \tag{2.90}$$

This transition probability is proportional to the matrix element $\langle \phi_1 | \widehat{H'}(t) | \phi_2 \rangle$ squared of the transition considered and can be calculated from quantum mechanics [Röpke, 1983]. $\widehat{H'}(t)$ is the perturbation Hamilton operator corresponding to electromagnetic dipole radiation for example. The B_{21} and B_{12} are related to each other and to the coefficient for spontaneous emission A_{21} by the so-called Einstein relations [Thomas and Stamnes, 2002]

$$\begin{aligned} A_{21} &= \frac{2h\nu^3}{c^2} B_{21} \\ g_1 B_{12} &= g_2 B_{21}. \end{aligned} \tag{2.91}$$

The inelastic collision rate for excitation C_{12} can be written as the product of the amount of collision partners $[M]$ times the collisional excitation coefficient k_{12}

$$C_{12} = [M] k_{12}. \tag{2.92}$$

Assuming binary collisions, the excitation coefficient depends on the magnitude of the velocity difference between the absorber ($\vec{v}_a$) and the collision partner ($\vec{v}_M$) and on the differential inelastic scattering cross-section (compare the collision term (2.43) applied in the Boltzmann equation (2.44) without the loss term)

$$k_{in} = \int d|\vec{v}_a - \vec{v}_M| f_a(\vec{x}, \vec{v}_a) f_M(\vec{x}, \vec{v}_M) \frac{d\sigma_{in}}{d\Omega}. \tag{2.93}$$

Since the atmospheric gas is in LTE, the velocity distribution functions are given by Maxwell's velocity distribution and the collision rates are related to each other by the law of detailed balance

$$n_2 C_{21} = n_1 C_{12}. \tag{2.94}$$

The same argument implies that it is allowed to relate the rates of the two collision processes by invoking the Boltzmann distribution (2.86) such that C_{21} can be calculated as

$$C_{21} = C_{12} \frac{g_1}{g_2} \exp\left(\frac{h\nu}{k_B T}\right). \tag{2.95}$$

The definitions and concepts explained above will now be applied to derive the monochromatic two-level non-LTE source function S_ν for the transition considered in two steps. First, only induced emission and absorption as well as spontaneous emission are considered. The rate at which radiative energy is gained or lost along a light beam can then be assigned to these microscopic radiative processes to obtain the so-called microscopic radiative transfer equation, compare [Thomas and Stamnes, 2002] p.106,

$$\vec{n} \cdot \frac{\partial I_\nu(\vec{r},\vec{n})}{\partial \vec{r}} = -\frac{h\nu}{4\pi} n_1 B_{12} I_\nu(\vec{r},\vec{n})\Phi(\nu) + \frac{h\nu}{4\pi} n_2 B_{21} I_\nu(\vec{r},\vec{n})\Phi(\nu) + \frac{h\nu}{4\pi} n_2 A_{21}\Phi(\nu). \tag{2.96}$$

Comparing this equation to the macroscopic RTE (2.66) and assuming the same line profile $\Phi(\nu)$ for all of the three radiative processes (complete frequency redistribution) leads to the following intermediate expression for the source function

$$S_\nu = \frac{n_2 A_{21}}{n_1 B_{12} - n_2 B_{21}} = \frac{2h\nu^3/c^2}{(n_1 g_2/n_2 g_1) - 1}. \tag{2.97}$$

This equation still contains the ratio of the population numbers (n_1/n_2) of the energy levels which is unknown in general situations. To eliminate the ratio of the population numbers, the two-level statistical equilibrium equation (2.87) including now the collision processes is considered. By solving this equation an expression for the term $\frac{n_1 g_2}{n_2 g_1}$, which appears in the denominator of (2.97), is obtained

$$\frac{n_1 g_2}{n_2 g_1} = \frac{A_{21} + B_{21} J + C_{21}}{B_{21} J + C_{21} \exp\left(-\frac{h\nu}{k_B T}\right)}. \tag{2.98}$$

Substituting this back into (2.97) leads, after some additional manipulations, to the final result for the two-level monochromatic non-LTE source function

$$S_\nu = \varepsilon_\nu B_\nu(T) + (1 - \varepsilon_\nu) J. \tag{2.99}$$

Here, the definition of the so-called coupling parameter

$$\varepsilon_\nu = \frac{C_{21}}{C_{21} + A_{21}(1 - \exp(\frac{h\nu}{k_B T}))^{-1}} \tag{2.100}$$

is used. Noting that J corresponds to the scattering part of the source function (2.62), the single scattering albedo needed to allow for non-LTE in the new radiation scheme is given by $\omega_\nu = 1 - \varepsilon_\nu$.

A physical motivation to describe deviations from LTE using the single scattering albedo can be thought of in the following way. In the case of non-LTE, absorption is less efficient

than in LTE because the radiatively active molecules partly remain in their excited state due to the insufficient frequency of inelastic collisions. In the same fashion, also thermal emission is less efficient because a depopulated excited state will not quickly enough be repopulated due to inelastic collisions. The overall result is that the macroscopic description of radiative transfer for a particular frequency in non-LTE will invoke the concept of virtual states and isotropic scattering, instead of pure thermal absorption and emission according to Kirchhoff's law, which applies in strict LTE. Hence, the degree of non-LTE corresponds to the relative importance of isotropic scattering in the source function (2.67) given by the value of the single scattering albedo, which is zero in LTE and equal one in complete non-LTE.

2.3 Conventional solution methods of the radiative transfer equation to obtain the radiative heating rates

To compare the new radiation scheme presented in this work with comprehensive radiative transfer calculations from the literature and to highlight some advantages of the new method, an (not all-encompassing) overview of conventional solution methods of the radiative transfer problem is presented in this section. Due to the fact that in the SW regime only a simple absorption law is applied in the new radiation scheme, comprehensive solar radiation calculations are only shortly mentioned. Concerning the LW regime, the Curtis matrix calculation of heating rates is explained in some more detail. Thereafter some general issues important for the evaluation of the flux transmission functions appearing in the Curtis matrix formalism are discussed. Finally two approaches conventionally applied to allow for non-LTE in the middle atmosphere are mentioned.

2.3.1 Overview

Most of the conventional radiation schemes designed for use in atmospheric circulation models start from the vertically integrated stationary radiative transfer equation (2.66). To simplify the solution of this equation, the plane-parallel approximation is usually invoked, see Chapter 2.3.2.

In the thermal (or long-wave) regime up to the stratopause, clear-sky conditions and local thermodynamic equilibrium are assumed. The resulting expressions for the radiative heating rates can be expressed in terms of derivatives of so-called flux transmission functions, which include integrations over frequency, zenith angle ϑ, and height [Andrews et al., 1987], Chapter 2.4. Corresponding numerical methods are known as Curtis-matrix formulations. In state-of-the art schemes, also tropospheric clouds, which contribute to the greenhouse-effect, are accounted for. Furthermore, the deviation from LTE (non-LTE), which is relevant in the mesosphere and higher up, has been successfully included in the matrix formalism by applying appropriate source functions [Lopez-Puertas and Taylor, 2001]) and validated against line-by-line calculations [Fomichev et al., 1986; Fomichev and Shved, 1988, 1994; Fomichev and Blanchet, 1995]. An alternative approach to calculate the radiation field under non-LTE conditions is to iterate between the vertically integrated RTE and the so-called statistical equilibrium equations [Kutepov et al., 1998].

In calculations of the SW (short-wave) heating rates, the incoming solar flux must be considered while thermal emission is neglected. Allowing for absorption of the direct solar radiation in clear air atmospheres leads to height and frequency dependent heating rate maxima (Chapman layers) [Andrews et al., 1987], Chapter 2.7. Comprehensive methods to solve the radiation problem in the SW regime include scattering on aerosols, clouds, and air molecules and allow for reflection at the surface [Liou, 2002]. Non-LTE in the SW regime

[1] can be established by considering appropriate efficiencies for the conversion of absorbed solar radiation to kinetic energy of the atmospheric constituents [Landsberg, 1980]. In the approach of discrete ordinates, the appropriate RTE is solved for different discrete zenith directions. The principle of invariance and the adding method apply some kind of ray tracing for the incoming solar beam inside an atmospheric layer in order to calculate the emerging radiation at the upper and lower boundary of the layer.

2.3.2 Curtis matrix formulation

In this section a more detailed description of how radiative temperature tendencies can be obtained using flux transmission functions and the Curtis matrix method are given in the following. To simplify the RTE (2.66) with the source function given by (2.67) further, the so-called plane-parallel approximation is usually assumed. This means that the position vector $\vec{r}$ is replaced by some vertical coordinate and that horizontal gradients of the radiative energy fluxes are neglected. In addition, the directional dependence on the azimuth φ can be neglected in the LW regime, see the right panel of Figure 2.4 for the geometry of the coordinates. Invoking the hydrostatic approximation ($\frac{\partial p}{\partial z} = -\rho g$) pressure p can be used as vertical coordinate. The resulting azimuth independent plan parallel transfer equation depends solely on pressure and the zenith angle ϑ

$$\begin{aligned} \cos\vartheta \frac{\partial I_\nu(p,\vartheta)}{\partial p} &= \frac{\kappa_\nu}{g}\Big(- I_\nu(p,\vartheta) + (\,1 - \omega_\nu(\vec{r})\,)\, B_\nu(T) \\ &\quad + \frac{\omega_\nu(\vec{r})}{2}\int I_\nu(p,\vartheta)\, \sin\vartheta d\vartheta\Big). \end{aligned} \tag{2.101}$$

Note that to shorten the notation, the dependence of temperature on the vertical pressure coordinate $T(p)$ is suppressed hereafter in the Planck function. In the thermal regime up to the mesosphere and assuming clear sky conditions, scattering can be neglected in LTE ($\omega_\nu = 0$) as explained above. This leads to

$$\cos\vartheta \frac{\partial I_\nu(p,\vartheta)}{\partial p} = \frac{\kappa_\nu}{g}\Big(- I_\nu(p,\vartheta) + B_\nu(T)\Big). \tag{2.102}$$

Integrating this equation vertically and over both hemispheres leads to the following integral equations for the upward and downward monochromatic intensities (in pressure coordinates):

$$\begin{aligned} I_{\nu,\uparrow}(p,\vartheta) &= I_{\nu,\uparrow}(p_s,\vartheta)\exp\{-(\tau_\nu(p,p_s,\cos\vartheta))\} \\ &\quad + \int_p^{p_s} \frac{\kappa_\nu(p')}{g\cos\vartheta} B_\nu(T')\exp\big\{-(\tau_\nu(p,p',\cos\vartheta))\big\}dp' \end{aligned} \tag{2.103}$$

$$I_{\nu,\downarrow}(p,\vartheta) = -\int_0^{p} \frac{\kappa_\nu(p')}{g\cos\vartheta} B_\nu(T')\exp\big\{-(\tau_\nu(p,p',\cos\vartheta))\big\}dp' \tag{2.104}$$

with

$$\tau_\nu(p_1,p_2,\cos\vartheta) = \int_{p_1}^{p_2} \frac{1}{\cos\vartheta}\kappa_\nu(p)\frac{dp}{g}. \tag{2.105}$$

[1] In addition to the definition of non-LTE in the LW regime, compare Chapter (2.2.3), this term is sometimes also used when the absorbed SW radiation is not directly thermalized. Note, however, that with regard to the general definition of non-LTE in radiative transfer, the SW regime is generally in non-LTE.

Here, $\kappa_\nu(p)$ is the monochromatic extinction coefficient and τ_ν is the optical path from the pressure level p_1 to p_2. The upward monochromatic intensity measured at pressure level p consists of the radiation emitted at the surface, which is reduced due to absorption in the underlying atmosphere, plus the radiation emitted and transmitted from all of the underlying atmospheric layers. Assuming no incoming long-wave radiation from space, the downward intensity at a pressure level p contains just the radiation emitted and transmitted through the overlying atmosphere.

To get the LW upward U and downward D radiative energy flux densities needed to calculate the radiative temperature tendencies in the atmosphere (2.59) and at the surface (2.60) for a whole absorber band k instead of a single monochromatic line, (2.103) and (2.104) must be integrated over the corresponding frequency range and over the zenith direction. To simplify the notation of these integrals, so-called transmission functions are usually defined.

The monochromatic transmission function $T_\nu(p_1, p_2, \cos\vartheta)$ gives the fractional part of the intensity for a light beam transmitted in the direction ϑ from p_1 to p_2

$$T_\nu(p_1, p_2, \cos\vartheta) = \exp\{-(\tau_\nu(p_1, p_2, \cos\vartheta))\}. \tag{2.106}$$

A first integration of the monochromatic transmission function over the frequency range (from ν_{k2} to ν_{k1}) of a band k leads to the band transmission function

$$\overline{T}^k(p_1, p_2, \cos\vartheta) = \frac{1}{\nu_{k2} - \nu_{k1}} \int_{\nu_{k1}}^{\nu_{k2}} T_\nu(p_1, p_2, \cos\vartheta) d\nu. \tag{2.107}$$

Related quantities often used in the literature are the so-called band absorptivity

$$\overline{A}^k(p_1, p_2, \cos\vartheta) = 1 - \overline{T}^k(p_1, p_2, \cos\vartheta) \tag{2.108}$$

or the equivalent width

$$\overline{W}^k(p_1, p_2, \cos\vartheta) = (\nu_{k2} - \nu_{k1})\overline{A}^k(p_1, p_2, \cos\vartheta). \tag{2.109}$$

A second integration of the band transmission function over the half sphere finally gives the flux transmission function $\overline{T}_f^k(p_1, p_2)$

$$\overline{T}_f^k(p_1, p_2) = 2\pi \int_0^1 \cos\vartheta \, \overline{T}^k(p_1, p_2, \cos\vartheta) d\cos\vartheta. \tag{2.110}$$

Applying this definition of the flux transmission function in (2.103) and (2.104) and carrying out the two integrations, the upward and downward radiative energy flux densities can be written as

$$U^k(p) = B^k(T_s)\overline{T}_f^k(p, p_s) - \int_p^{p_s} B^k(T') \frac{\partial \overline{T}_f^k(p, p')}{\partial p'} dp' \tag{2.111}$$

and

$$D^k(p) = \int_0^p B^k(T') \frac{\partial \overline{T}_f^k(p, p')}{\partial p'} dp'. \tag{2.112}$$

From the upward and downward energy flux density the radiative temperature tendency of a band k can then be calculated as

$$\left(\frac{\partial}{\partial t} T\right)_{rad}^k (p) = \frac{g}{c_p} \frac{\partial}{\partial p} \left\{ U^k(p) - D^k(p) \right\}, \tag{2.113}$$

leading to

$$\left(\frac{\partial}{\partial t}T\right)^k_{rad}(p) = \frac{g}{c_p}\left\{B^k(T_s)\frac{\partial\overline{T}^k_f(p,p_s)}{\partial p} - \int_p^{p_s} B^k(T')\frac{\partial^2\overline{T}^k_f(p,p')}{\partial p\partial p'}dp' - \int_0^{p} B^k(T')\frac{\partial^2\overline{T}^k_f(p,p')}{\partial p\partial p'}dp'\right\}$$

Adding and subtracting the two integrals $\int_0^{p_s} B^k(T)\frac{\partial^2\overline{T}^k_f(p,p')}{\partial p\partial p'}dp'$ and $\int_0^{p} B^k(T)dp'$, the radiative temperature tendency at a pressure level p for a band k can be written in the exchange integral formulation

$$\begin{aligned}\left(\frac{\partial}{\partial t}T\right)^k_{rad}(p) &= -\frac{g}{c_p}B^k(T)\frac{\partial\overline{T}^k_f(p,0)}{\partial p}\\ &\quad +\frac{g}{c_p}(B^k(T_s)-B^k(T))\frac{\partial\overline{T}^k_f(p,p_s)}{\partial p}\\ &\quad -\frac{g}{c_p}\int_p^{p_s}(B^k(T')-B^k(T))\frac{\partial^2\overline{T}^k_f(p,p')}{\partial p\partial p'}dp'\\ &\quad -\frac{g}{c_p}\int_0^{p}(B^k(T')-B^k(T))\frac{\partial^2\overline{T}^k_f(p,p')}{\partial p\partial p'}dp'. \qquad (2.114)\end{aligned}$$

The first term on the right hand side of (2.114) describes the contribution to the temperature tendency as a result of emission from the level p directly to space (cooling to space term). The direct exchange of radiation between the surface and the level p is given in the second term (usually a heating term). The last two expressions describe contributions to the temperature tendency due to exchanges with atmospheric layers below and above the level considered.

To numerically calculate radiative temperature tendencies in radiation models, (2.114) can be reformulated decomposing the Planck function at a pressure level p' into a sum of contributions from all of the other levels p_j constituting the model domain

$$B^k(T(p')) = \sum_j a_j(p',p_j)B^k(T(p_j)). \qquad (2.115)$$

Inserting this decomposition into (2.114) results in the Curtis matrix formulation of the radiative temperature tendency; see for example [Zhu and Strobel, 1991; Zhu, 1993]

$$\left(\frac{\partial}{\partial t}T\right)^k_{rad}(p_i) = \sum_j R_{ij}\,B^k(T(p_j)). \qquad (2.116)$$

Note that in the above equation the cooling to space term and the interaction with the surface are not included. The Curtis matrix element R_{ij} contains the contribution to the temperature tendency at level i due to emission from level j

$$R_{ij}(p_i,p_j) = \frac{g}{c_p}\int a_j(p',p_j)\frac{\partial^2\overline{T}^k_f(p_i,p')}{\partial p\partial p'}dp' \qquad (2.117)$$

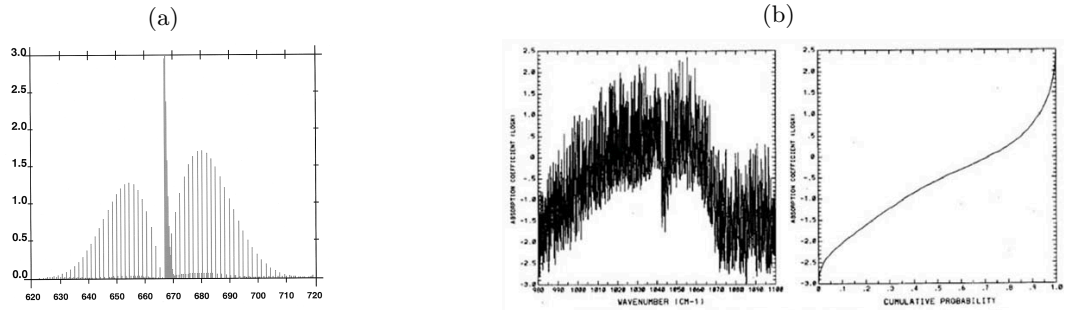

Figure 2.6: (a) The wavenumber (cm^{-1}) spectrum of the CO_2 15 μm band in units of ($10^{-19} cm^2 mol^{-1}$) from HITRAN 2004 [Rothman et al., 2004], and (b) (the wavenumber spectrum of the ozone 15 μm band in units of (cm^{-1}atm) mapped to the cumulative probability

2.3.3 Evaluation of the flux transmission functions

The flux transmission functions appearing in the exchange integral formulation (2.114) or in the Curtis matrix elements (2.117) are generally very complicated and can be evaluated only by applying strong simplifications and approximations. To evaluate the frequency integral needed for calculating the band transmission functions, the most accurate but most tedious method is to integrate the absorption coefficient over all lines in a band applying frequency intervals smaller than the line half-with (line-by-line calculations) [Clough et al., 1992; Clough and Iocono, 1995]. This is illustrated for the spectrum of the CO_2 15 μm band in Figure 2.6, panel (a). To avoid such cumbersome line-by-line calculations, band models, such as the Elsasser band which will be used in this work (compare Chapter 3.1) can be defined to develop analytical expressions for the band transmission function or other related quantities which describe the absorption characteristics of a band [Thomas and Stamnes, 2002; Liou, 2002]. In different band models, the integration over an absorber band is simplified by assumptions concerning the density, strength, distribution and form of the lines in the respective frequency range. For non overlapping Lorentz lines, the band absorptivity can be described by the Ladenberg-Reiche function or some assumptions about the probability distribution of line strength can be prescribed to compute the band absorptivity. If line overlap is important, random models for the positions of the line centers, such as the Goody or Malkmus model, can be used for relatively narrow frequency bands to calculate band transmission functions. The exponential sum fit can be applied to describe the equivalent width of weak broad bands, whereas for strong broad bands, a flux emissivity formulation can be applied. Another approach to simplify the frequency integration is the so-called correlated k-distribution method, compare panel (b) of Figure 2.6. The correlated k-distribution maps the integration in frequency space to the cumulative distribution of the absorption coefficient in a band, to get much smoother integrands. For vertically inhomogeneous atmospheres, these distribution functions of the absorption coefficients k are assumed to be correlated in adjacent layers [Mlawer et al., 1997].

Concerning the angular (zenith) integration, the diffuse flux factor approximation applying a mean value for the cosine of the zenith angle can be used in the troposphere and stratosphere. For this purpose, a constant diffusivity factor r

$$r \doteq 1/\bar{\mu} = 1/\cos\vartheta \approx \frac{3}{5} \tag{2.118}$$

can be defined [Thomas and Stamnes, 2002]. In addition to the two integrations needed to obtain the flux transmission-function, the pressure and temperature dependence of the

absorption coefficient must be adequately considered to compute transmission functions along a varying optical path. Therefore the flux transmission-functions depend strongly on the thermodynamic state of the atmosphere. The monochromatic absorption coefficient can be written as the product of a temperature dependent line strength S and the line profile f

$$\kappa_\nu(p,T) = S_\nu(T) \cdot f(\nu,T,p). \tag{2.119}$$

The line strength $S_\nu(T)$ and the Voigt profile $f(\nu,T,p)$ can be calculated from spectroscopic databases such as HITRAN for example [Rothman et al., 2004, 2009]. Applying radiative temperature tendency calculations in general circulation models, the flux transmission functions or Curtis matrices must be recalculated after every time step and at each position in the atmosphere. Therefore, some authors use prescribed Curtis matrices corresponding to a standard set of temperatures and pressure values and apply interpolations between these reference states to obtain the radiative temperature tendencies corresponding to intermediate states of the atmosphere [Zhu and Strobel, 1991; Zhu, 1993].

2.3.4 Non-LTE calculations in conventional methods

Neglecting the reduction of the efficiency in both emission and absorption due to the decreasing number of inelastic collisions in the upper atmosphere would result in an excessive unrealistic cooling rate for the CO_2 15μm band of about 100 Kd^{-1} in the thermosphere. Considering the Curtis matrix approach to calculate the radiative heating rate non-LTE can easily be included into the formalism by substituting the Planck function in (2.116) by a generalized band source function at each level $S^k(p_j)$ [Lopez-Puertas and Taylor, 2001]

$$\left(\frac{\partial}{\partial t}T\right)^k_{rad}(p_i) = \sum_j R_{ij} S^k(p_j). \tag{2.120}$$

The band source function $S^k(p_j)$ can for example be derived from the two-level model (2.99) or from more sophisticated calculations including additional processes that populate and deplete the excited energy level(s). This method has been validated against line-by-line calculations for instance by Fomichev [Fomichev et al., 1986; Fomichev and Shved, 1988, 1994; Fomichev and Blanchet, 1995].

Another approach to calculate the radiation field under non-LTE conditions is to iterate between the vertically integrated RTE and the statistical equilibrium equations [Kutepov et al., 1998]. Generally, the Planck function appearing in the upward and downward monochromatic intensities must be replaced by a more general source function $S_\nu(p)$ to allow for non-LTE

$$\begin{aligned} I_{\nu,\uparrow}(p,\vartheta) &= I_{\nu,\uparrow}(p_s,\vartheta)\exp\{-(\tau_\nu(p,p_s,\cos\vartheta))\} \\ &\quad + \int_p^{p_s} \frac{\kappa_{a,\nu}(p')}{g} S_\nu(p) \exp\big\{-(\tau_\nu(p,p',\cos\vartheta))\big\} dp' \end{aligned} \tag{2.121}$$

$$I_{\nu,\downarrow}(p,\vartheta) = -\int_0^{p} \frac{\kappa_{a,\nu}(p')}{g} S_\nu(p') \exp\big\{-(\tau_\nu(p',p,\cos\vartheta))\big\} dp'. \tag{2.122}$$

This source function depends on the population numbers of the energy levels that belong to the transition considered as can be seen for example in the two-level model (compare Chapter 2.2.3),

$$S_\nu = \frac{n_2 A_{21}}{n_1 B_{12} - n_2 B_{21}} = \frac{2h\nu^3/c^2}{(n_1 g_2/n_2 g_1) - 1}. \tag{2.123}$$

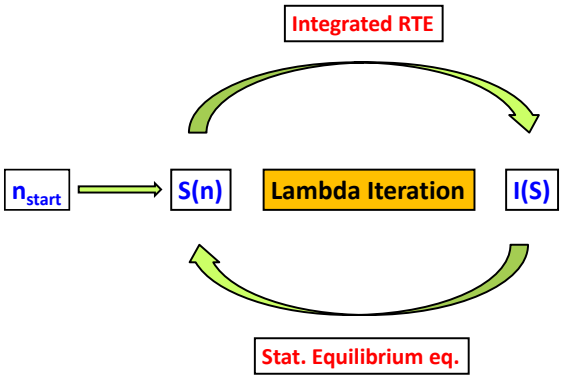

Figure 2.7: The lambda iteration method to calculate the non-LTE radiation field. It is initialized with some prescribed population numbers n from which the source function S is calculated. From this source function, the upward and downward intensities are obtained from the integrated RTE, compare (2.121) and (2.122). Substituting the directionally averaged intensity back into the statistical equilibrium equation, the source function can be updated. This process is repeated until some criterion for convergence is satisfied.

The population numbers appearing in the source function are calculated using the appropriate statistical equilibrium equation which should include all of the relevant processes. Using (2.87) for the two-level model this leads to

$$\frac{n_1}{n_2} = \frac{A_{21} + B_{21}J + C_{21}}{(g_2/g_1)C_{21}e^{-h\nu/k_BT} + (g_2/g_1)B_{21}J} \tag{2.124}$$

with

$$J \doteq \int_0^\infty d\nu \Phi(\nu) \bar{I}_\nu. \tag{2.125}$$

The mutual dependence of the directionally averaged intensity $\overline{I}_\nu$ and the source function can be written down defining the lambda operator Λ

$$\overline{I}_\nu = \Lambda\left[S_\nu\right] \tag{2.126}$$

The lambda operator depends nonlocally on all of the atmospheric layers considered. Invoking some kind of local approximation leads to the so-called Accelerated Lambda Iteration (ALI) methods [Kutepov et al., 1998]. The iteration is initialized applying some prescribed population numbers (or vibration temperatures, compare (2.127)) below from which an initial source function is calculated. This source function is then used to calculate the radiation field, from which a new updated source function is obtained by applying again the statistical equilibrium equation, see Figure 2.7. Using ALI methods, the same technical difficulties known from flux transmission function calculations namely an integration over the zenith direction to calculate the directionally averaged intensity appearing in (2.87) and the frequency integration to avoid line-by-line calculations must be considered. The pressure and temperature dependence of the absorption coefficient remains an issue to be dealt with too. The accuracy achieved for the heating rates calculated using the Lambda iteration depends on the

simplifications used to locally approximate the lambda operator. In addition, convergence of the iteration can not always be guaranteed [Wintersteiner et al., 1992].

Another method to describe the radiation field far from equilibrium is to consider each light beam as a distinct thermodynamic subsystem characterized by its specific radiative temperature [Callies and Herbert, 1988a, b; Herbert and Pelkowski, 1990; Kutepov et al., 1998]. In strong nonequilibrium the different monochromatic light beams propagating in specific directions must be described by their own radiation temperatures which may differ from each other and from the local kinetic temperature of the atmospheric gas.

In general, the radiation temperature $T_{\nu,rad}$ for a single transition between two energy levels is defined as

$$T_{\nu,rad} \doteq -\frac{E_2 - E_1}{k_B \ln\left(\frac{n_2 g_1}{n_1 g_2}\right)}. \tag{2.127}$$

It depends on the energy difference between the excited and the ground state $E_2 - E_1$, the population numbers n_2 and n_1 of the excited and the ground state, and on the degeneracies g_2 and g_1 of the two states. For non-LTE, the population numbers are not Boltzmann distributed, but must be determined from a statistical equilibrium equation which includes all of the relevant processes that populate and deplete the excited level. Radiative temperatures are often applied in the context the Lambda iterations discussed above [Kutepov et al., 1998; Wintersteiner et al., 1992].

Considering a vibration-rotation band, different degrees of deviations from LTE can be distinguished. Since the energy levels of vibrational transitions are farther separated than the rotational energy levels, the population numbers corresponding to a vibrational transition start to deviate from the Boltzmann distribution lower in the atmosphere whereas (2.86) is still valid for the rotational substructure of the band (vibrational non-LTE). Farther up in the atmosphere the air density becomes so low that even the Boltzmann distribution of the population numbers for the more narrowly spaced rotational energy levels is no longer maintained (rotational non-LTE). Therefore, in situations where only vibrational non-LTE must be considered, the calculation of appropriate source functions or radiation temperatures can often be simplified by modeling the spectrum of a rotation-vibration band by a small number of approximate energy levels (applying a so-called multilevel approach [Lopez-Puertas and Taylor, 2001]).

Apart from the case of the CO_2 15 μm band, non-LTE considerations are indispensable for other long-wave bands too [Lopez-Puertas and Taylor, 2001]. For the ozone 9.6 μm band, the difference between the vibrational temperature and the kinetic temperature begins to be important above the stratopause and reaches a maximum value above 80 km, see Figure 2 and 3 in [Manuilova et al., 1998]. The vibrational temperature of the water vapor 6.3 μm band is larger than the kinetic temperature above about 60 km [Lopez-Puertas et al., 1998], whereas for the water vapor rotation continuum LTE is assumed to hold up to much higher atmospheric levels than for the vibrational bands [Kutepov et al., 1998].

Chapter 3

The simplified radiation scheme

Such complex transfer schemes as described in Chapter 2.3 are frequently used in state-of-the-art middle atmosphere GCMs [Beagley et al., 1997; Fomichev et al., 2002; Schmidt et al., 2006; Garcia et al., 2007; Richter et al., 2008]. However, due to the history of comprehensive GCMs and the inherent difficulties in the evaluations of the flux transmission functions (2.110), the radiation block is usually composed of parameterizations in the LW-regime that are distinct for the troposphere/lower stratosphere and the model domain farther above [Richter et al., 2008]; [Garcia et al., 2007; Schmidt et al., 2006; Wehrbein and Leovy, 1982]. Only the resulting heating rates of the distinct schemes are merged in the stratosphere [Fomichev et al., 2002]. In the WACCM3 model, different radiation schemes are even applied for distinct frequency bands and absorbers [Collins et al., 2004]. To calculate the cooling rates in the CO_2 15 μm band, Fomichev and Blanchet apply three separate parameterizations in three distinct height regions [Fomichev and Blanchet, 1998]. Finally, also the time step used to update the radiative heating rates is often much longer than the time step for the dynamical core [Roeckner et al., 2003].

Therefore, in this chapter a new method to compute the radiative flux densities and heating rates is presented. The goal is to do high resolution (T300/L200) simulations simultaneously of both the dynamics and the radiation applying a mechanistic general circulation model. Therefore, the new radiation parameterization should be numerically efficient and extend continuously from the surface (given by a swamp ocean) up to the lower thermosphere. In addition it should be comprehensible and simple enough such that the physical effects included can be fully understood and tested separately in sensitivity studies. Nevertheless, all of the relevant physical processes must be consistently included in the radiation parameterization. The strategy persued here is to account for the fundamental differences between the troposphere and middle atmosphere with regard to the radiative transfer problem in a general and straight-forward fashion, i.e. by one set of transfer equations that holds for the entire altitude range from the surface to the mesopause region. In contrast to conventional methods described in the previous section 2.3, all the necessary approximations and simplifications to arrive at a system of transfer equations for the radiative energy fluxes are introduced first. The numerical integration of these equations over the optical path is then performed as the last step.

The basic idea for the LW-regime derives from the aforementioned (see section 1) approach of Frierson and Held [Frierson et al., 2006, 2007] who used a highly idealized heating due to solar insolation and a broad-band Eddington approximation for the LW regime in the gray limit. Their approach for the LW-regime (see also [Held, 1982]) is equivalent to the 2-stream approximation and results in simple RTEs for the upward and downward energy flux densities that can be solved with negligible computational costs. To extend this concept into the

middle atmosphere, several approximations must be relaxed and corresponding parameterizations must be specified. For example, when using the Eddington approximation for the directional dependence of the LW radiation, the single scattering albedo must be retained as a dynamic variable in order to properly represent non-LTE effects. Furthermore, the broad-band approximation is no longer appropriate and the LW energy flux densities must be calculated for certain distinct frequency bands. These frequency bands must represent the most important absorbers (CO_2, O_3, and H_2O) important to determine the radiative heating rates in the middle atmosphere. As a consequence, one also has to abolish the gray-limit approximation which neglects the frequency variation of the absorption coefficient inside the particular frequency bands defined. In the new radiation scheme, these effects are allowed for by parameterizing the covariance terms which result from frequency variations of the intensity and absorption coefficient within a band. Nonetheless, this still leads to a set of simplified RTEs as the final formal result of the new concept for the LW-regime. As a last step, the simplified RTEs are integrated numerically with regard to the vertical discretization of the circulation model in order to obtain the LW radiative energy flux densities and corresponding heating rates. The fact that all of the needed approximations and parameterizations are introduced first and the vertical integration of the resulting RTEs is performed as a last step is the major difference of the new LW transfer scheme to the aforementioned Curtis-matrix or Lambda-Iteration methods [Kutepov et al., 1998], which work quite the other way round. Other differences are due to the very simple choice of broad frequency bands, application of the simple Elsasser band model to parameterize deviations from the gray limit, and the assumption of the Eddington approximation to integrate over the zenith angle. Non-LTE is included by the single scattering albedo which is calculated from the two-level model for each band. To obtain the SW heating rates, the solar flux at the top of the atmosphere is split into five broad energetically defined bands. The incoming solar radiation is absorbed in four of these bands according too the Beer-Bougert-Lambert law. One short-wave band is assumed to mimic dissociation of mesospheric O_2, two bands are attributed to absorption by O_3 and one band describes absorption by H_2O. The energy contained in the fifth band is assumed to be transmitted directly to the surface.

Compared to comprehensive radiation schemes implemented in other general circulation models including the middle atmosphere, the new method applied in this study leads to some valuable advantages for the purpose persued with a mechanistic circulation model. The continuous computation of the LW and SW radiative energy flux densities allows for a consistent consideration of the surface energy budget and of the radiation budget at the top of the atmosphere (TOA). This continuity is important as well for studies of coupling processes between different height regions.

With the new radiation scheme it is not necessary to introduce additional approximations and simplifications to evaluate complicated and non-local flux transmission functions as given for example in (2.110). The radiative heat fluxes and heating rates can be calculated for each state of the atmosphere without resorting to interpolations between prescribed reference states as is done for example when using matrix methods [Zhu, 1994]. The new parameterization is unified and extends over the whole model domain and frequency bands considered. The physical processes dominating in different height regions are consistently included.

3.1 The LW regime

In this section, Eddington-type band mean transfer equations for the broad long-wave bands applied in the new radiation scheme will be derived. To account for the frequency variation

inside each band some kind of "Reynolds decomposition" is applied to the radiative variables. This leads to an additional set of transfer equations for the perturbation radiative fluxes that is closed in first order using the Elsasser band model. Deviations from local thermodynamic equilibrium are included in terms of isotropic scattering, calculating a mean single scattering albedo from the coupling parameter of the two-level model (2.100) for each band. The mean and perturbation transfer equations are then solved iteratively applying finite differences for the vertical discretization.

Starting point to derive the Eddington equations is the stationary RTE [Chandrasekhar, 1960] (2.66) with the source function (2.67), which corresponds to the assumption of a clear air atmosphere. As explained in Chapter 2.3.2, the plane-parallel approximation is invoked, the azimuth-dependence is neglected, and pressure coordinates are applied to describe the vertical dependence. However, in contrast to conventional solution methods for the LW regime, the single scattering albedo is retained as the non-LTE parameter in the new radiation scheme.

To further simplify the scattering integral in the plane-parallel azimuth-independent equation (2.101), the Eddington approximation is used to parameterize the zenith dependence of the intensity [Liou, 2002] Chapter 6.5.2. This means we expand the zenith-dependent intensity $I_\nu(p,\vartheta)$ into a series of Legendre polynomials and retain only the two leading terms. This allows for the necessary asymmetry between the upward and downward direction of the intensity:

$$I_\nu(p,\vartheta) = I_{0\,\nu}(p) + I_{1\,\nu}(p)\,\cos\vartheta\,. \tag{3.1}$$

The upward U_ν and downward D_ν monochromatic energy flux densities, defined as the directional integrals of the intensity over the upper and lower hemisphere, can then be calculated by means of the Eddington approximation. For the upward monochromatic energy flux density the integration over the upper hemisphere leads to

$$\begin{aligned} U_\nu(p) &= 2\pi \int_0^{\pi/2} I_\nu(p,\vartheta)\cos\vartheta\sin\vartheta d\vartheta \\ &= 2\pi \int_0^{\pi/2} \Big\{ I_{\nu,0}(p) + I_{\nu,1}(p)\cos\vartheta \Big\} \cos\vartheta\sin\vartheta d\vartheta \\ &= \pi I_{\nu,0}(p) + \frac{2}{3}\pi I_{\nu,1}(p). \end{aligned}$$

An analogous calculation holds for the downward monochromatic energy flux density. Hence we have

$$\begin{aligned} U_\nu(p) &= \pi I_{0\,\nu}(p) + \tfrac{2}{3}\pi I_{1\,\nu}(p) \\ D_\nu(p) &= \pi I_{0\,\nu}(p) - \tfrac{2}{3}\pi I_{1\,\nu}(p). \end{aligned} \tag{3.2}$$

Applying the Eddington approximation (3.1) and using the definition of the monochromatic radiative fluxes (3.2) to integrate the azimuth-independent plan parallel RTE (2.102) over the upper and lower domain yields Eddington-type transfer equations for the upward and downward monochromatic energy flux densities (to simplify the notation the pressure dependence of the radiative variables will be suppressed hereafter)

$$\begin{aligned} \frac{\partial}{\partial p} U_\nu &= \frac{7/4-\omega_\nu}{g}\,\kappa_\nu\,U_\nu + \frac{1/4-\omega_\nu}{g}\,\kappa_\nu\,D_\nu - \frac{2\,(1-\omega_\nu)}{g}\,\kappa_\nu\,B_\nu(T) \\ \frac{\partial}{\partial p} D_\nu &= -\frac{7/4-\omega_\nu}{g}\,\kappa_\nu\,D_\nu - \frac{1/4-\omega_\nu}{g}\,\kappa_\nu\,U_\nu + \frac{2\,(1-\omega_\nu)}{g}\,\kappa_\nu\,B_\nu(T). \end{aligned} \tag{3.3}$$

This system of coupled transfer equations for the upward and downward monochromatic energy flux densities forms the basis of the new simplified radiation scheme in the LW regime [1].

In principle, the coupled Eddington equations (3.3) must be solved for each absorption line contributing to the LW energy flux densities and heating rates (line-by-line calculation). To avoid such a time consuming procedure, averages over broad but nevertheless finite frequency bands corresponding to the main LW absorbers are defined. This substantially reduces the number of equations that must be solved to calculate the radiative heating rates. In the present setup a total of four broad frequency bands corresponding to the absorption by CO_2, ozone and water vapor is applied, see Table 3.1.

The frequency average of some quantity X_ν over a particular absorber band denoted by the index k is defined as

$$\overline{X}^{\,k} \doteq \frac{1}{\nu_{k2} - \nu_{k1}} \int_{\nu_{k1}}^{\nu_{k2}} X_\nu \, d\nu. \tag{3.4}$$

When X is U, D, or κ, in analogy to the Reynolds decomposition applied in turbulence theory, each variable X_ν can be written as the sum of the band mean value $\overline{X}^{\,k}$ and a perturbation part X'_ν.

$$X_\nu = \overline{X}^{\,k} + X'_\nu \tag{3.5}$$

As usual, the band averaged perturbations are assumed to vanish:

$$\overline{X'_\nu} = 0. \tag{3.6}$$

The frequency variations X'_ν contain fast variations associated with individual lines, as well as slow variations associated with different lines strengths and line distributions across each band. The frequency dependencies of the Planck function and the single scattering albedo, on the other hand, are assumed to be smooth such that

$$B_\nu \doteq \overline{B}^{\,k} + B^*_\nu \quad \text{and} \quad \omega_\nu \approx \overline{\omega}^{\,k} \quad \text{for} \quad \nu_{k1} < \nu < \nu_{k2}\,. \tag{3.7}$$

Here, B^*_ν describes the slow frequency-dependence of the Planck function within the band and satisfies $\overline{B^*_\nu} = 0$. No such frequency variation is retained for the single scattering albedo. $\overline{B}^{\,k}$ denotes the mean value of the Planck function $B_\nu(T)$ taken over the frequency range of band k which corresponds to the mean energy thermally emitted into this band:

$$\overline{B}^{\,k} \doteq \frac{1}{\nu_{k2} - \nu_{k1}} \int_{\nu_{k1}}^{\nu_{k2}} B_\nu(T) \, d\nu \tag{3.8}$$

To calculate the band mean Eddington equations, the decomposition (3.5) and (3.7) are

[1] Integration of these equations over the whole LW frequency range (broad band approximation applying one single absorption band) and setting $\omega_\nu = 1/4$ leads to a simple and decoupled system of equations [Held, 1982]. It has been applied in Held and Frierson [Frierson et al., 2006] and subsequent studies as a LW radiation scheme in mechanistic climate simulations [Frierson et al., 2007]. The resulting underestimation of emission and absorption due to the non-zero single scattering albedo is not important in view of the idealizations made otherwise in these studies.

inserted into the monochromatic transfer equations (3.3)

$$\begin{aligned}
\frac{\partial}{\partial p}\left(\overline{U}^{\,k}+U'_\nu\right) &= \frac{7/4-\overline{\omega}^{\,k}}{g}\left(\overline{\kappa}^{\,k}+\kappa'_\nu\right)\left(\overline{U}^{\,k}+U'_\nu\right) \\
&\quad+\frac{1/4-\overline{\omega}^{\,k}}{g}\left(\overline{\kappa}^{\,k}+\kappa'_\nu\right)\left(\overline{D}^{\,k}+D'_\nu\right) \\
&\quad-\frac{2\left(1-\overline{\omega}^{\,k}\right)}{g}\left(\overline{\kappa}^{\,k}+\kappa'_\nu\right)\left(\overline{B}^{\,k}+B^*_\nu\right) \\
\frac{\partial}{\partial p}\left(\overline{D}^{\,k}+D'_\nu\right) &= -\frac{7/4-\overline{\omega}^{\,k}}{g}\left(\overline{\kappa}^{\,k}+\kappa'_\nu\right)\left(\overline{D}^{\,k}+D'_\nu\right) \\
&\quad-\frac{1/4-\overline{\omega}^{\,k}}{g}\left(\overline{\kappa}^{\,k}+\kappa'_\nu\right)\left(\overline{U}^{\,k}+U'_\nu\right) \\
&\quad+\frac{2\left(1-\overline{\omega}^{\,k}\right)}{g}\left(\overline{\kappa}^{\,k}+\kappa'_\nu\right)\left(\overline{B}+B^*_\nu\right)^{k}.
\end{aligned}$$

Averaging these equations over the band k and bearing in mind that the band mean of the perturbations vanishes results in

$$\begin{aligned}
\frac{\partial}{\partial p}\,\overline{U}^{\,k} &= \frac{7/4-\overline{\omega}^{k}}{g}\left(\,\overline{\kappa}^{\,k}\,\overline{U}^{\,k}\;+\;\overline{\kappa'_\nu U'_\nu}\,\right)+\frac{1/4-\overline{\omega}^{\,k}}{g}\left(\,\overline{\kappa}^{\,k}\,\overline{D}^{\,k}\;+\;\overline{\kappa'_\nu\,D'_\nu}\,\right) \\
&\quad-\frac{2\left(1-\overline{\omega}^{\,k}\right)}{g}\left(\,\overline{\kappa}^{\,k}\,\overline{B}^{\,k}+\,\overline{\kappa'_\nu\,B^*_\nu}\,\right) \qquad (3.9)\\
\frac{\partial}{\partial p}\,\overline{D}^{\,k} &= -\frac{7/4-\overline{\omega}^{k}}{g}\left(\,\overline{\kappa}^{\,k}\,\overline{D}^{\,k}\;+\;\overline{\kappa'_\nu D'_\nu}\,\right)-\frac{1/4-\overline{\omega}^{\,k}}{g}\left(\,\overline{\kappa}^{\,k}\,\overline{U}^{\,k}\;+\;\overline{\kappa'_\nu U'_\nu}\,\right) \\
&\quad+\frac{2\left(1-\overline{\omega}^{\,k}\right)}{g}\left(\,\overline{\kappa}^{\,k}\,\overline{B}^{\,k}+\,\overline{\kappa'_\nu\,B^*_\nu}\,\right).
\end{aligned}$$

The covariance terms $\overline{\kappa'_\nu U'_\nu}$ and $\overline{\kappa'_\nu D'_\nu}$ appearing in (3.9) correspond to the well-known dependence of the flux transmission functions on deviations from the gray limit, cf. Ch.10.3 in the text of Thomas and Stamnes [2002]. An absorber band is defined to be "gray" if the frequency variations of the absorption coefficient within the band can be neglected. This is the case if the individual lines within the band are sufficiently broad. In the lower troposphere the assumption of the gray limit is often justified because of the strong pressure broadening of individual lines. However, due to the exponential decrease of the pressure with increasing height, the gray-limit assumption is no longer valid from the upper troposphere on. The resulting effects must be parameterized in any accurate radiative transfer scheme that invokes broad frequency bands. Accordingly, some assumption about the frequency variation of the absorption coefficient and the monochromatic energy flux densities inside each band k must be made. For the purpose to develop a simplified radiative transfer scheme it is adequate as a first guess to take advantage of the regular Elsasser band model (see [Thomas and Stamnes, 2002]). The Elsasser band model is usually applied to describe the frequency dependence of the extinction coefficient in terms of a shape function f_ν for the band considered, see Figure 3.1. It assumes an infinite number of equally spaced lines of equal shape. The lines of the Elsasser band are separated by the mean frequency interval δ^k and have the mean line width γ^k. The perturbation part of the frequency-dependent absorption coefficient can be written applying the Elsasser band model as

$$\kappa'_\nu=\overline{\kappa}^{\,k}\,\left(f_\nu(\delta^k,\gamma^k)-1\right)\quad\text{for}\quad\nu_{1\,k}\le\nu\le\nu_{2\,k}. \qquad (3.10)$$

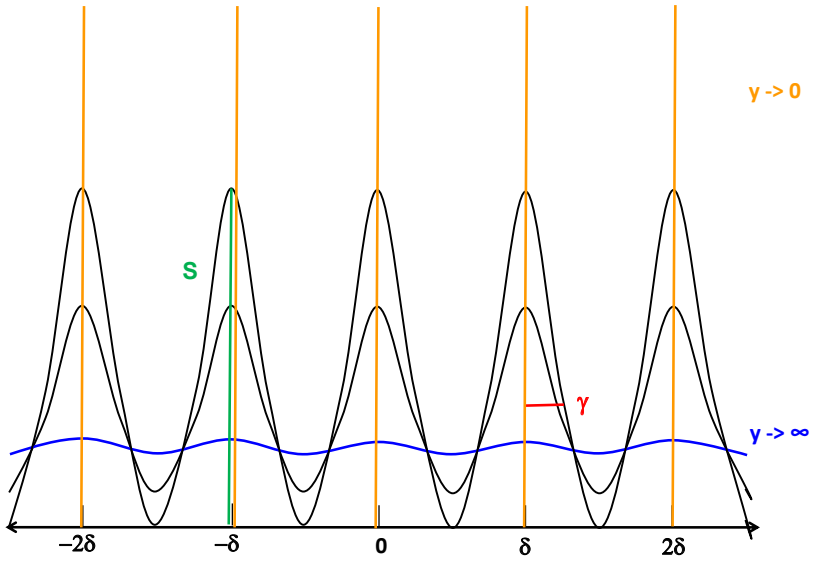

Figure 3.1: The Elsasser band consists of an infinite number of lines with line strength S and the Voigt line width γ. The lines are separated by the mean line spacing δ. The spectrum is given by the Elsasser shape function (3.11), which takes δ and γ as parameters. The limit of thin isolated lines is indicated in yellow and a spectrum close to the gray limit in blue.

The mean line profile describing the lines in the Elsasser band is given by the normalized Elsasser shape function [Thomas and Stamnes, 2002],

$$f_\nu(\delta^k, \gamma^k) \;=\; \frac{\sinh(2\pi y^k)}{\cosh(2\pi y^k) - \cos(2\pi\nu/\delta^k)} \tag{3.11}$$

with

$$\overline{f}^{\,k} = 1\,. \tag{3.12}$$

In (3.11) the grayness parameter y for band k is defined as the ratio of the mean line width to the mean line separation in the spectrum

$$y^k = \gamma^k/\delta^k\,. \tag{3.13}$$

The grayness parameter y^k measures the smoothness of the lines in band k by relating the mean line width γ^k to the mean line separation δ^k. For large values of the grayness parameter, the lines are broad and densely packed such that the extinction coefficient is blurred over the whole frequency range of the band, see the blue line in Figure 3.1. In this case, the frequency variance inside the band and therefore the covariance terms can be neglected (gray limit). The gray limit is approximately justified in the troposphere, where the Voigt line width is dominated by strong pressure broadening. Conversely, when the grayness parameter approaches values near zero, the Elsasser band is dominated by thin isolated lines. In this case, the absorption coefficient varies strongly with frequency inside the band. The covariance terms will then strongly affect the radiative transfer in the band. Above the troposphere, the line width quickly drops due to the exponential decrease of pressure with height. In

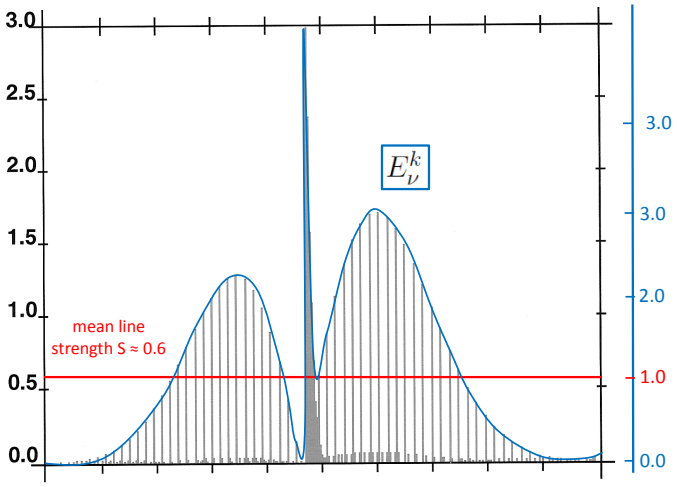

Figure 3.2: Sketch of a band spectrum and its corresponding envelope function E_ν^k (blue line). The line strength of the individual lines and the numerical values for the envelope function are given in arbitrary units. The band mean value of the envelope function is normalized to unity. For lines with a line strength corresponding to the mean value of the Elsasser band S (red) the envelope function takes a value of 1. Lines with line strengths smaller (greater) than the band mean value are scaled by a factor of E_ν^k smaller (greater) than one.

the middle atmosphere the line shape is solely determined by the much weaker Doppler and natural broadening, resulting in the lines to be very thin and isolated in each band. Neglecting the deviations from the gray limit above the tropopause would lead to a strong and unrealistic cooling of the middle atmosphere (see chapter 4).

To relax the idealization of the regular Elsasser band model a bit, an additional slowly-varying function E_ν^k to parameterize the frequency variation inside the band k due to the envelope function of the spectrum, see Figure (3.2), is included. This envelope function is assumed to be normalized such that its band mean value equals one

$$\overline{E}^{\,k} = 1\,. \tag{3.14}$$

The complete band shape function, can then be redefined as the product of the Elsasser shape function $f_\nu(\delta^k, \gamma^k)$ and the envelope function E_ν^k. Assuming the frequency variation of the envelope function to be sufficiently smooth, the band mean of the full band shape function can be approximated by

$$\frac{1}{\nu_{k2}-\nu_{k1}} \int_{\nu_{k1}}^{\nu_{k2}} f_\nu(\delta^k, \gamma^k)\; E_\nu^k \, d\nu \;\approx\; \frac{1}{\nu_{k2}-\nu_{k1}} \overline{E}^{\,k} \int_{\nu_{k1}}^{\nu_{k2}} f_\nu(\delta^k, \gamma^k)\, d\nu = \overline{f}^{\,k}\; \overline{E}^{\,k}. \tag{3.15}$$

Replacing the Elsasser shape function by the complete band shape function, the perturbation part of the extinction coefficient can be written as

$$\kappa'_\nu = \overline{\kappa}^k \; (f_\nu(\delta^k, \gamma^k) - 1)\; E_\nu^k \quad \text{for} \quad \nu_{1\,k} \le \nu \le \nu_{2\,k}. \tag{3.16}$$

To calculate the covariance terms involving U, D and κ in the mean Eddington equations (3.9), the frequency variation within a band k of the absorption coefficient and the upward and

downward energy flux densities must be known. Therefore it is assumed that the frequency dependence of the monochromatic energy flux densities inside a band k can be parameterized by the same functional dependence as is applied for the extinction coefficient. The perturbation part of the radiative energy flux densities can then be written in analogy to (3.16) as

$$\begin{aligned} U'_\nu &= \overline{u}^{\,k}\,(\,f_\nu(\delta^k,\gamma^k)-1\,)\,E^k_\nu \\ D'_\nu &= \overline{d}^{\,k}\,(\,f_\nu(\delta^k,\gamma^k)-1\,)\,E^k_\nu\,. \end{aligned} \tag{3.17}$$

Negative (positive) upward perturbation amplitudes $\overline{u}^{\,k}$ would describe the weakening (reinforcement) of the upward radiative energy flux densities by selective absorption (emission) on the line centers. The downward perturbation amplitudes $\overline{d}^{\,k}$ parameterize the enhancement of the downward radiative energy flux densities due to selective emission into the line centers.

The perturbation amplitudes can be found by deriving additional transfer equations from the monochromatic (3.3) and the band mean (3.9) equations. Therefore the extinction coefficient and the monochromatic energy flux densities are written as the sum of a band-mean value and the perturbation part

$$\begin{aligned} U_\nu &= \overline{U}^{\,k} + \overline{u}^{\,k}\,(\,f_\nu(\delta^k,\gamma^k)-1\,)\,E^k_\nu \\ D_\nu &= \overline{D}^{\,k} + \overline{d}^{\,k}\,(\,f_\nu(\delta^k,\gamma^k)-1\,)\,E^k_\nu \\ \kappa_\nu &= \overline{\kappa}^{\,k} + \overline{\kappa}^{\,k}\,(\,f_\nu(\delta^k,\gamma^k)-1\,)\,E^k_\nu\,. \end{aligned} \tag{3.18}$$

Then, the "Reynolds decomposition" of the radiative variables (3.18) is inserted into the monochromatic transfer equations (3.3). Subtracting the mean equations (3.9) a first intermediate result for the upward

$$\begin{aligned} \frac{\partial}{\partial p}\left\{\overline{u}^{\,k}(f-1)E^k_\nu\right\} &= \frac{7/4-\overline{\omega}^{\,k}}{g}\Bigg\{\overline{u}^{\,k}\overline{\kappa}^{k}(f-1)E^k_\nu + \overline{U}^{\,k}\overline{\kappa}^{k}(f-1)E^k_\nu \\ &\quad + \underbrace{\overline{u}^{\,k}\overline{\kappa}^{k}(f-1)^2(E^k_\nu)^2 - \overline{\kappa'_\nu\,U'_\nu}}_{\text{nonlinear terms}}\Bigg\} \\ &\quad + \frac{1/4-\overline{\omega}^{\,k}}{g}\Bigg\{\overline{d}^{\,k}\overline{\kappa}^{k}(f-1)E^k_\nu + \overline{D}^{\,k}\overline{\kappa}^{k}(f-1)E^k_\nu \\ &\quad + \underbrace{\overline{d}^{\,k}\overline{\kappa}^{k}(f-1)^2(E^k_\nu)^2 - \overline{\kappa'_\nu\,D'_\nu}}_{\text{nonlinear terms}}\Bigg\} \\ &\quad - \frac{2\,(1-\overline{\omega}^{\,k})}{g}\Bigg\{\overline{\kappa}^{\,k}\overline{B}^{\,k}(f-1)E^k_\nu\Bigg\}. \end{aligned} \tag{3.19}$$

and the downward perturbation amplitudes

$$\begin{aligned}\frac{\partial}{\partial p}\{\overline{d}^k(f-1)E_\nu^k\} &= -\frac{7/4-\overline{\omega}^k}{g}\Big\{\overline{d}^k\overline{\kappa}^k(f-1)E_\nu^k+\overline{D}^k\overline{\kappa}^k(f-1)E_\nu^k \\ &\quad+\underbrace{\overline{d}^k\overline{\kappa}^k(f-1)^2(E_\nu^k)^2-\overline{\kappa'_\nu\,D'_\nu}}_{\text{nonlinear terms}}\Big\} \\ &\quad-\frac{1/4-\overline{\omega}^k}{g}\Big\{\overline{u}^k\overline{\kappa}^k(f-1)E_\nu^k+\overline{U}^k\overline{\kappa}^k(f-1)E_\nu^k \\ &\quad+\underbrace{\overline{u}^k\overline{\kappa}^k(f-1)^2(E_\nu^k)^2-\overline{\kappa'_\nu\,U'_\nu}}_{\text{nonlinear terms}}\Big\} \\ &\quad+\frac{2\,(1-\overline{\omega}^k)}{g}\Big\{\overline{\kappa}^k\overline{B}^k(f-1)E_\nu^k\Big\}\end{aligned} \tag{3.20}$$

is obtained. Neglecting all of the nonlinear terms in (3.19) and (3.20), and dividing by $(\,f_\nu(\gamma^k,\delta^k)-1\,)\;E_\nu^k$, leads to the following transfer equation for the upward and downward perturbation amplitudes:

$$\begin{aligned}\frac{\partial}{\partial p}\,\overline{u}^k &= \frac{7/4-\overline{\omega}^k}{g}\,\overline{\kappa}^k\,(\,\overline{U}^k+\overline{u}^k)+\frac{1/4-\overline{\omega}^k}{g}\,\overline{\kappa}^k(\,\overline{D}^k+\overline{d}^k) \\ &\quad-\frac{2\,(1-\overline{\omega}^k)}{g}\,\overline{\kappa}^k\,\overline{B}^k \\ \frac{\partial}{\partial p}\,\overline{d}^k &= -\frac{7/4-\overline{\omega}^k}{g}\,\overline{\kappa}^k\,(\,\overline{D}^k+\overline{d}^k)-\frac{1/4-\overline{\omega}^k}{g}\,\overline{\kappa}^k\,(\,\overline{U}^k+\overline{u}^k\,) \\ &\quad+\frac{2\,(1-\overline{\omega}^k)}{g}\,\overline{\kappa}^k\,\overline{B}^k.\end{aligned} \tag{3.21}$$

Applying the Elsasser band model for the perturbation parts of the radiation variables, the covariance terms in the mean Eddington equations (3.9) can be reexpressed as

$$\begin{aligned}\overline{\kappa'_\nu\,U'_\nu} &= \overline{u}^k\overline{\kappa}^k\overline{(f-1)}^2(\overline{E_\nu^k})^2 \\ \overline{\kappa'_\nu\,D'_\nu} &= \overline{d}^k\overline{\kappa}^k\overline{(f-1)}^2(\overline{E_\nu^k})^2.\end{aligned} \tag{3.22}$$

Taking further the analytical expression

$$\overline{(f-1)^2}^k=\coth(2\pi y^k)-1 \tag{3.23}$$

into account finally leads to

$$\begin{aligned}\overline{\kappa'_\nu U'_\nu} &= \overline{\kappa}^k\,\overline{u}^k\,(\coth(2\pi y^k)-1)\,\overline{E^2}^k \\ \overline{\kappa'_\nu D'_\nu} &= \overline{\kappa}^k\,\overline{d}^k\,(\coth(2\pi y^k)-1)\,\overline{E^2}^k.\end{aligned} \tag{3.24}$$

The covariance terms involving the Planck function, $\overline{\kappa'_\nu\,B^*_\nu}$ occur in (3.9) due to the fact that individual lines may posses considerably different line strengths and may be unequally distributed, whereas the Planck function can be assumed to monotonically increase or decrease over a broad frequency band. The frequency-averaged thermal emissions will then be considerably less than $\overline{\kappa}^k\,\overline{B}^k$ for small grayness parameters. This effect is parameterized by

$$\overline{\kappa}^k\,\overline{B}^k+\overline{\kappa'_\nu\,B^*_\nu}\;=\;\Delta^k\,\overline{\kappa}^k\,\overline{B}^k \tag{3.25}$$

with $\Delta^k = 1$ in the gray limit and $0 < \Delta^k < 1$ otherwise. In other radiative transfer schemes, this effect is often taken into account by evaluating the Planck function at a particular frequency that corresponds to the strongest line of the band [Collins et al., 2004]. Nevertheless, to be consistent, any such parameterization should reduce to the band averaged Planck function in the gray limit. Equation (3.25) is consistent with this constraint by using

$$\Delta^k \;=\; 1 \;-\; \exp\big(\; 10\, y^k \;\ln(1 - b^k)\;\big)\,. \tag{3.26}$$

The b^k are tunable parameters that define the scaling of the Planck function for $y^k = 0.1$.

The system of equations so far consists of the frequency-averaged RTEs (3.9) combined with (3.24)-(3.26) and the RTEs for the perturbation amplitudes (3.21). To recover the radiative variables ($X = U, u, D, d, B$) in terms of energy flux densities they must be multiplied by the frequency range of the corresponding long-wave band

$$X^k = \overline{X}^k(\nu_{k2} - \nu_{k1}). \tag{3.27}$$

Looking at the mean (3.9) and perturbation equations (3.21) it can be seen that this unit conversion of the energetic variables does not change the form of the transfer equations.
In summary, the final Eddington-type RTEs in the LW regime are for the mean energy flux densities

$$\begin{aligned}
\frac{\partial}{\partial p} U^k &= \frac{7/4 - \overline{\omega}^k}{g}\,\overline{\kappa}^k\,(\,U^k \;+\; u^k\,(\coth(2\pi y^k) - 1)\,\overline{E^2}^k\,) \\
&+ \frac{1/4 - \overline{\omega}^k}{g}\,\overline{\kappa}^k\,(\,D^k \;+\; d^k\,(\coth(2\pi y^k) - 1)\,\overline{E^2}^k\,) \\
&- \frac{2\,(1 - \overline{\omega}^k)}{g}\,\overline{\kappa}^k\,\Delta^k B^k \\
\frac{\partial}{\partial p} D^k &= -\frac{7/4 - \overline{\omega}^k}{g}\,(\,D^k \;+\; d^k\,(\coth(2\pi y^k) - 1)\,\overline{E^2}^k\,) \\
&- \frac{1/4 - \overline{\omega}^k}{g}\,\overline{\kappa}^k\,(\,U^k \;+\; u^k\,(\coth(2\pi y^k) - 1)\,\overline{E^2}^k\,) \\
&+ \frac{2\,(1 - \overline{\omega}^k\,)}{g}\,\overline{\kappa}^k\,\Delta^k B^k
\end{aligned} \tag{3.28}$$

and for the perturbation amplitudes

$$\begin{aligned}
\frac{\partial}{\partial p} u^k &= \frac{7/4 - \overline{\omega}^k}{g}\,\overline{\kappa}^k\,(\,U^k + u^k\,) \;+\; \frac{1/4 - \overline{\omega}^k}{g}\,\overline{\kappa}^k\,(\,D^k \;+\; d^k\,) \\
&- \frac{2\,(1 - \overline{\omega}^k)}{g}\,\overline{\kappa}^k\,B^k \\
\frac{\partial}{\partial p} d^k &= -\frac{7/4 - \overline{\omega}^k}{g}\,\overline{\kappa}^k\,(\,D^k \;+\; d^k\,) \;-\; \frac{1/4 - \overline{\omega}^k}{g}\,\overline{\kappa}^k\,(\,U^k \;+\; u^k\,) \\
&+ \frac{2\,(1 - \overline{\omega}^k)}{g}\,\overline{\kappa}^k\,B^k\,.
\end{aligned} \tag{3.29}$$

This coupled system of transfer equations must be solved iteratively for the $4 * k$ unknowns U^k, D^k, u^k and d^k. At the top of the model atmosphere ($p = 0$), the downward long-wave energy flux density coming from space as well as the downward perturbation amplitudes are assumed to vanish:

$$D^k(\,p = 0\,) \;=\; d^k(\,p = 0\,) \;=\; 0. \tag{3.30}$$

	O3	H2O(1)	H2O(2)	CO2
Line Center	9.6 μm	6.3 μm	> 15 μm	15 μm
Transition	$\nu 1, \nu 2$	$\nu 2$	continuum	$\nu 2$
Number of lines	46422	6762	7244	18768
Min. wavenumber	980 cm^{-1}	1300 cm^{-1}	1 cm^{-1}	540 cm^{-1}
Max. wavenumber	1100 cm^{-1}	2100 cm^{-1}	540 cm^{-1}	800 cm^{-1}
$\overline{\epsilon}^k$	0.6	0.95	0.95	0.95
$\overline{E^2}^k$	1.5	1.5	1.0	1.5
b^k	0.250	0.600	0.975	0.080

Table 3.1: The broad long-wave frequency bands included in the simplified radiative-transfer scheme. They correspond to the most important bands of the primary absorbers accounting for the radiative heating and cooling rates in the middle atmosphere. The bands are further specified by the relevant transition mechanisms such as the molecular vibration number ν_i, combination band or rotation continuum. In the lowermost three rows the values of the free parameters of the radiation scheme are denoted for each band.

The surface ($p = p_s$) emits thermally according to its temperature T_s into the long-wave bands and directly to space. Therefore, the upward perturbation vanish at the surface. Our lower boundary conditions are

$$\begin{aligned} U^k(p = p_s) &= (1 - \overline{\epsilon}^k)\, D^k(p = p_s) + \overline{\epsilon}^k\, B^k(T_s) \\ u^k(p = p_s) &= 0\,. \end{aligned} \tag{3.31}$$

Here, a surface emissivity $\overline{\epsilon}^k$ is introduced for each band k and for the emission directly to space. The RTEs (3.28) and (3.29) are discretized using the terrain-following vertical hybrid coordinate system proposed by Simmons and Burridge [Simmons and Burridge, 1981]. This corresponds to a staggered vertical grid where the so-called half levels extend from $p = p_s$ to $p = 0$. The energy flux densities are calculated on these half levels, while the Planck function, the extinction coefficients and other band parameters, as well as the flux convergencies, i.e., the atmospheric LW radiative sensible heating rates in band k,

$$Q^k_{LW} = g\,\frac{\partial}{\partial p}\,(U^k - D^k)\,,\ k = 1, \ldots, 4, \tag{3.32}$$

are computed on the intermediate full model layers.

The free parameters of the so-defined LW radiation scheme are the surface emissivities $\overline{\epsilon}^k$, the band mean values of the squared envelope function $\overline{E^2}^k$, and the emission scaling factors b^k. The corresponding numbers applied for our four long-wave bands in the context of the test simulation are given in Table 3.1.

In the following subsection the calculation of the mean line widths, line distances, and extinction coefficients from the HITRAN data base [Rothman et al., 2004] is described. The definition of the non-LTE parameter $\overline{\omega}^k$ is given in section 3.3, which is followed by a description of our idealized transfer scheme in the short-wave regime.

3.2 Calculation of LW absorption coefficients

To calculate the LW heating rates as described in the previous section it is necessary to choose the most important absorbers and absorber bands. Aiming at middle atmospheric

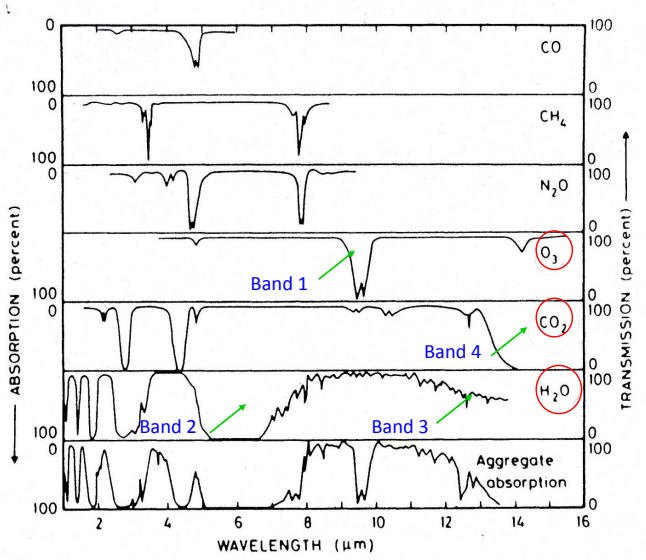

Figure 3.3: The four bands included to calculate the LW heating rates, based on Andrews' Figure 2.5 [Andrews et al., 1987]. The transmission (given in percent on the right axes in the figure) of energy through the atmosphere is reduced at those wavelengths where strong absorber bands are found (increased absorption). The absorbers selected are marked by red circles and the bands considered by green arrows.

applications four bands of the absorbers ozone, water vapor, and CO_2 are selected, based on Figure 2.5 of Andrews' text [Andrews et al., 1987], see Fig.(3.3) and Tab.(3.1). The approach to consider only CO_2, ozone, and water vapor as the most important LW absorbers is in agreement with other middle atmospheric radiation calculations [London, 1980; Fomichev et al., 1986].

Nevertheless, considering some climate indicators as for example the Radiative Forcing (RF) or the Global Warming Potential Index ($GWPi$) applied in the latest IPCC report to measure the contributions of different absorbers to climate change in the troposphere, additional trace gases such as CH_4, N_2O or CFCs are considered important in the troposphere [Forster et al., 2007]. The radiative forcing (Wm^{-2}) for an absorber i is defined as the change in the net radiative energy flux density (downward - upward) of SW plus LW radiation at the tropopause due to changes in the emission of the absorber since a reference time (usually 1750). The $GWPi$ is the time integrated radiative forcing of an absorber i induced by the pulse emission of 1 kg divided by the same quantity calculated for CO_2

$$GWP_i = \frac{\int_0^{TH} RF_i(t)dt}{\int_0^{TH} RF_{CO_2}(t)dt} \tag{3.33}$$

with

$$RF = aC(t). \tag{3.34}$$

Here $C(t)$ is the time dependent abundance of the absorber and a is the radiative efficiency, defined as the RF per unit mass increase. Due to the time horizon TH appearing in (3.33),

the $GWPi$ depends apart from the absorption properties and the time dependence of the absorber abundance on the life time of the absorber in the atmosphere.

Both the radiative forcing and the $GWPi$ are designed to compare the relative importance of different (radiative) climate forcings (as for example caused by changing emissions) for the troposphere. With regard to the application of the radiation scheme in a middle atmospheric mechanistic circulation model, the absolute radiative heating rates or temperature tendencies are of primary importance. Additional absorbers such as CH_4, N_2O or CFCs provide only minor contributions to these heating rates. Therefore it is sufficient to consider only CO_2, ozone and water vapor in the new LW radiation scheme.

The mean absorption coefficient $\overline{\kappa}^k$ for an absorber band is defined as the product of a mean band strength $\overline{K}^k$ (m^2kg^{-1}) and the absorber mass mixing ratio ρ_a^k/ρ (kg kg^{-1}).

$$\overline{\kappa}^k \;=\; \overline{K}^k \, \rho_a^k/\rho \tag{3.35}$$

In the present model setup the mass absorber mixing rations are prescribed, see Figure 3.4. The ozone mixing ratio (panel a) is similar to that used by Shine [Shine, 1987]. It is zonally symmetric and subject to a simple annual cycle. The tropospheric water vapor (panel b) maximizes in the intertropical convergence zone and in the middle latitudes. These maxima are subject to an annual cycle and have pronounced longitude-dependencies (not shown) that reflect the large-scale structure of tropospheric latent heating (see also section 4.1). Water vapor in the middle atmosphere (panel c), which in the real atmosphere results from methane oxidation [Grygalashvyly et al., 2009] and upward transport of water vapor through the tropical troposphere by the Brewer-Dobson circulation, is roughly taken into account by a zonally symmetric distribution subject to a seasonal cycle. The CO_2 mixing ratio (panel d) is constant up to the mesopause region and decreases in the lower thermosphere.

The mean band strengths $\overline{K}^k$ are derived from the HITRAN spectroscopic database (Rothman 2004) using a procedure similar to a line by line integration [Rothman et al., 2004]. The monochromatic absorption coefficient K_n, given in wave-number space k, can be written as the product of a temperature-dependent line strength $S_n(T)$ and a normalized shape function $f_n(\mathrm{k}, T, p)$, where the index n enumerates the lines of the band considered,

$$K_n = S_n(T) f_n(\mathrm{k}, T, p) \tag{3.36}$$

with

$$\int_{-\infty}^{\infty} f_n(\mathrm{k}, T, p) dk = 1. \tag{3.37}$$

By integrating the shape function f_n for each line n over the whole wave-number space to encompass the complete absorptance, the monochromatic absorption coefficient can be reduced to the temperature dependent line strength S_n, see Eq.(A11) of Rothman 1998 [Rothman et al., 1998],

$$S_n(T) = S_n(T_{ref}) \frac{Q(T_{ref}) \exp(-c_2 E_n/T)}{Q(T) \exp(-c_2 E_n/T_{ref})} \frac{[1 - \exp(-c_2 \mathrm{k}_n/T)]}{[1 - \exp(-c_2 \mathrm{k}_n/T_{ref})]} \tag{3.38}$$

which contains the temperature dependent partition function

$$Q(T) = \sum_s g_s \exp(-c_2 E_n/T_{ref}). \tag{3.39}$$

E_n and k_n denote the lower energy level and the transition wave-number, $c_2 = hc/k_B$ is the second radiation constant, g_s the statistical weight of the lower energy level. A reference temperature of $T_{ref} = 296$ K is applied.

(a)

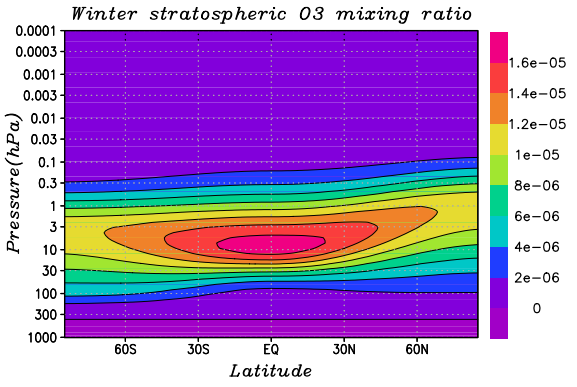

(b)

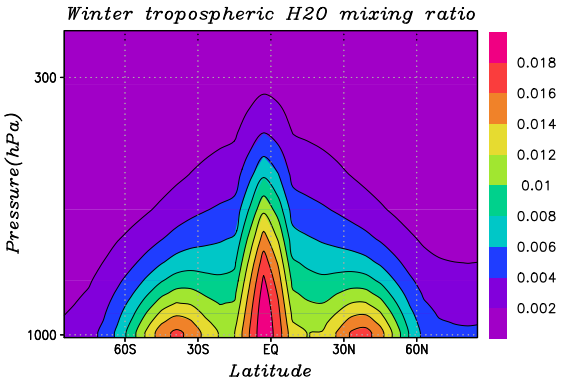

(c)

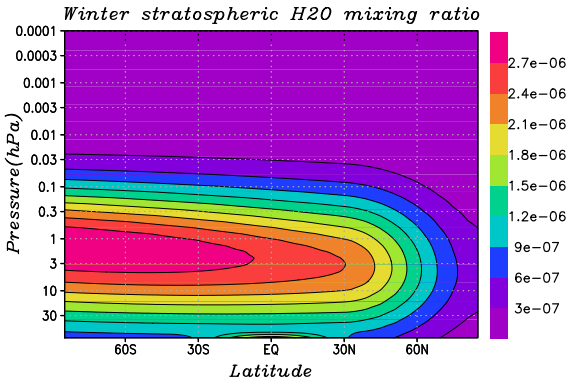

(d)

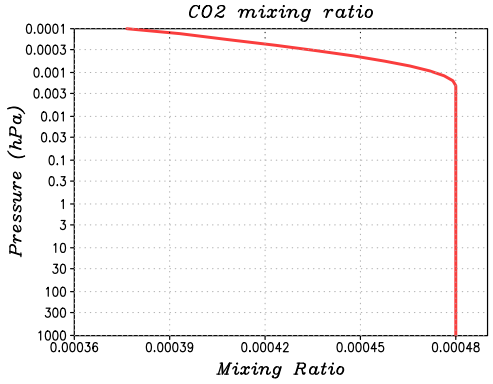

Figure 3.4: Prescribed mass-mixing ratios of (a) ozone (January), (b) tropospheric water vapor, (c) water vapor in the middle atmosphere (January), and (d) carbon dioxide.

band	a	b	c	d
1	$5.293 \cdot 10^{-7}$	-0.0008959	0.6251	41.64
2	1.3	0.5982	5.729	-
3	7.012	0.5457	19.78	-
4	93.4	-0.01006	39.93	0.0002842

Table 3.2: Parameters of the curves (3.42) used to parameterize the temperature dependence of the for LW band strengths.

Hence, the mean band strength can be written as a sum over all N^k line strengths divided by the frequency range of the band

$$\overline{K}^k = \frac{F}{(\nu_{k2} - \nu_{k1})} \sum_{n=1}^{N^k} S_n(T). \tag{3.40}$$

The factor F is applied to convert the band strengths from HITRAN units of cm^2/molecule to the units of a mass absorption coefficient m^2/kg applied in the mechanistic model

$$F = \frac{10^{-4}}{\langle M \rangle}. \tag{3.41}$$

Here, $\langle M \rangle$ is the mean mass of an absorber molecule in kg, considering all isotopes weighted with their relative frequencies.

For the calculation of the mean band strengths as described above, the line parameters for the four LW bands from the HITRAN 2004 database are applied [Rothman et al., 2004]. To enhance the computational efficiency, the temperature dependencies of the band strengths can accurately be fitted to the following empirical expressions:

$$\begin{aligned} \overline{K}^k(T) &= a \cdot T^3 + b \cdot T^2 + c \cdot T + d && \text{for ozone } (k = 1), \\ \overline{K}^k(T) &= a \cdot T^b + c && \text{for water vapor } (k = 2, 3), \\ \text{and} \quad \overline{K}^k(T) &= a \cdot \exp(b \cdot T) + c \cdot \exp(d \cdot T) && \text{for carbon dioxide } (k = 4). \end{aligned} \tag{3.42}$$

The so-obtained temperature dependencies of the band strengths for ozone 9.6 μm, $(k = 1)$, water vapor 6.3 μm, $(k = 2)$, and CO_2 (15 μm, $k = 4$) are displayed in Figure 3.5, and the fitting parameters for all four bands are listed in Table 3.2. Note that for water vapor and ozone, the band strength increases monotonically with temperature, whereas CO_2 shows the opposite behavior [Gerakines et al., 1995; Oeberg et al., 2007].

To compute the mean Voigt line width $\gamma^k(p, T)$ needed to evaluate the grayness parameter appearing in the Elsasser band model, the convolution of the Lorentz line width $\gamma_L(p, T)$ and the Doppler line width $\gamma_D(T)$ is approximated according to Olivero and Lomgbothum (1977, their Eq.(4c)[Olivero and Longbothum, 1977])

$$\gamma^k(p, T) = 1.0692 \cdot \gamma_L(p, T) + \sqrt{0.8664 \cdot \gamma_L(p, T)^2 + 2.7726 \cdot \gamma_D(T)^2} \tag{3.43}$$

with

$$\gamma_L(p, T) = \left(\frac{T_{ref}}{T}\right)^{\mathrm{n}} (\gamma_{air}(p_{ref}, T_{ref})(p - p_a) + \gamma_{self}(p_{ref}, T_{ref}) \cdot p_a) \tag{3.44}$$

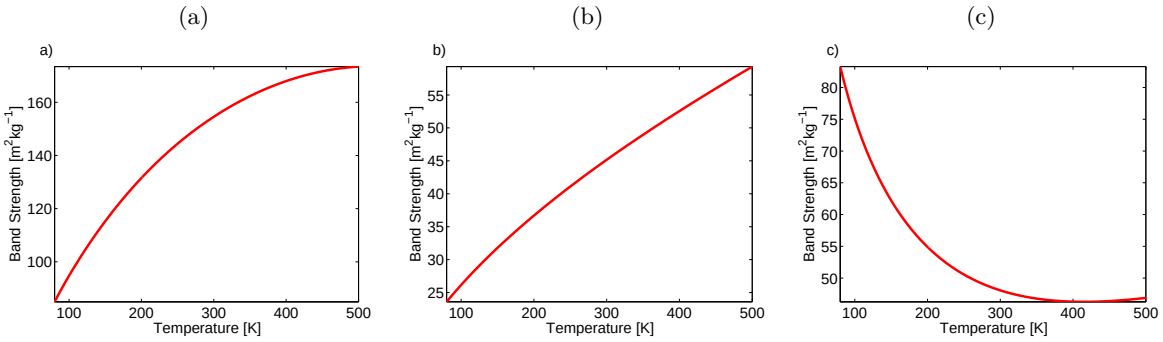

Figure 3.5: Temperature dependencies of the mean band strengths (m^2kg^{-1}). (a) Ozone band strengths ($k = 2$). (b) Water vapor ($k = 4$). (c) Carbon dioxide ($k = 6$).

and

$$\gamma_D(T) = \nu_0 \left(\frac{2k_B T}{mc^2} \right)^{1/2} . \tag{3.45}$$

The Lorentz line width comprises both the pressure broadening induced by collisions with air molecules (half line width γ_{air}) and the self broadening effect due to the finite life-time of the upper energy level of the transition considered (half width γ_{self}) [Rothman et al., 1998]. The Doppler line width accounts for the effect of the thermal motion of the absorber molecules on the line shape. In (3.44)-(3.45), T_{ref} is again 296 K, p_{ref} is 1 bar, p_a is the partial pressure of the absorber, m is the mass of an absorber molecule (kg) and ν_0 is the band center (Hz). Parameters such as the air and self broadening line widths and the exponent n are again taken from HITRAN [Rothman et al., 2004] for each line and band mean values are calculated for each LW frequency band applied in the new radiation scheme.
Olivero's s formula leads to a maximum error relative to the real Voigt line of about 2% [Olivero and Longbothum, 1977].

3.3 Non-LTE parameterisation

Due to the exponential decrease of air density with height, inelastic collisions between the atmospheric constituents become less frequent. As a consequence for some vibrational/rotational transitions of the radiatively active molecules, the ratios of the population numbers of the respective energy levels may no longer be described by the Boltzmann distribution. In this case the LTE assumption (as applied in the radiative transfer literature, compare Chapter 2.2.3) breaks down and the source function is no longer given by Planck's law. This non-LTE situation must be accounted for in the RTE to correctly simulate the thermodynamic state of the middle atmosphere with a GCM. Calculating for example the heating rate in the CO_2 15 μm band assuming LTE would lead to a strong excessive cooling of the middle atmosphere. Retaining only the cooling to space term in the Curtis matrix formulation results in a cooling rate of about 100 Kd^{-1}. Furthermore, the scale-selective radiative damping of waves depends strongly on the application of a suitable non-LTE parameterization in the middle atmosphere [Fels, 1984; Andrews et al., 1987].

A lot of non-LTE radiative transfer parameterizations have already been proposed by other authors. As discussed in the Appendix B, for only weak deviations from LTE of the radiation field a macroscopic statistical approach that is based on an extended ensemble formalism [Vasconcellos et al., 2005] can be applied to derive anisotropic nonequilibrium emission functions in terms of corrections to the Planck function [Fort et al., 1998]. To allow for states

farther away from LTE, as encountered in the middle atmosphere and the thermosphere, Dickinson used a three level model to calculate non-LTE source functions [Dickinson, 1984]. Zhu applied Curtis matrix calculations with prescribed temperature distributions to obtain long-wave radiative cooling rates [Zhu and Strobel, 1991; Zhu, 1993]. Kutepov calculated the radiation field under non-LTE conditions by iterating between the integrated RTE and the statistical equilibrium equations for the population numbers of the energy levels considered [Kutepov et al., 1998], see Chapter 2.3.

In order to incorporate the strong deviations from LTE in the formalism presented here, the final transfer equations are solved for finite values of the single scattering albedo $\overline{\omega}^k$. The increasing importance of isotropic scattering with height describes the reduced efficiency of absorption and emission. The single scattering albedo in turn is derived from the two-level model described in Chapter 2.2.3. For use in the radiation scheme, the band-mean value of $\omega_\nu = 1 - \varepsilon_\nu$ for each absorber band k is needed. It is defined as

$$\overline{\omega}^k \doteq 1 - \frac{\overline{C}^k_{21}}{\overline{C}^k_{21} + \overline{A}^k_{21}(1 - \exp(-\frac{h\nu^k_0}{k_B T}))^{-1}}\,, \tag{3.46}$$

applying the band-mean values of the Einstein coefficients for spontaneous emission $\overline{A}^k_{21}$ (calculated from HITRAN 2004), and the band mean inelastic collision rates $\overline{C}^k_{21}$. Here ν^k_0 is the central frequency of band k. The mean inelastic collision rates $\overline{C}^k_{21}$ are defined as the product of a mean inelastic collision coefficient $\overline{k}^k_{21}$ and the amount of third body molecules $[M]$ [Thomas and Stamnes, 2002]. Assuming a sufficient number of elastic collisions between the atmospheric constituents to maintain the law of detailed balance (LTE of the atmospheric constituents, compare the discussion of Figure 2.2), the collision coefficient $\overline{k}^k_{21}$ can be replaced by the more easily determined quenching coefficient $\overline{k}^k_{12}$. Hence the mean inelastic collision rate for each band $\overline{C}^k_{21}$ can be written as

$$\overline{C}^k_{21} = \overline{k}^k_{21}\,[M] = \overline{k}^k_{12}\,\frac{\overline{g}^k_1}{\overline{g}^k_2}\exp\left(\frac{h\nu^k_0}{k_B T}\right)[M] \tag{3.47}$$

with

$$\overline{k}^k_{12} = a^k \left(\frac{T}{300}\right)^{1/2} \exp\left(-\frac{h\nu^k_0}{k_B T}\right). \tag{3.48}$$

The statistical weights of the lower and upper states of a monochromatic transition g_1 and g_2 are given line by line in HITRAN [Simeckova et al., 2006]. The parameters a^k contain the mean inelastic collision scattering cross sections, which are not well known for such broad absorber bands as used in the present radiation scheme. Therefore the a^k are used as tuning parameters to control the efficiency of the inelastic collisions. The third body molecules are generally assumed to be N_2 and O_2, such that $[M]$ can be approximated by the air density. For the CO_2 15μ m band, collisions with molecular oxygen become important above the mesopause. For this band $a^4 = 100$ is used for the collisions with air molecules and $a^4 = 0.3 \cdot 10^3$ for the much more efficient collisions with atomic oxygen. The molecular oxygen mixing ratio applied in the test simulation is given in Figure 3.6.

The weighting of thermal emission $(1 - \overline{\omega}^k)$ and isotropic scattering $(\overline{\omega}^k)$ in the source function depends on the ratio of the time constant for spontaneous emission and the time constant for quenching by inelastic collision $\Phi \doteq \frac{C_{21}}{A_{21}}$. Conventionally the transition level from LTE to non-LTE (the so-called vibrational relaxation level) in the atmosphere is defined as

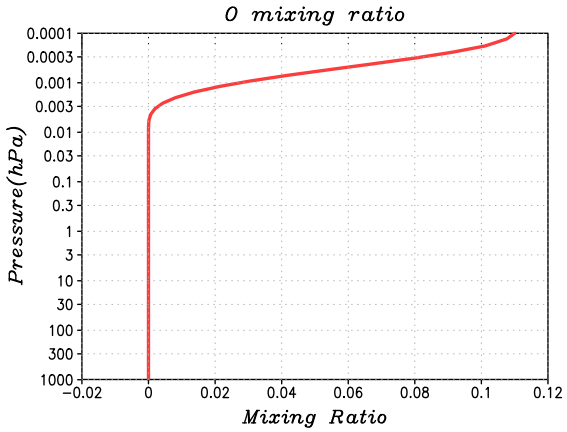

Figure 3.6: Atomic oxygen mass mixing ratio. This presribed profile is applied to calculate the collision rate in the CO_2 15μ m band.

the height where this ratio equals one meaning that the two processes are of equal importance

$$\Phi = \frac{C_{21}}{A_{21}} = 1. \tag{3.49}$$

Inserting (3.49) into the definition of the band mean single scattering albedo (3.46) results in a mean single scattering albedo of $\overline{\omega}^k = 0.5$ which therefore corresponds to the vibration relaxation level as defined above. For the CO_2 15μm band, the height of the vibration relaxation level is estimated to be at about 75 km [Andrews et al., 1987]. Looking at the latitude-height distribution of the single scattering albedo for each of the four long-wave bands applied here, the corresponding height of transition from LTE to non-LTE in the new LW radiation scheme can easily be determined, see Chapter 4.5.

Knowing the single scattering albedo, the non-LTE source function can be calculated for each long-wave absorber band applying the relations between the mean intensity and the long-wave energy flux densities (3.2). In the context of the Eddington equations the non-LTE source function is then given by

$$\overline{S}^k = (1 - \overline{\omega}^k)B^k(T) + \overline{\omega}^k \left(\overline{U}^k + \overline{D}^k + \text{covariance terms}\right). \tag{3.50}$$

The scattering contribution of the covariance terms to the source function can be shown to be negligible. To describe the deviation of the source function from Planck's law, the relative non-LTE source functions can be defined as

$$\overline{S}^k_{rel} \doteq \frac{\overline{S}^k}{B^k(T)}. \tag{3.51}$$

These relative source functions can be compared to the results of other authors [Dickinson, 1984] and will be further discussed in Chapter 4.3.

3.4 Short-wave radiation

The short-wave absorbers considered in the model are stratospheric ozone, water vapor in the troposphere and in the middle atmosphere, and molecular oxygen in the lower thermosphere. In the clear air calculations applied here, scattering and reflection of solar radiation, apart from an adaptation of the surface albedo to include the effect of reflection by clouds, are neglected.

At the top of the atmosphere, the incoming solar energy is subdivided into four broad UV and visible bands. The rest of the solar energy is transmitted without loss to the surface. With $\cos\theta_0(\lambda, \phi, t)$ being the cosine of the solar zenith angle depending on longitude λ, latitude ϕ, and time t, see [Hartmann, 1994], the upper boundary conditions for the short-wave energy flux densities are defined as

$$\begin{aligned} S^1(p=0) &= C_{sun}\ UV_{O3}\ \cos\theta_0 \\ S^2(p=0) &= C_{sun}\ VIS_{O3}\ \cos\theta_0 \\ S^3(p=0) &= C_{sun}\ VIS_{H2O}\ \cos\theta_0 \\ S^4(p=0) &= C_{sun}\ UV_{O2}\ \cos\theta_0 \\ S^5 &= C_{sun}\ \cos\theta_0\ - \sum_{i=1}^{4} S^i(p=0) \end{aligned} \tag{3.52}$$

C_{sun} is the solar constant and the symbols $UV_{O3}, VIS_{O3}, VIS_{H2O}, UV_{O2}$ denote the relative parts of solar energy contained in each band. The following values are used in the test simulation described in Chapter 4.1: $UV_{O3} = 0.015$, $VIS_{O3} = 0.07$, $VIS_{H2O} = 0.165$, and $UV_{O2} = 0.33 \cdot 10^{-5}$.

Retaining only the absorption term on the right hand side of the plan parallel equation (2.102) and assuming that the short wave radiation propagates only downward through the atmosphere along the zenith direction θ_0, leads to Beer-Bougert-Lambert s law for the short-wave radiative transfer:

$$\cos\theta_0 \frac{\partial}{\partial p} S^i = -\frac{\kappa^i}{g} S^i \tag{3.53}$$

for $i = 1, \ldots, 4$. With regard to ozone, the solar radiation is subdivided into an UV band S^1, representing the Hartley-Huggins band, and a visible band S^2 to parameterize the Chappuis band [London, 1980]. The other two short-wave energy flux densities S^3 and S^4 are subject to absorption by water vapor and molecular oxygen. S^5 is independent of height and represents the solar insolation reaching the surface without loss.

The short-wave absorption coefficients κ^i are defined in analogy to the specification applied for the long-wave regime as the product of the absorber mixing ratio ρ_a/ρ times the band strengths K^i,

$$\kappa^i = \frac{\rho_a}{\rho} K^i \,. \tag{3.54}$$

The mass volume mixing ratios used for O_3 and H_2O are shown in Figure 3.4. For the very simple thermospheric solar heating rate due to absorption by molecular oxygen, a constant oxygen concentration is used. The short wave band strengths $K^i = (2200; 0.15; 650; 58)$, given in units of $\mathrm{m}^2\ \mathrm{kg}^{-1}$, are tuning parameters to adjust the short-wave heating rates given by

$$Q^i_{SW} \ = \ - g \, \frac{\partial}{\partial p} \, S^{\,i} \,, i = 1, \ldots, 4 \,. \tag{3.55}$$

Note that the simple thermospheric solar heating Q^4_{SW} is a strong simplification of the complicated process of the dissociation of molecular oxygen and the subsequent recombination of atomic oxygen and chemical heating due to other processes, which usually take place in the mesopause region [Fomichev et al., 2002]. These processes are mimicked by redistributing some of the heating due to absorption by molecular oxygen from the lower thermosphere down to the summer mesopause region. Note that the correct representation of chemical heating is not in the focus of this study. Furthermore, previous mechanistic model studies

have shown that a reasonable thermal and dynamical structure of the mesopause region as well as insightful dynamical responses can well be simulated using the mechanistic model concept [Becker and von Savigny, 2010; Hoffmann et al., 2010].

Chapter 4

Results

In this chapter a short description of the mechanistic circulation model used to test the new radiation scheme is given. This is followed by a discussion of the climatological state and annual variation of the model atmosphere when applying the new radiation scheme (Section 4.2). Some specific results illustrating the performance of the radiation calculation are discussed in section 4.3. The energy balance at the top of the atmosphere (TOA) and at the surface are then compared to the findings of other modeling and measurement studies in section 4.4. The sensitivity of the radiative heating rates to the appropriate consideration of deviations from the gray limit and from LTE is investigated in chapter 4.5. Finally in Chapter 4.6 the annual variation of the TOA radiative energy balance and the radiative effect of doubling the CO_2 amount on the summer MLT are evaluated and interpreted.

4.1 Model overview

The radiation scheme described in the previous section is validated using the Kühlungsborn Mechanistic general Circulation Model (KMCM). The dynamical core of this model is standard and solves the primitive equations by the spectral transform method applied on so-called hybrid surfaces [Simmons and Burridge, 1981]. The present resolution is triangular spectral truncation at wavenumber 32 and 70 levels from the surface up to 4×10^{-5} hPa ($\sim$120 km height). Up to the lower thermosphere this resolution is similar to those usually used in middle atmosphere GCMs [Fomichev et al., 2002; Schmidt et al., 2006]. In addition to the radiation scheme, the model includes parameterizations for gravity waves and turbulence. In particular, the complete surface energy budget is taken into account. The model specifications are discussed in the following.

Vertical momentum and heat diffusion is based on the mixing-length concept and scaled by the Richardson criterion as usual. These terms include the dissipation due to momentum diffusion according to the energy conservation law [Becker, 2003a, b]. Also horizontal diffusion is formulated with respect to the conservation laws [Becker and Burkhardt, 2007]. These parameterizations ensure that the kinetic energy destroyed by momentum diffusion is precisely balanced by a positive definite dissipation rate, see (2.58). This internal heating equals the net diabatic heating of the atmosphere [Lorenz, 1964]. Note that the neglect of dissipation would lead to a systematic artificial radiative forcing that corresponds to the intensity of the Lorenz energy cycle [Becker, 2003a, b].

The latent heating is subject to simple parameterizations since an explicit tropospheric moisture cycle is not included in the KMCM yet. The latent heating Q_c is prescribed in the intertropical convergence zone and a self-induced condensational heating which is pro-

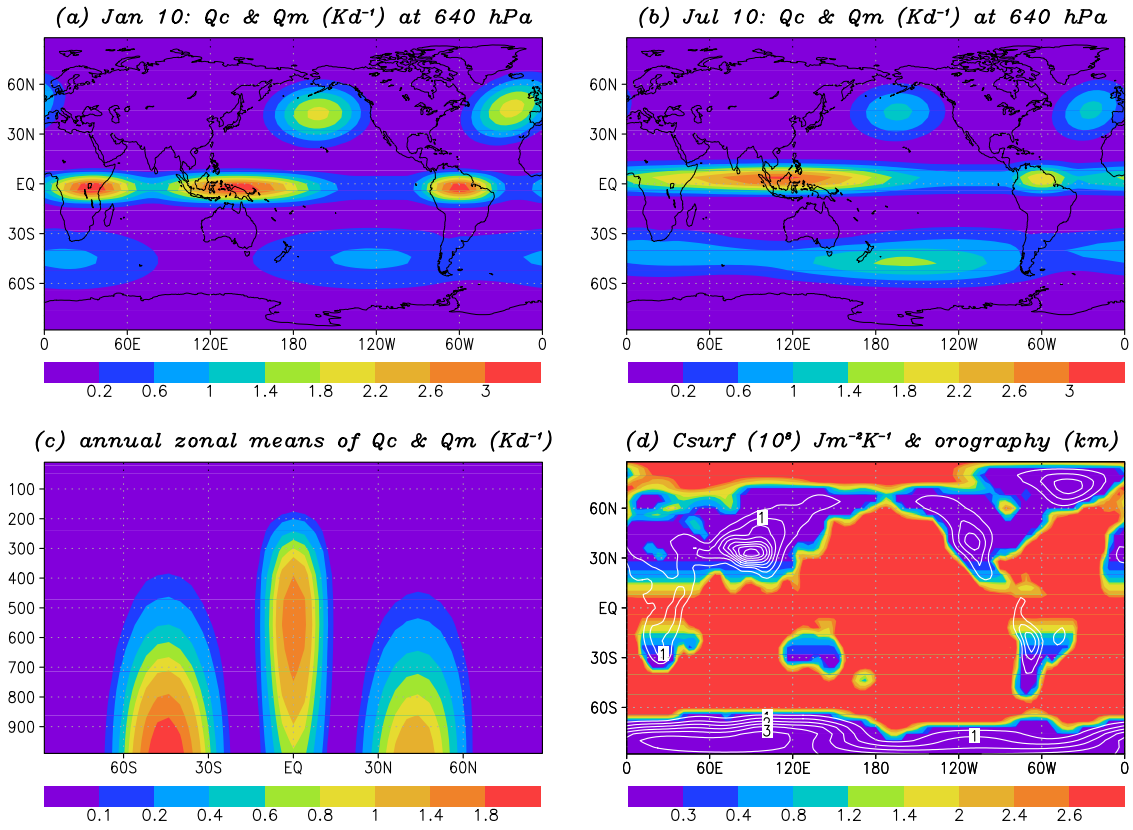

Figure 4.1: Latent heating functions, orography and surface heat capacity. Longitude-latitude distribution of the latent heating functions (Kd^{-1}) for (a) January 10., (b) July 10., (c) latitude-hight cross-section of the annual zonal mean latent heating function (Kd^{-1}) and (d) contours of the model orography (contour interval 0.5 km) and surface heat capacity (colors, 10^8 Km^{-2})

portional to the heating function Q_m is assumed in the middle latitudes. The latent heating can be written as

$$Q_{lat} = Q_c + \mathrm{He}(-\dot{p})\,\frac{\dot{p}}{\dot{p}_0}\,Q_m\,. \tag{4.1}$$

Here, $\dot{p}$ denotes pressure velocity and $\dot{p}_0 = 90$ Pa/s. The Heaviside function He ensures that latent heating in middle latitudes is only present in regions of ascending motion such as to reinforce low-pressure systems. This method has successfully been used in previous studies (e.g., [Körnich et al., 2006]). The heating functions for January and July are given in Figure 4.1 panel a and b. An annual cycle is realized by combining the January and July fields with harmonic functions with respect to the day of the year. Panel c displays the annual mean of the zonal-mean heating functions in a latitude-height cross-section.

Concerning the LW effects of clouds, a constant upper tropospheric zonally symmetric cooling rate of 1 Kd^{-1} together with a corresponding contribution to the upward radiative energy flux is included to represent the cloud LW radiative cooling. The cloud greenhouse effect is not yet accounted for.

For the sake of a consistent radiation budget at the surface and at the top of the atmosphere

(TOA), the surface energy budget is specified as follows:

$$c_{surf}\,\partial_t T_s \;=\; (1-\alpha)\sum_{i=1}^{5} S^i(p_s) \;+\; \sum_{k=1}^{4}(D^k(p_s)-U^k(p_s)) \;-\; U^5 \qquad (4.2)$$
$$-\;\int_0^{p_s} Q_{lat}\,\frac{dp}{g} \;-\; \rho_L\,c_D\;c_p\,|\vec{v}_L|\,(\Theta_s-\Theta_L) \;+\; q_{surf}\,.$$

Here c_{surf} is the surface heat capacity. Land-sea contrasts are represented by assigning different values of c_{surf} for water (3.0×10^8 JK^{-1}m^{-2}) and land surfaces (0.30×10^8 JK^{-1}m^{-2}). Figure 4.1d shows the model orography by contours (with a maximum elevation of the Himalayas of 4.9 km) together with c_{csurf} given by color shading. The surface albedo is 0.38 at the equator and increases to 0.47 at the poles. The somewhat larger values for the albedo compared to other models and measurements [Trenberth et al., 2009] represent the effect of reflection of SW radiation by clouds which is otherwise not accounted for in the model. In addition to the surface absorption of solar radiation proportional to $(1-\alpha)$, (4.3) also takes the long-wave energy flux densities into account. Here, $U^5 = \sigma\,T_s^4 - (U^1(p_s)+U^2(p_s)+U^3(p_s)+U^4(p_s))$ is the long-wave energy flux density that is directly radiated back into space. The energy flux corresponding to the upward cloud LW cooling is added to this band from the mid-troposphere on. The surface budget (4.3) furthermore includes the losses of energy due to latent heating and sensible heating in each column. While the former must be specified as an integral in our model formulation, the latter can be written in terms of the flux boundary condition for the vertical diffusion of sensible heat. Here, the index L indicates the lowest full model layer, c_D is the usual surface exchange coefficient, and $\vec{v}$ the horizontal wind. The potential temperature is defined as $\Theta = T\,(p/p_{00})^{R/c_p}$ with $p_{00} = 1013$ hPa and Θ_s is the surface potential temperature. Finally, some prescribed surface heating q_{surf} is included in order to maintain the surface temperatures in the regions of maximum Q_c and Q_m. The global mean of q_{surf} is zero to ensure energy conservation.

To adequately simulate the general circulation in the middle atmosphere, with the present low-resolution model version, the effects of internal gravity waves must be parameterized. Here, the extended Doppler-spread parameterization (DSP) for non-orographic gravity waves which has recently been proposed by Becker and McLandres [2009] is used. This version of the DSP deviates from previous implementations (e.g., [Fomichev et al., 2002]) by the representation of all energy conversions, as well as by a dynamically consistent treatment of vertical diffusion. In addition, a simple orographic gravity wave drag parameterization is included to improve the simulation of the stratospheric polar vortex.

4.2 Climatology and annual cycle

In this section the zonal-mean model climatology and the simulated annual cycle are inspected in order to validate the performance of the radiation scheme in the context of the large-scale atmospheric dynamics. The model was integrated for several years until the surface temperature reached a steady annual mean state for the chosen model parameters. Then another 5 years were simulated which form the basis of the analysis presented here.

Figure 4.2 shows monthly zonal means of the temperature, the zonal wind, and the residual mass streamfunction for January and July. All the main features of the general circulation are well captured. In the troposphere, the temperature decreases toward the poles and vertically up to the tropopause, with a tropical cold point of about 190 K around 100 hPa. In the stratosphere, the temperature increases with height and towards the summer pole.

The wave-induced winter stratopause is too warm and too high . An explanation for this deficiency is not at hand yet, but it may be caused by the lack of a realistic orographic gravity-wave drag parameterization. The meridional temperature gradient is reversed in the mesopause region due to the gravity-wave driven summer-to-winter-pole branch of the residual circulation, compare the Appendix A. According to an approximate gradient wind balance, the mean zonal wind also exhibits the main features of the general circulation. This includes the westerly jets in the troposphere, as well as westerlies versus easterlies in the middle atmosphere in winter versus summer up to the mesopause region where the wind reverses. This wind reversal is most pronounced in summer, as observed. The residual mass streamfunction exhibits the-well known two-cell structure, with the winter cell extending more and more into the summer hemisphere with increasing height above the tropopause, featuring upwelling in the summer polar mesosphere and downwelling in the winter mesosphere and stratosphere. In addition, the specification of land-sea heating contrasts and the resulting forcing of planetary Rossby waves induces the expected north-south asymmetry, with the polar night jet in the middle atmosphere being clearly stronger in the southern than in the northern hemisphere. All these simulated features compare well to results obtained with comprehensive middle atmospheric GCMs [McLandress et al., 2006; Fomichev et al., 2007], given the mechanistic character of the model used here. The only exception is the temperature structure around the polar winter stratopause as already mentioned.

Figure 4.3 displays the annual variations for the zonal mean temperature and the zonal mean zonal wind at 70 N and at 70 S in terms of consecutive 5-day averages. The simulation reproduces the observed annual variations in a satisfactory way. In particular, the summer mesopause shifts downward during the summer season, [Gerding et al., 2008] and the summer easterlies are most prevailing in the upper mesosphere, [Hoffmann et al., 2010]. For the present parameter setting the northern winter stratosphere exhibits minor stratospheric warming events but no major warming. The differences in the variability of temperature and the zonal wind between the southern and the northern hemisphere can again be explained by the stronger and more stable polar vortex in the southern hemisphere.

In Figure 4.4, the zonal and annual mean diabatic heating rates of the troposphere and lower stratosphere (panel a) are compared to the dynamic heating rates (adiabatic heating plus advection, panel b). As expected for climatological equilibrium, the heating rates due to diabatic processes are exactly compensated everywhere by the resolved dynamic heating. The spatial distribution of the diabatic or dynamic heating indicates that the Lorenz energy cycle is reasonably well simulated (see the discussion in the indroduction). In panel (c) and (d) of Figure 4.4 the January mean heat budget is shown, compare also Figure 6 in [Becker, 2011]. The most important feature in panel (c) is the vertical dipole due to the sum of radiative heating, diffusion and dissipation, and parameterized GW heating, featuring a cooling in the lower thermosphere and a heating in the mesopause region. These heating rates are compensated by a reverse dipole in the large-scale dynamic heating in polar summer, panel (d), with cooling around and below the mesopause and heating above. This reflects the residual circulation with upwelling in the mesosphere and downwelling in the lower thermosphere (the thermospheric contours of the streamfunction are not included in Figure 4.2 panel (b)). In the winter lower mesosphere the residual circulation gives rise to the dynamically induced stratopause which induces a compensating radiative cooling, see panel (c).

4.3 Radiation quantities

To evaluate the overall consistency of the radiation scheme, we diagnose the radiative energy balance at the top of the atmosphere (TOA), as well as the global and annual mean SW

(a) (b)

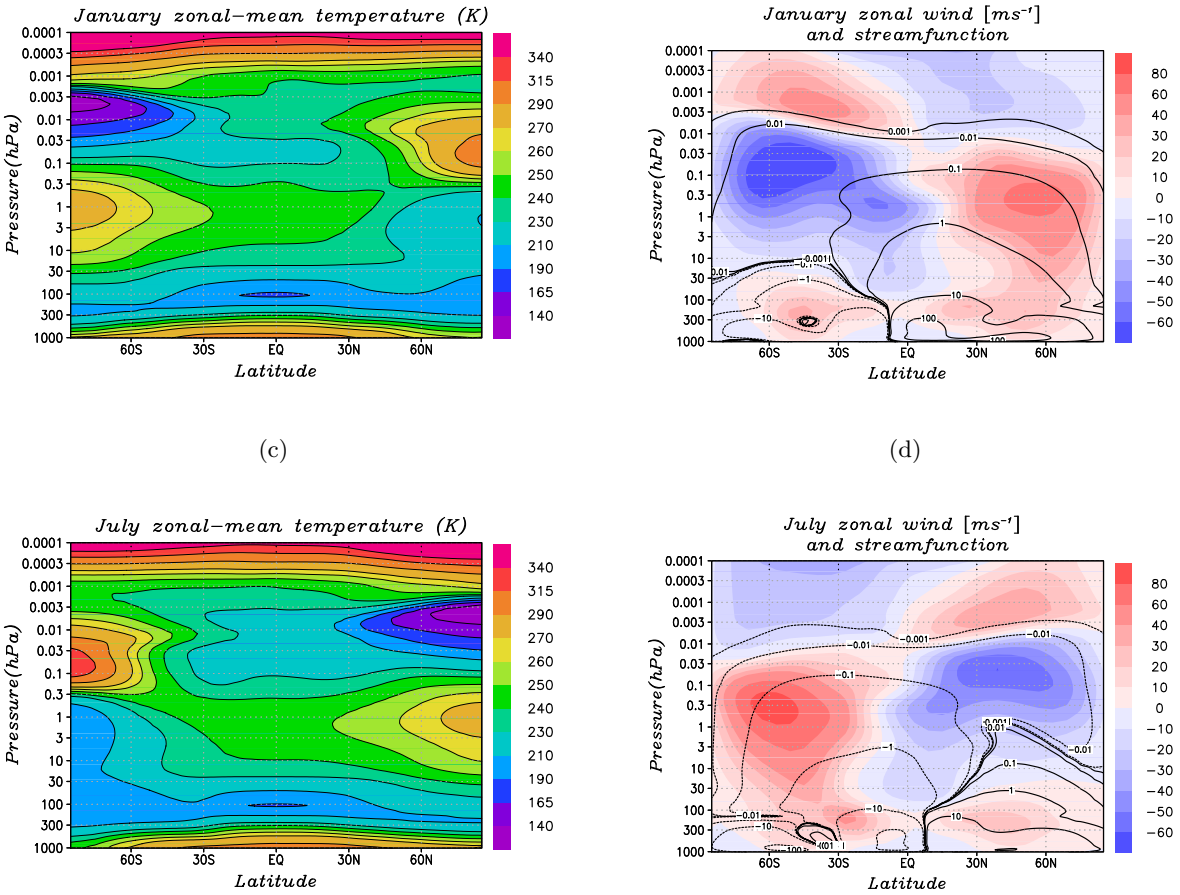

(c) (d)

Figure 4.2: January and July climatologies from five years of integration. (a) January temperature (K), (b) January zonal wind (ms^{-1}) and contours of the residual mass stream-function (10^9 kgs^{-1}), (c) July temperature (K), and (d) July zonal wind (ms^{-1}) and contours of the residual mass stream-function (10^9 kgs^{-1}).

(a) (b)

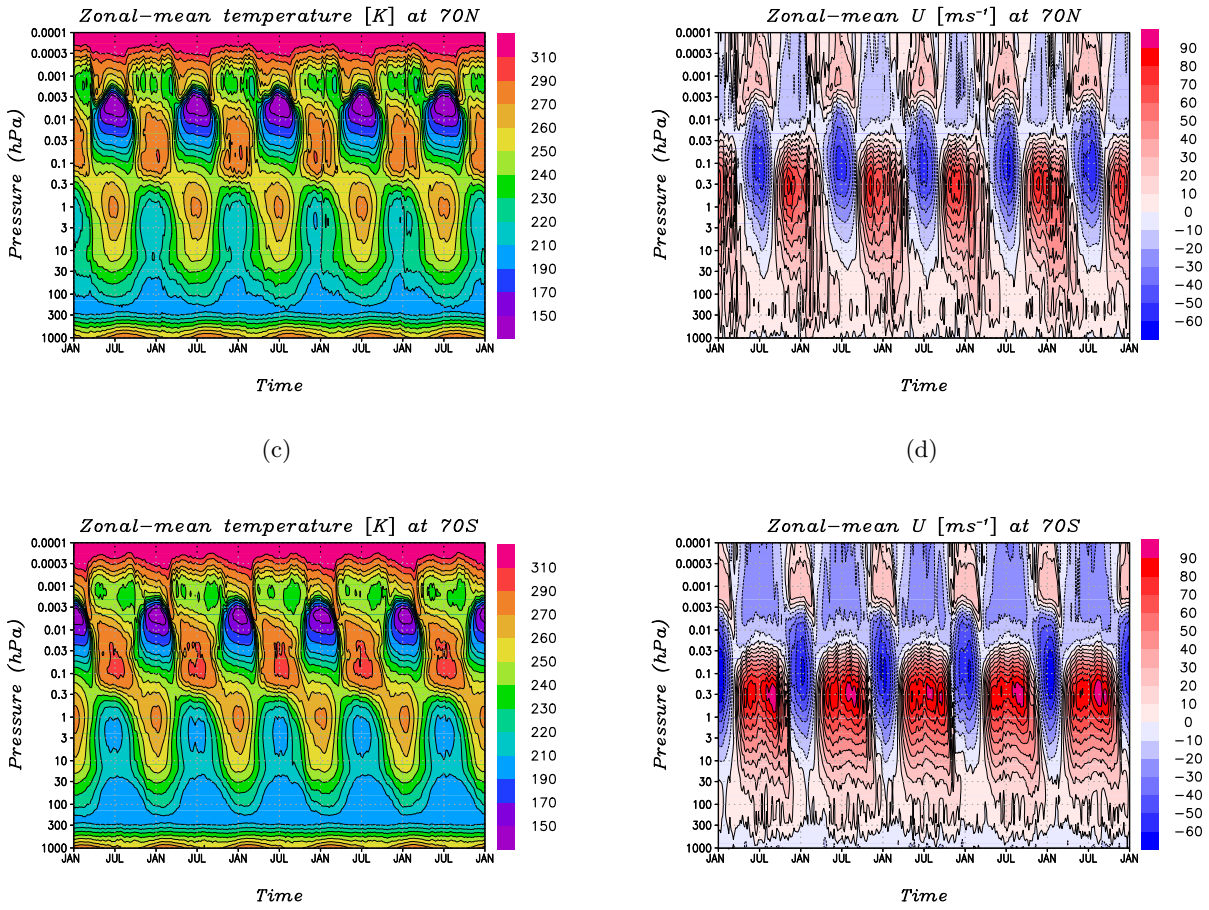

(c) (d)

Figure 4.3: Time series of five-day zonal-mean averages at 70 N of (a) the zonal-mean temperature (K) and (b) the zonal-mean zonal wind (ms^{-1}) and at 70 S of (c) the zonal-mean temperature (K) and (d) the zonal-mean zonal wind (ms^{-1}).

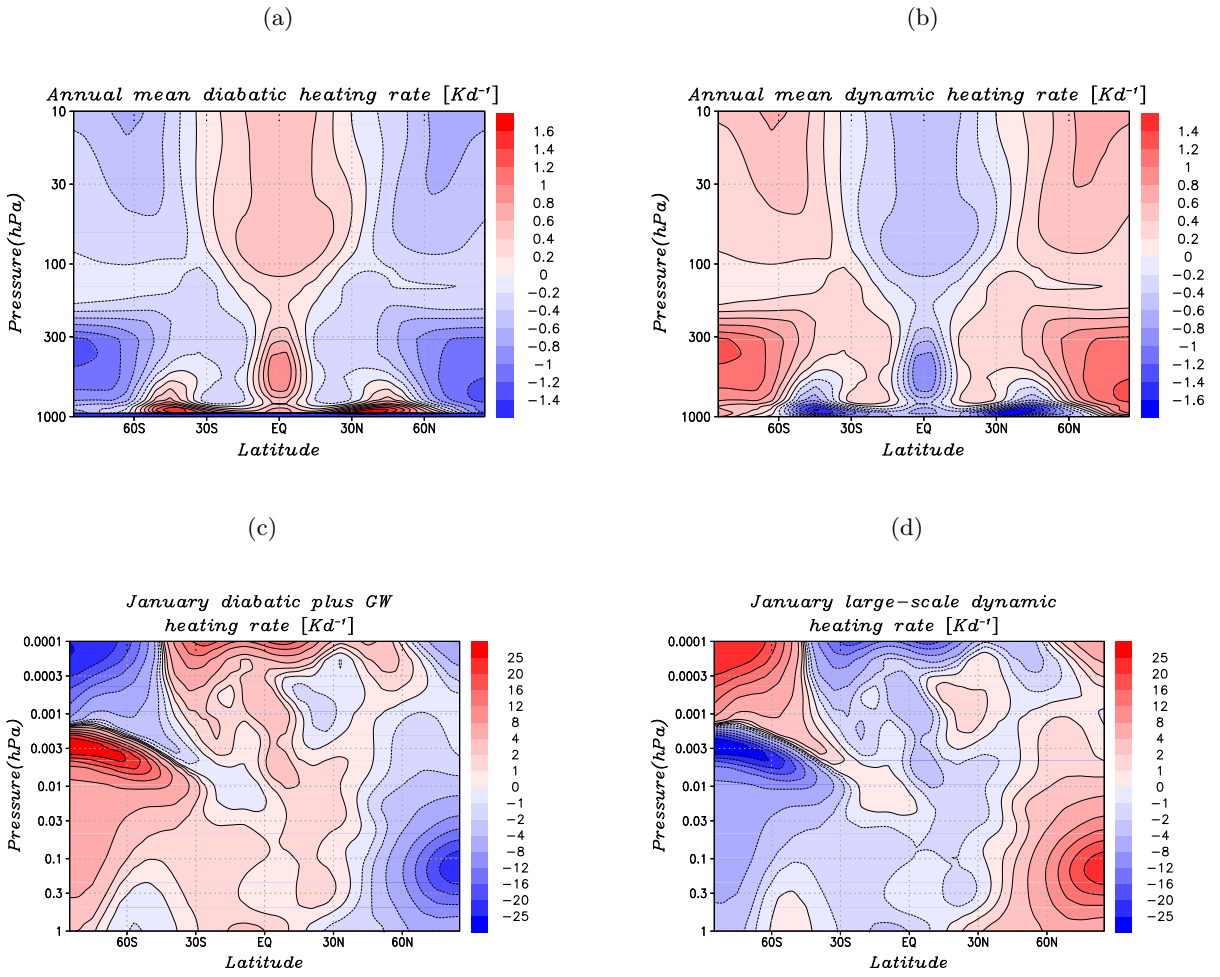

Figure 4.4: (a),(b): Five year average of the annual mean diabatic and the annual mean dynamic heating rates for the troposphere and lower stratosphere. (c), (d): January mean (five months) diabatic plus GW heating rates, and the large-scale dynamic heating for the middle atmosphere. The unit is Kd^{-1}.

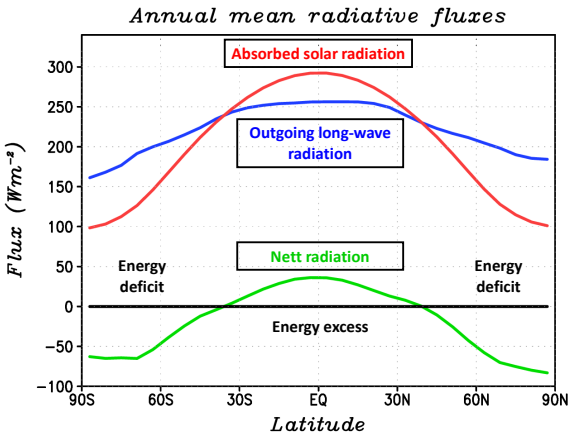

Figure 4.5: Radiative energy budget at the top of the atmosphere (Wm^{-2}). blue: outgoing longwave radiation, red: absorbed solar radiation, green: net radiation

heating and LW cooling rate profiles. The annual mean radiative energy fluxes at the TOA are given in Figure 4.5. The absorbed solar radiation (hereafter: ASR) is defined as the incoming solar radiation at the TOA minus the solar radiation that is reflected back to space due to the latitude-dependent planetary albedo. The latitude distribution of the ASR shows a maximum at the equator and decreases towards polar latitudes. In our model with prescribed cooling due to clouds, the outgoing LW radiation (hereafter: OLR) is the upward radiative energy flux at the TOA in the four absorber bands plus the LW radiation emitted from the surface and by clouds. The OLR shows a weaker dependence on latitude than the absorbed solar radiation. The resulting imbalance (ASR-OLR) corresponds to a surplus of radiative energy at the equator and a deficit poleward of about 35 latitude. These imbalances are somewhat weaker than observed (see the text of Hartmann 1994, his Figure 2.12) because the surface energy budget does not properly include the heat exchange between low and high latitudes by ocean currents.

In the climatological mean, the polar energy deficits and the equatorial energy excess must generally add up to zero if the climate is in equilibrium (zero radiative forcing). This constraint holds with an error of about 0.23 Wm^{-2} in the model presented here. This means, that all energy conversion rates, including for example the dissipation of kinetic energy generated via the Lorenz energy cycle, the energetics of parameterized gravity waves, or the radiative, latent, and sensible heat exchange with the surface, are represented without systematic errors. The global average of the outgoing long-wave radiation is about 235 Wm^{-2} which is somewhat less than the observational estimate of 242 Wm^{-2}. Note however that the model is not tuned to yield this value, but rather to reproduce the general circulation up to the mesopause region.

The global and annual mean LW cooling and SW heating rates are displayed in Figure 4.7. These results may be compared to the compilation of cooling and heating rates from different models presented by London [London, 1980], see Figure 4.6. The solar heating rates are determined by UV absorption in the thermosphere by oxygen and in the stratopause region by ozone. Absorption of visible radiation by water vapor leads to an additional heating maximum in the troposphere. In the middle atmosphere, carbon dioxide is the most important greenhouse gas. It leads to strong cooling rates around the stratopause and in the mesosphere/lower thermosphere (MLT). Ozone induces a cooling rate of a few Kd^{-1} around the stratopause and a small long-wave heating rate in the lower stratosphere due to absorption of upward radiation. Water vapor cools predominantly the tropopause region and the lower

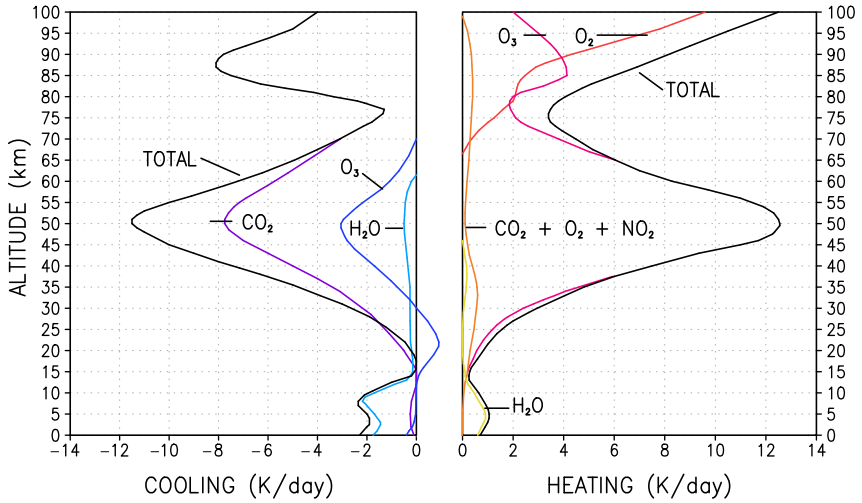

Figure 4.6: Contributions to the global-mean radiative heating and cooling rates from 0 -100 km (Kd^{-1}) based on Figure 2 in [London, 1980].

stratosphere.

Considering the global and annual means of the downward LW radiative fluxes due to water vapor and carbon dioxide in the troposphere (Figure 4.8) confirms that water vapor leads to a stronger greenhouse effect, i.e., 165 versus 100 W m^{-2}. Note that the sum of these two numbers encompasses not the entire downward long-wave radiation in the troposphere [Hartmann, 1994; Trenberth et al., 2009] due to the neglect of the cloud greenhouse effect in the present model version [Held and Soden, 2000]. In the middle atmosphere, the almost height-independent global and annual mean upward radiative fluxes (not shown) result in energy losses to space of 75.7 Wm^{-2} in the water vapor bands, 6.2 Wm^{-2} in the CO_2 band, and 11.6 Wm^{-2} in the ozone band. The surface emits another 96.6 Wm^{-2} not subject to radiative transfer within the model atmosphere, while the prescribed cloud cooling corresponds to an additional emission of 45.3 Wm^{-2}. The sum of these numbers corresponds to the global mean OLR, compare Figure 4.5 and Table 4.1.

Figures 4.9 and 4.10 show latitude-height cross-sections of the January mean upward and downward long-wave energy flux densities for the ozone 9.6 μm band, the water vapor 6.3 μm band, the water vapor rotation continuum, and the CO_2 15 μm band. In the stratosphere, the strongest absorption of upward radiation is seen for the ozone band (panel a), whereas the upward energy fluxes in the water vapor and CO_2 bandss (panel b-d) are weakened mainly in the troposphere. Carbon dioxide absorbs upward radiation up to the lower stratosphere. Regarding the downward fluxes in Figure 4.10, it can again be seen that the water vapor rotational continuum (panel c) leads to the strongest greenhouse effect. For the water vapor bands the downward radiation mainly originates in the troposphere, whereas for ozone and CO_2, the downward emission is already relevant in the stratosphere. This behavior of the upward and downward energy flux densities is consistent with the fact that the long-wave radiation measured by satellites to retrieve temperature and absorber profiles originates in the tropopause/lower stratosphere region for CO_2 and ozone, and in the troposphere for water vapor (see text of Liou, [Liou, 2002]).

We now consider the effects of deviations from the gray limit. Recall that these deviations are treated in our LW radiation scheme by solving the additional transfer equations for the

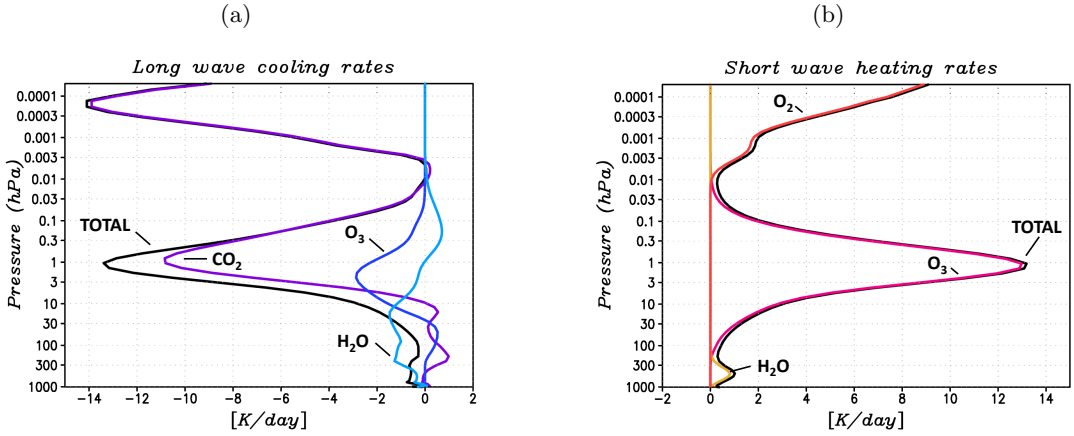

Figure 4.7: Global and annual mean heating and cooling rate profiles. (a) the net short-wave heating rate (black) due to oxygen in the lower thermosphere (red), ozone in the stratosphere (magenta), and water vapor in the troposphere (yellow). (b) the total long-wave cooling rate (black) due to ozone (blue), carbon dioxide (dark purple), and water vapor (medium blue). The unit is Kd^{-1}.

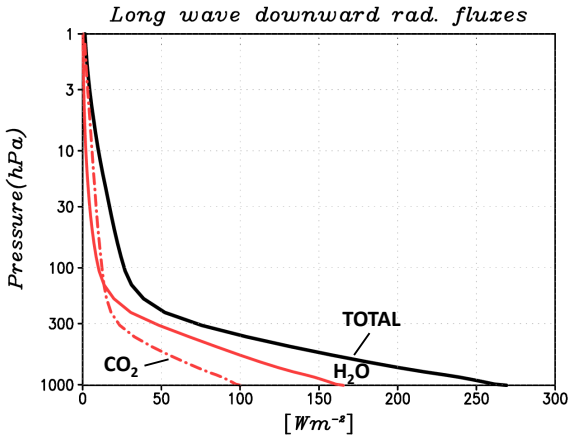

Figure 4.8: Global and annual mean downward long-wave energy flux densities due to water vapor (red solid) and carbon dioxide (red dashed-dotted), as well as the total long-wave energy flux density (black solid). The unit is Wm^{-2}.

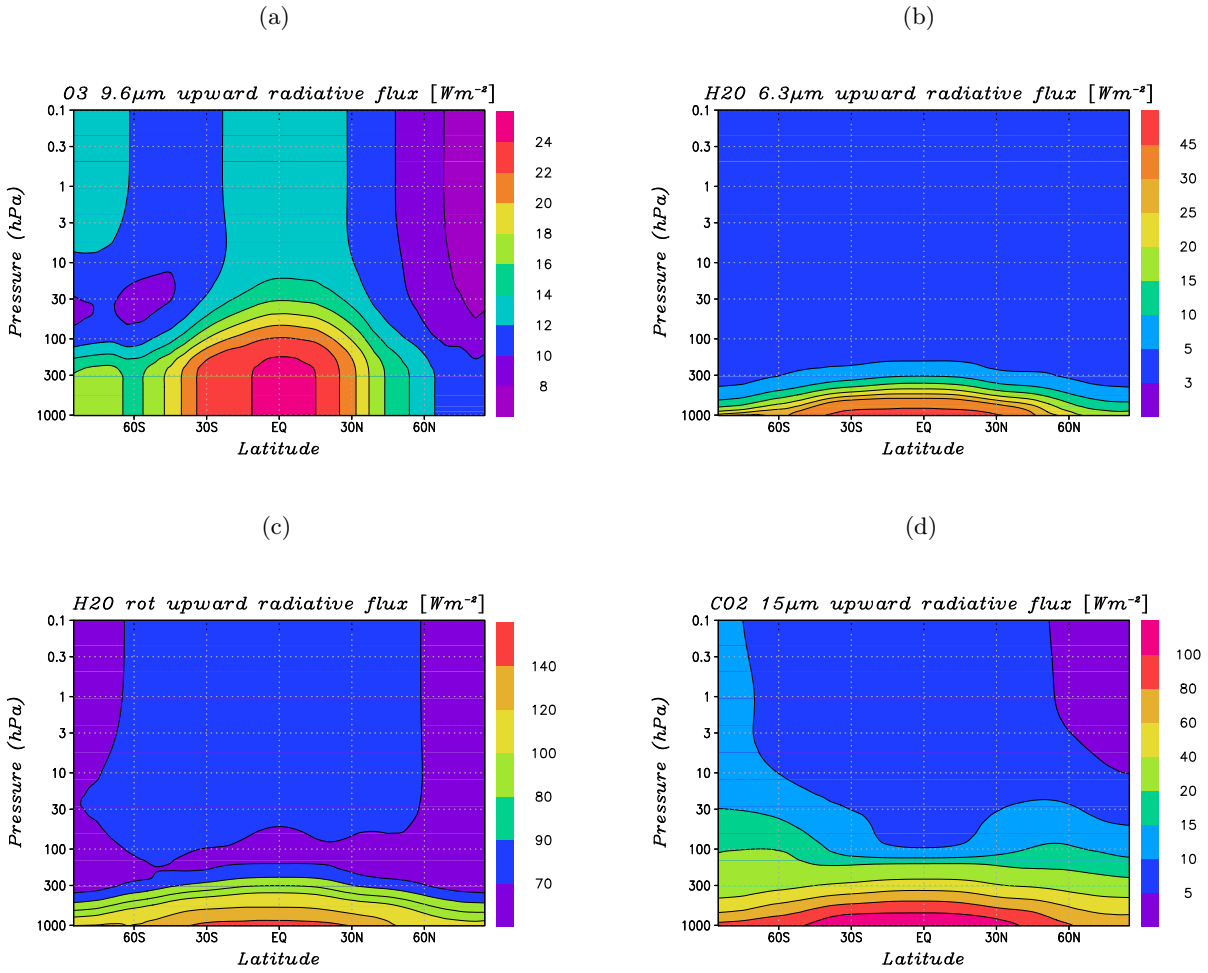

Figure 4.9: January mean upward radiative fluxes (Wm^{-2}) for (a) the ozone 9.6 μm band, (b) the water vapor 6.3 μm band, (c) the water vapor rotation continuum, and (d) the CO_2 15 μm band.

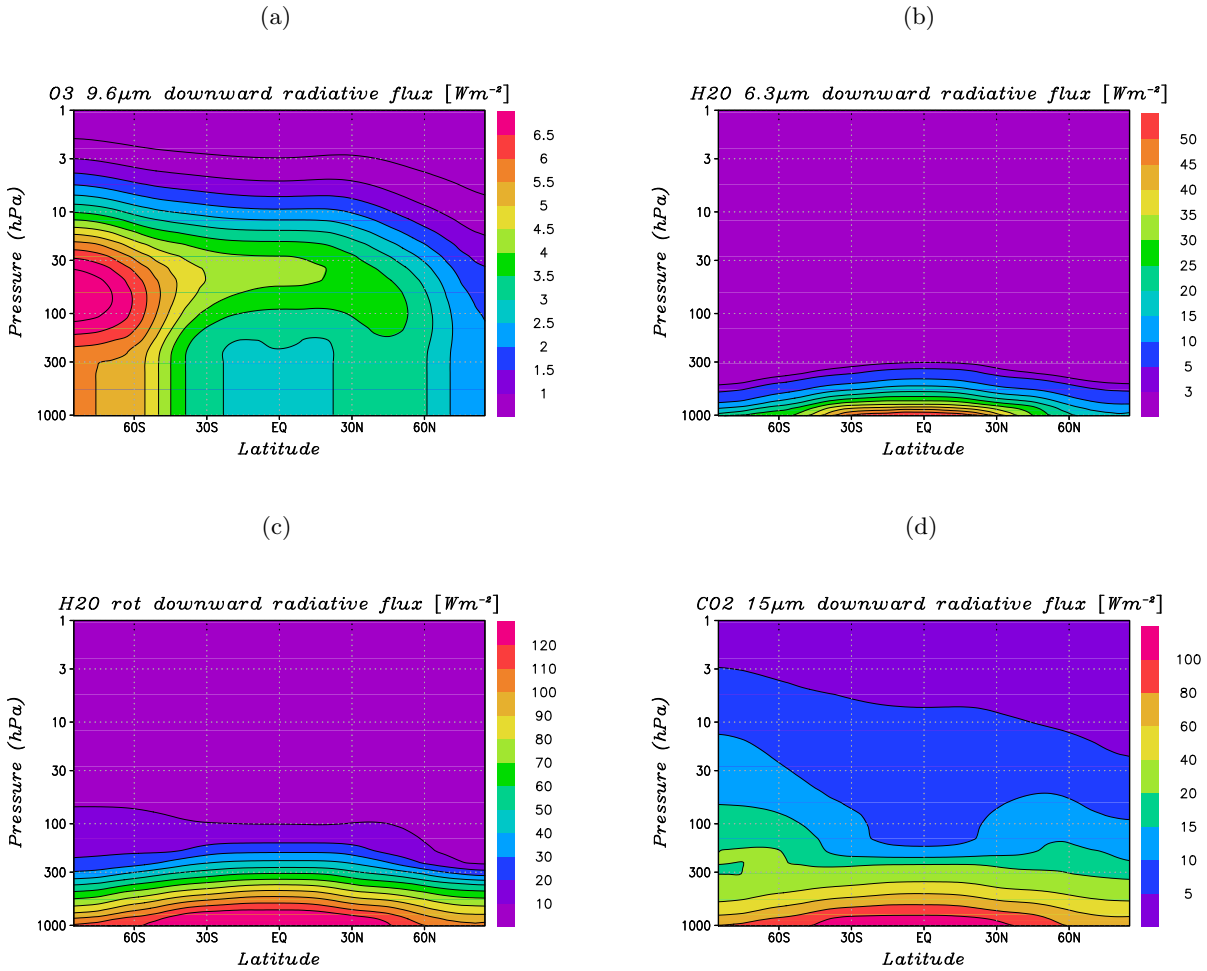

Figure 4.10: January mean downward radiative fluxes (Wm^{-2}) for (a) the ozone 9.6 μm band, (b) the water vapor 6.3 μm band, (c) the water vapor rotation continuum, and (d) the CO_2 15 μm band.

perturbation amplitudes. With regard to the frequency decomposition in (3.18), the upward perturbation amplitudes u^k are expected to be mainly negative if selective absorption at the line centers (maxima of κ_ν) predominates and positive if upward emission into the line centers prevails. Similarly, the downward perturbation amplitudes d^k are assumed to be positive due to selective downward emission into the line centers.

In Figurer 4.11 and 4.12, latitude-height distributions of the upward and downward perturbation amplitudes during January, respectively, are illustrated. The upward perturbation amplitudes generally indicate absorption at the line centers mainly in the troposphere. Due to the fact that the maximum of the ozone distribution is located in the stratosphere, the corresponding upward perturbation amplitudes of the ozone 9.6 μm band are nearly zero below the tropopause (panel a). The positive values of the upward perturbation amplitudes in the polar summer stratopause and above seen in the ozone band (panel a) and in the water vapor rotation band (panel c) can be explained by strong emission into the line centers from the warm summer stratopause region. Concerning the CO_2 15 μm band, the upward perturbation amplitudes are positive everywhere above the tropopause. The obvious explanation for this is that upward emission into the lines exceeds the absorption of upwelling radiation above this height and thereby leads to LW radiative cooling. Since the grayness parameter

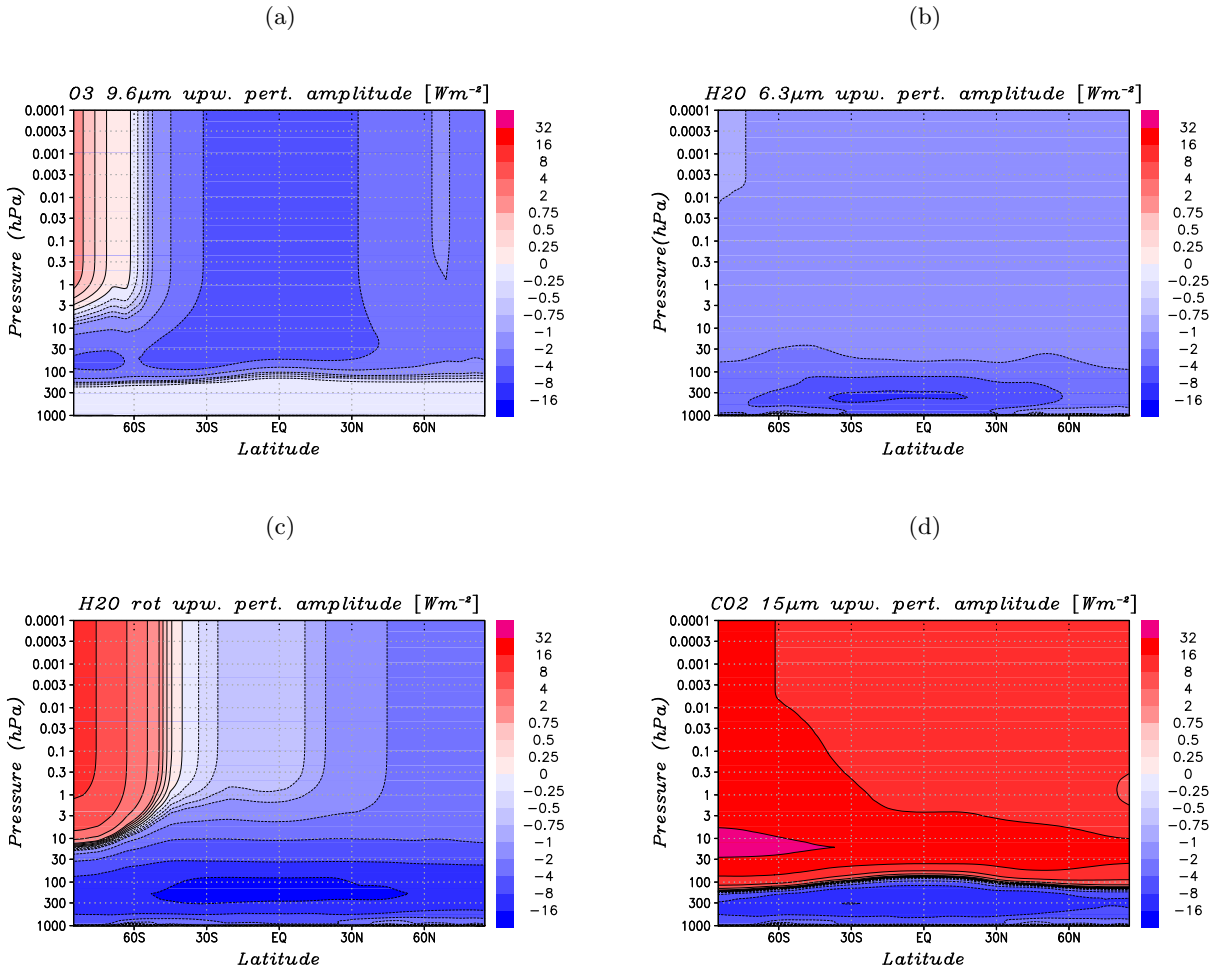

Figure 4.11: January mean upward perturbation radiative fluxes (Wm^{-2}) for (a) the ozone 9.6 μm band, (b) the water vapor 6.3 μm band, (c) the water vapor rotation continuum, and (d) the CO_2 15 μm band.

for the CO_2 band is very small above the tropopause (Figure 4.18 panel d), this cooling manifests itself by a positive upward perturbation amplitude. Comparing Figures 4.10 and 4.12 it can be noticed that the downward emission into the line centers reinforces the mean downward radiation everywhere for each of the four absorber bands.

Latitude-height cross-sections of the January mean short-wave heating rates due to O_2 and O_3, cooling rates in the CO_2 15 μm, the ozone 9.6 μm band, and the two water vapor bands together are given in Figure 4.13. These distributions are comparable to other results [London, 1980; Fomichev et al., 1986], except for the thermospheric heating (panel a) which is too weak with the present model tuning. One reason for this tuning is that the frictional heating due to the damping of tidal waves by momentum diffusion, as well as the complete gravity-wave heating are included in the model. The combined energy deposition yields an average heating rate of 10-20 Kd^{-1} in the lower thermosphere which is neglected in other global circulation models. The discrepancy in thermospheric short-wave heating may otherwise be attributed to the limited vertical model extent. The heating by ozone due to absorption in the Hartley-Huggins and Chappuis bands (see Figure 4.13 a), on the other hand, is tuned to yield realistic values around the stratopause. In the long-wave regime, ozone induces a cooling maximum of a few Kd^{-1} in the warm summer upper stratosphere (panel b) while the

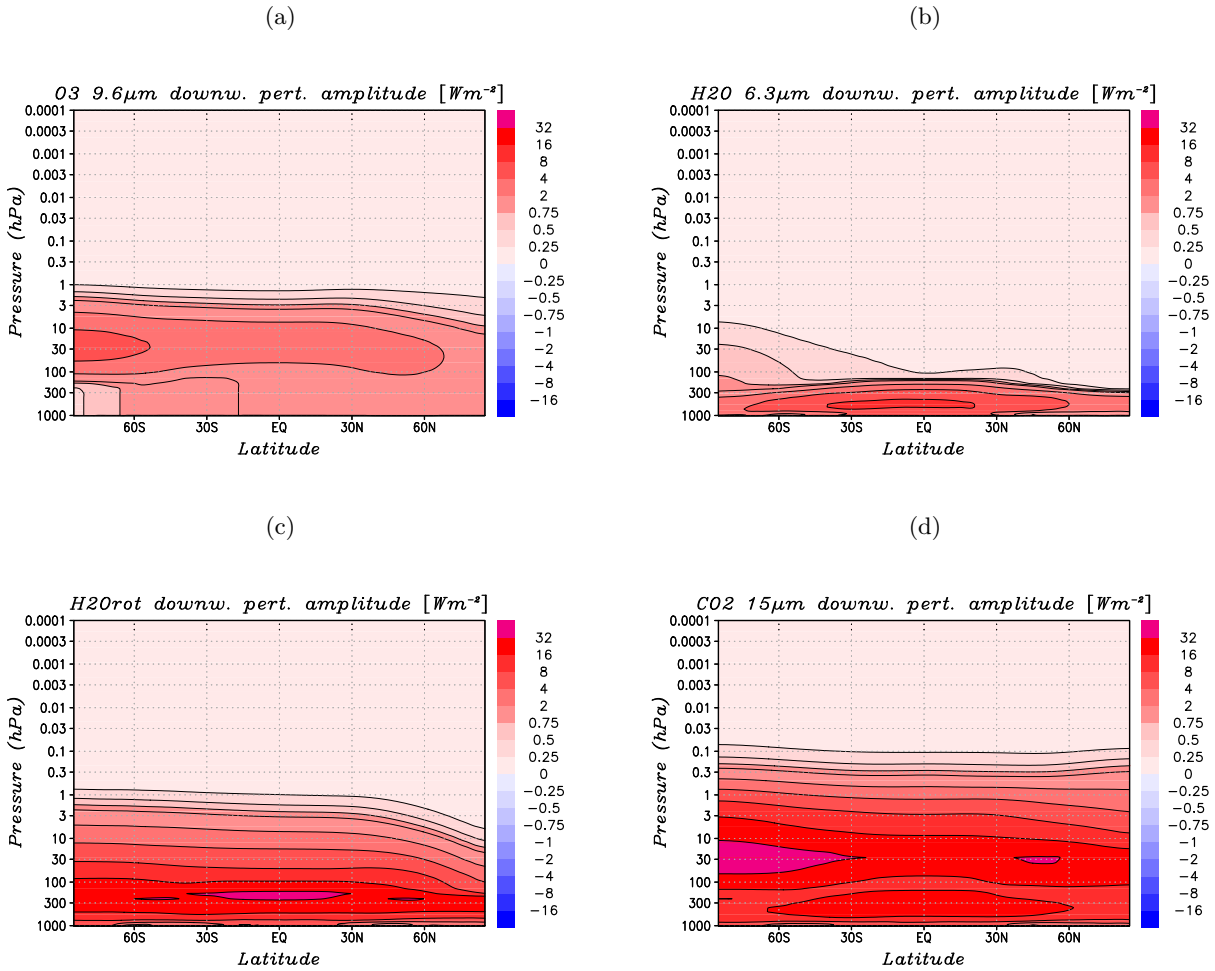

Figure 4.12: January mean downward perturbation radiative fluxes (Wm^{-2}) for (a) the ozone 9.6 μm band, (b) the water vapor 6.3 μm band, (c) the water vapor rotation continuum, and (d) the CO_2 15 μm band.

lower tropical stratosphere is heated by absorption of upward long-wave radiation. Water vapor leads to a cooling beneath the tropopause and has additional cooling or heating effects in the lower tropical stratosphere or the lower summer polar mesosphere of few Kd^{-1} (panel c). The CO_2 15 μm band cools the stratopause region and the thermosphere. At the cold summer mesopause, absorption of upward radiation leads to a heating rate of some Kd^{-1} in this band. Again, these results are widely consistent with other comprehensive middle atmosphere model results [Fomichev et al., 2002; Garcia et al., 2007] up to the mesopause region.

The non-LTE parameterization in terms of a band-averaged scattering albedo may be compared to a study of Dickinson [Dickinson, 1984]. For this purpose, profiles of the relative source function based on equations (3.50) and (3.51) were computed for the CO_2 15 μm band. The summer and winter profiles presented in Figure 4.15 are based on the simulated climatology displayed in Figure 4.2. Comparing the relative source functions to the corresponding profiles of Dickinson in Figure 4.14 for January and July shows quite a good correspondence, given the large differences in the methods and the sensitivity of the relative source function to the actual temperature profile.

The differing characteristics of the CO_2 15 μm source function for summer and winter

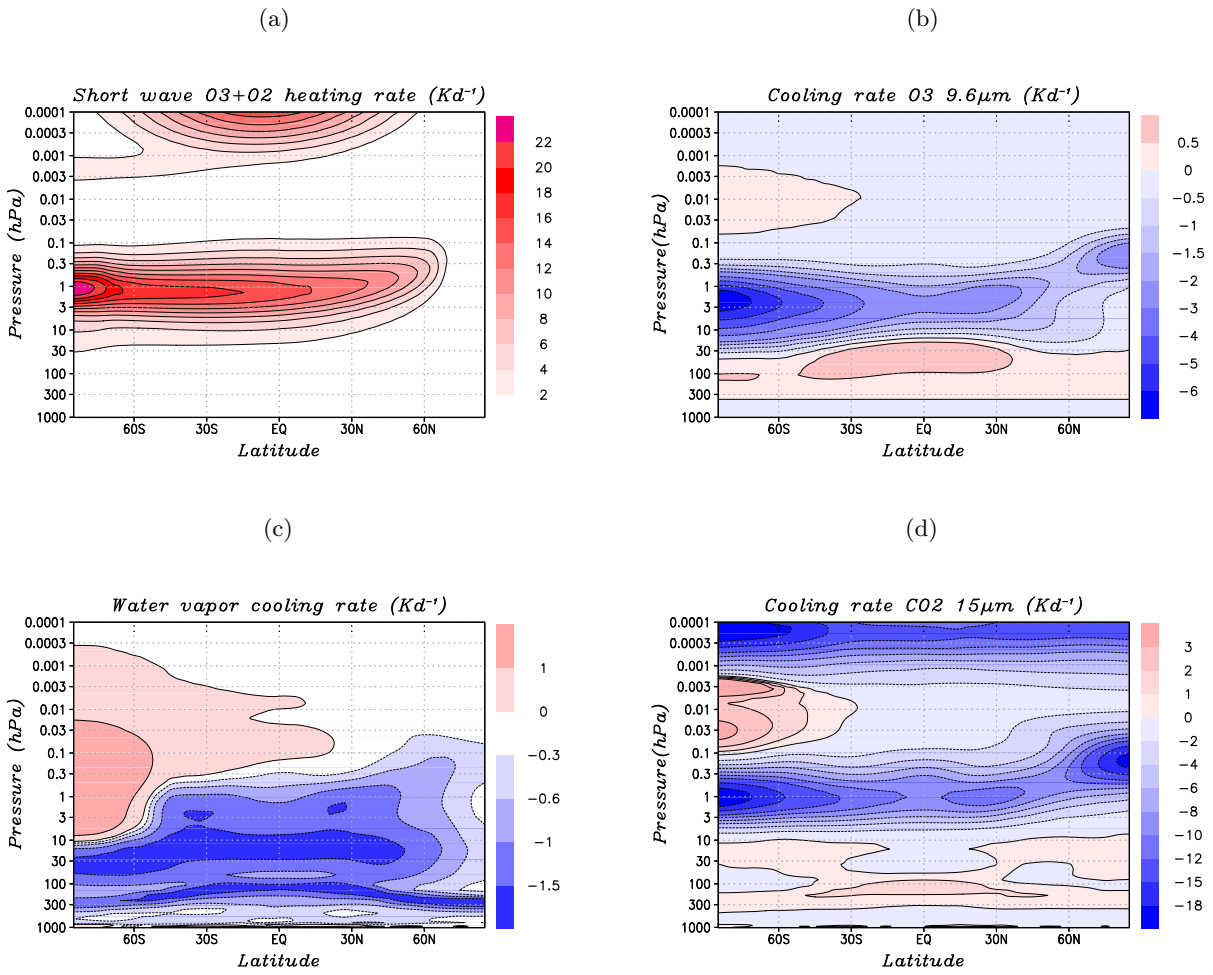

Figure 4.13: January mean of (a) the SW oxygen plus ozone heating rate, (b) the ozone 9.6 μm cooling rate, (c) the water vapor LW cooling rate, and (d) the CO_2 15 μm cooling rate. All values are given in Kd^{-1}.

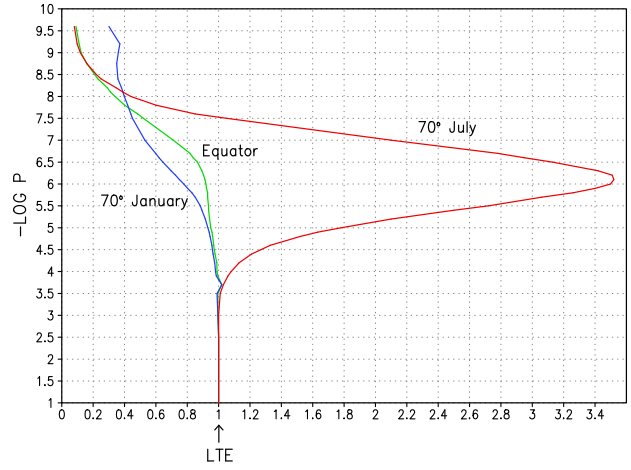

Figure 4.14: Relative non-LTE source functions for the CO_2 15 μm band according to Figure 7 of [Dickinson, 1984]. red: July 70N , blue: January 70N and green: equator

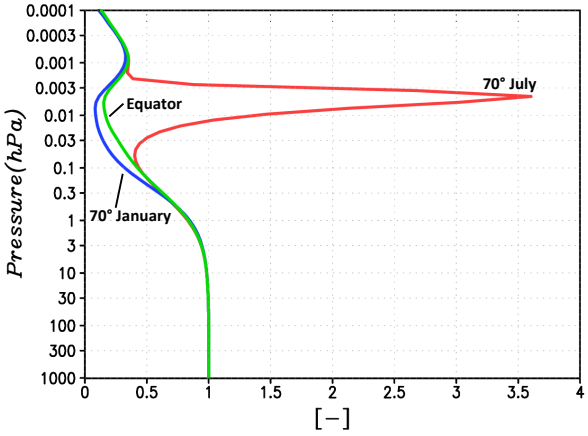

Figure 4.15: Relative non-LTE source function for the CO_2 15 μm band calculated from (3.50) and (3.51) at 70N July (red) , 70N January (blue) and at the equator (green). Five-year averages are applied to obtain the source functions.

conditions can be explained recalling the equations (3.50) and (3.51) and the temperature distributions in Figure 4.2. In the mesopause region, thermal emission is reduced by a finite single scattering albedo. Furthermore, the downward LW energy flux is negligible at these heights (Figure 4.10b). In summer, the reduced thermal emission around the cold mesopause is largely overcompensated by the scattering contribution to the source function, induced by a strong upward flux. This leads to the maximum of the source function for July seen in Figure 4.15. In winter the upper mesosphere temperatures are much higher than in summer. Hence the thermal emission is much higher too, despite the reduction due to non-LTE. As a result, the reduced emission at the mesopause is not completely compensated by scattering of the upward flux.

An additional verification of the non-LTE parameterization using the single scattering albedo as parameter can be achieved by comparing the heating rates for the LW bands of the test simulation to offline results obtained for doubling the number of inelastic collisions. A doubling of the collision rate corresponds to an underestimation of the deviations from LTE. For the CO_2 15 μm band this leads to an excessive cooling around the stratopause and the lower thermosphere, as well as to an overestimation of the LW heating around the polar summer mesospause. This sensitivity is further analyzed in Section 4.5.

4.4 Comparison with other model results and measurements

In the following, the global annual mean radiative energy budget at the TOA and the global annual mean surface energy budget calculated from the mechanistic model will be compared to other results. Trenberth collected a number of such energy balance studies for intercomparison [Trenberth et al., 2009].

In Table 4.1 the different components of the TOA energy balance computed with the mechanistic model are presented together with the corresponding values taken from Tables 1a and 2a of [Trenberth et al., 2009]. The results of the other investigations are based on satellite data and reanalyses. In the studies denoted by KT97 and ERBE FT08 the albedo is tuned to get a zero net radiation. In KT 09 the values of the surface albedo and the OLR are adjusted to decrease the net radiation to 0.9 Wm^{-2}. As discussed in [Trenberth et al., 2009], the differences in these values can for example be attributed to uncertainties in the tropospheric water vapor distribution, the absorption in the water vapor continuum, and radiative cloud properties or precipitation.

Data source	Solar in	Solar reflected	Albedo (%)	ASR	OLR	NET
This work	342.4	106.8	39.4	235.6	235.4	0.23
KT97	341.8	107	31	235	235	0.0
ERBE FT08	341.3	106.9	31.3	234.4	234.4	0.0
ISCCP-FD	341.8	105.9	31.0	235.8	233.3	2.5
NRA	341.9	115.6	33.8	226.3	237.4	-11.1
ERA-40	342.5	106.0	31.0	236.5	245.0	-8.5
JRA	339.1	95.2	28.1	234.8	253.9	-10.1
ISCCP	341.7	105.2	30.8	236.5	235.6	0.9
NRA	341.8	117.0	34.2	224.5	237.8	-13.0
JRA	339.1	94.6	27.9	244.5	253.6	-9.1
KT09	341.3	101.9	29.8	239.4	238.5	0.9

Table 4.1: TOA global annual mean radiation budget. The different contributions in Wm^{-2} listed separately for different models and measurements denote the incoming solar radiation, the solar radiation reflected back to space, the mean planetary albedo, the absorbed solar radiation, the outgoing LW radiation and the net radiation at the TOA. The numbers presented in the first row correspond to the test simulation obtained from the mechanistic model, compare Figure 4.5. The values in the following six rows below are based on data for the ERBE period of February 1985 to April 1989 and the quantities in the last for rows are derived from the CERES period of March 2000 to May 2004. Detailed information on the data and methods applied to calculate the tabulated values and further references are given in [Trenberth, 1997; Trenberth et al., 2009]

The numerical values of the different contributions to the TOA energy balance obtained using the mechanistic model compare well to the result of the other investigations (Table 4.1). Integrating the model further for about 5-10 years, the value of the net imbalance is expected to decrease further. In the model, a higher value for the planetary albedo is applied since reflection of SW radiation in the model takes place at the surface, i.e. after about 20 % of the incoming solar radiation is already absorbed by ozone and tropospheric water vapor. In the real atmosphere, the reflection is mainly due to clouds and aerosols in the mid and upper troposphere.

Data source	SW atm.	SW surf.	SW refl.	LH	SH	LW up	LW down	LW NET	Imb.
This work	69.4	166.2	106.8	32.3	8.0	416.9	292.3	-124.6	1.4
KT97	67	168	24	78	24	390	324	66	0
ISCCP-FD	164.9	105.9	24	-	-	395.9	344.8	51.1	-
NRA	64.4	161.9	45.2	80.2	15.3	395.5	334.1	61.5	4.9
ERA-40	80.7	155.8	23.1	82.3	15.3	394.8	340.3	54.4	3.8
JRA	75.0	168.9	25.6	85.1	18.8	395.6	324.3	73.1	-6.3
ISCCP	70.8	165.7	22.8	-	-	393.9	345.4	48.5	-
NRA	64.4	160.4	45.2	83.1	15.6	396.9	336.5	60.4	1.3
JRA	74.7	169.8	25.6	90.2	19.4	396.9	324.1	72.8	-12.6
KT09	78.2	161.2	23.1	80.0	17	396	333	63	0.9

Table 4.2: Surface global annual mean energy budget. The different contributions in Wm^{-2} listed separately for different models and measurements denote the solar radiation absorbed in the atmosphere, the solar radiation absorbed at the surface, the solar radiation reflected at the surface, the surface latent and sensible heat fluxes, the long-wave upward emission at the surface, the long-wave back radiation at the surface, the net long-wave radiation at the surface and the imbalance of the surface energy budget. The numbers in the first row are computed from the mechanistic model, compare (4.2). The values in the following six rows below are based on data for the ERBE period of February 1985 to April 1989 and the quantities in the last for rows are derived from the CERES period of March 2000 to May 2004. More detailed information on the data and methods applied to calculate the tabulated values and references are given in [Trenberth, 1997; Trenberth et al., 2009]

In Table 4.2, the different components of the global annual mean surface energy budget derived from the mechanistic model (first row) are listed together with the results of other investigations compiled in [Trenberth et al., 2009], see Tables 1b and 2b therein. The reason for a higher amount of solar energy reflected at the surface obtained using the mechanistic model is the same way as for the need of a higher surface albedo, see last paragraph. The latent and sensible heat fluxes in the model are much weaker compared to the other results. A possible explanation for this tuning is the lack of an explicit parameterizations of the tropospheric moisture cycle and convection processes in the present model setup, as well as the neglect of the cloud greenhouse effect, compare Chapter 4.1. Indeed, the long-wave downward radiation is about 40 Wm^{-2} less than the value found by Trenberth 2009.

Summarizing, the global annual mean energy balances at the top of the atmosphere and at the surface obtained from the mechanistic model are visualized in Figure 4.16. The major difference compared to the corresponding diagram of Trenberth [Trenberth et al., 2009], their Figure 1, is the lack of a realistic representation of cloud effects and the tropospheric moisture cycle in the mechanistic model. This results in underestimations of the downward long-wave radiation and the upward latent and sensible heat fluxes in the troposphere. The reflection of short-wave radiation by clouds is implicitly included by a higher value for the surface albedo.

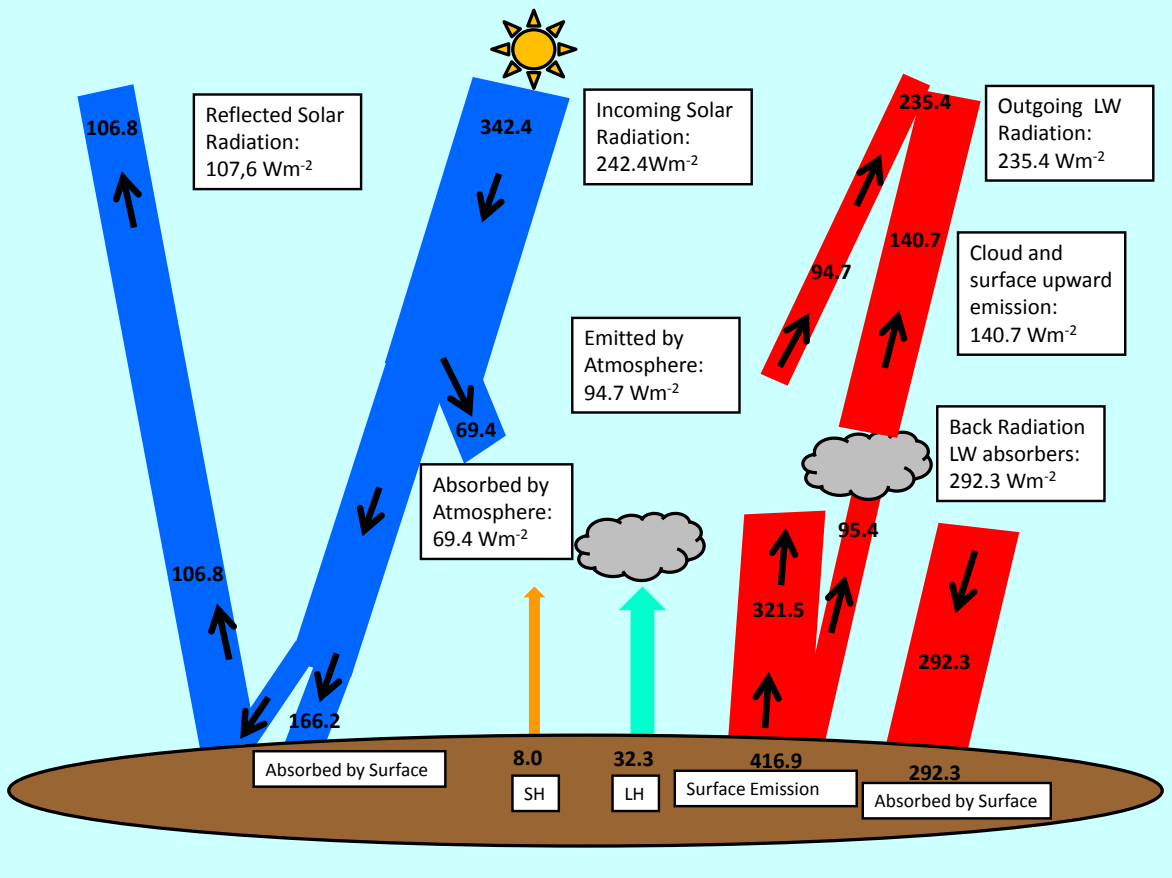

Figure 4.16: Diagram of the simulated global-mean energy flows through the earth system in analogy to Figure 1 of [Trenberth et al., 2009]. The numerical values of the energy fluxes are taken from Table 4.1 and 4.2. Short-wave radiative energy fluxes are given in blue and long-wave radiative energy fluxes are given in red.

4.5 Sensitivity of the LW cooling Rates to the number of collisions and to the grayness parameter

In this section, the parameterization of deviations from LTE using the single scattering albedo as non-LTE parameter and the inclusion of deviations from the gray limit by the solution of additional transfer equations will be further investigated. For that purpose, July latitude-height distributions of the single scattering albedo and the grayness parameter for the four long-wave absorber bands will be discussed first. After this, two offline experiments to extract the importance of each of the two effects to get the correct heating rates will be presented.

As discussed in section 2.2.3, the exponential decrease of air density with height leads to a reduction of the inelastic collisions such that the ratio of the number densities of energy levels follows no longer the Boltzmann distribution (2.86). In this case, the scattering part of the source function (2.62), which is parameterized by the single scattering albedo in the new radiation scheme, becomes important. Strong deviations from LTE correspond to a numerical value near 1 for the single scattering albedo ω (3.46) and will lead to a decrease in efficiency for both emission and absorption. In Figure 4.17 the single scattering albedo as applied in the test simulation is plotted for the four LW absorber bands. As mentioned at the end of Section 2.3.4, deviations from LTE for the ozone 9,6 μm band get significant above the stratopause pause panel (a) and the vibrational relaxation level of the CO_2 15 μm band is expected to be found at a height of about 70 km panel (d). In the mesospause region, the single scattering albedo for the CO_2 15 μm band decreases with height due to the increase of inelastic collisions with atomic oxygen [Fomichev et al., 2002]. Concerning the water vapor bands, non-LTE effects for the vibrational 6,3 μm band are expected to be important above about 60 km, panel (b), whereas LTE can be assumed for the rotation continuum, panel (c). As explained in Section 3, the grayness parameter y measures the importance of the frequency variation inside the broad long-wave absorber bands k. In the Elsasser band parameterization y determines the magnitude of the covariances between the radiative energy fluxes and the absorption coefficients and thereby the coupling of the flux perturbation amplitudes to the mean energy flux densities. July latitude-height distributions for the grayness parameters of the four bands are shown in Figure 4.18. For the ozone 9.6 μm band (panel a) and the CO_2 15 μm band (panel d) which are characterized by a large line density in their line spectra, a gray atmosphere can be assumed for the troposphere. Concerning the two water vapor bands (panel b and c), the grayness parameter is small already in the troposphere, such that it is important to include the frequency variation in the whole model domain for these bands. The increasing value of the grayness parameter in the thermosphere for example in the ozone 9.6 μm band is associated with the increasing Doppler line width (3.45) due to high temperatures dominating in this height region.

In Figure 4.19, July zonal-mean radiative heating rates obtained from the test simulation with deviations from the gray limit and from LTE correctly included by the new radiation scheme are presented. These heating rates provide the references against which the results from two offline computations will be compared, as discussed in the following. These offline computations are defined by diagnosing the radiation quantities from the test simulation already described; however, we use altered radiation parameters for this diagnosis.

To evaluate the effects of deviations from LTE on the resulting cooling rates, an offline test with the number of inelastic collisions for each long-wave band doubled is calculated. The doubling of the collision rates is realized by multiplying the numerical values a^k appearing in (3.48) by a factor of two, which leads to an underestimation of non-LTE. The corresponding cooling rates are given in Figure 4.20. Comparing these cooling rates to the reference case in Figure 4.19, the strongest impact is observed for the CO_2 15 μm band, as expected.

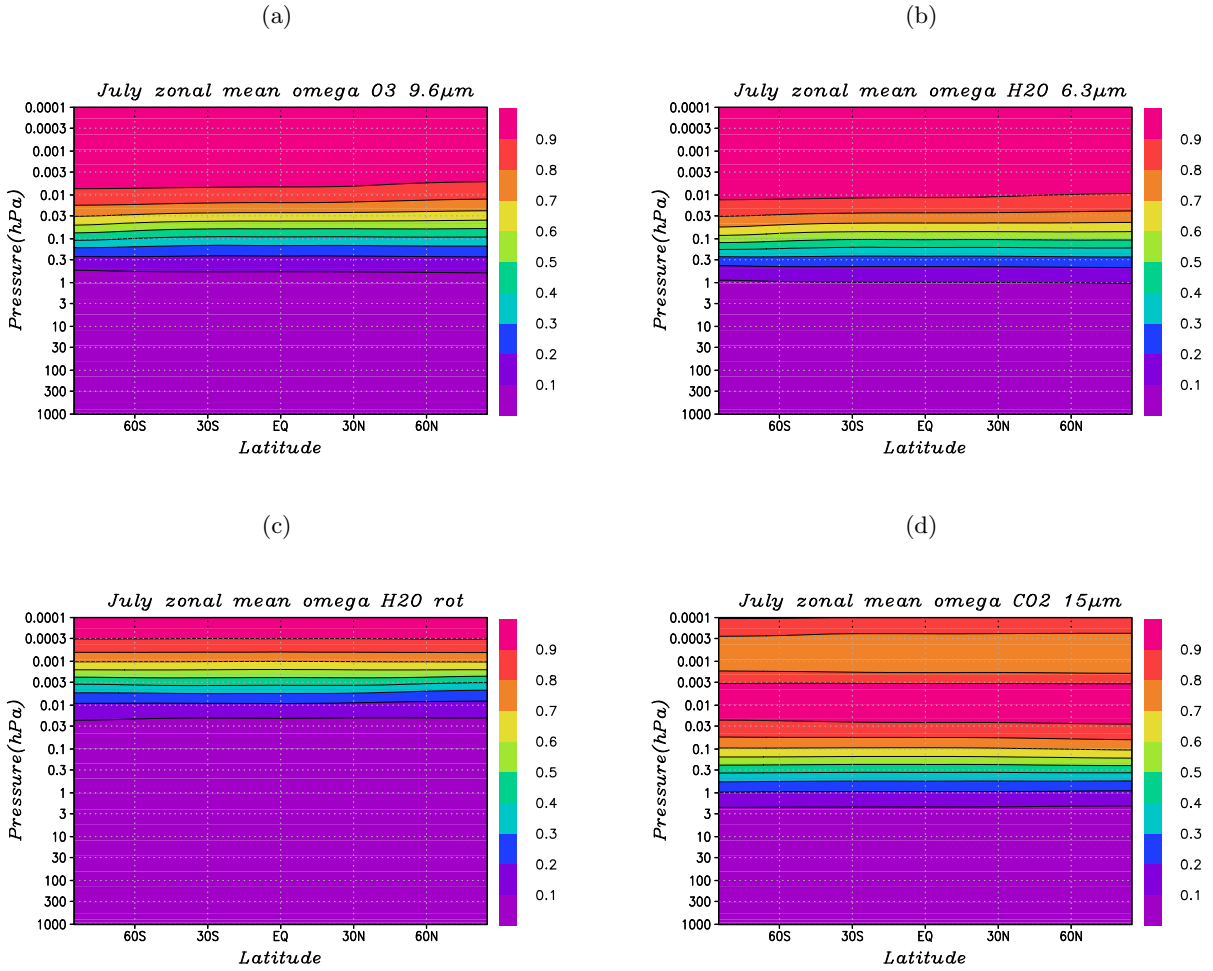

Figure 4.17: July monthly and zonal mean single scattering albedo (3.46) for (a) the ozone 9.6 μm band, (b) the water vapor 6.3 μm band, (c) the water vapor rotation band, and (d) the CO_2 15 μm band.

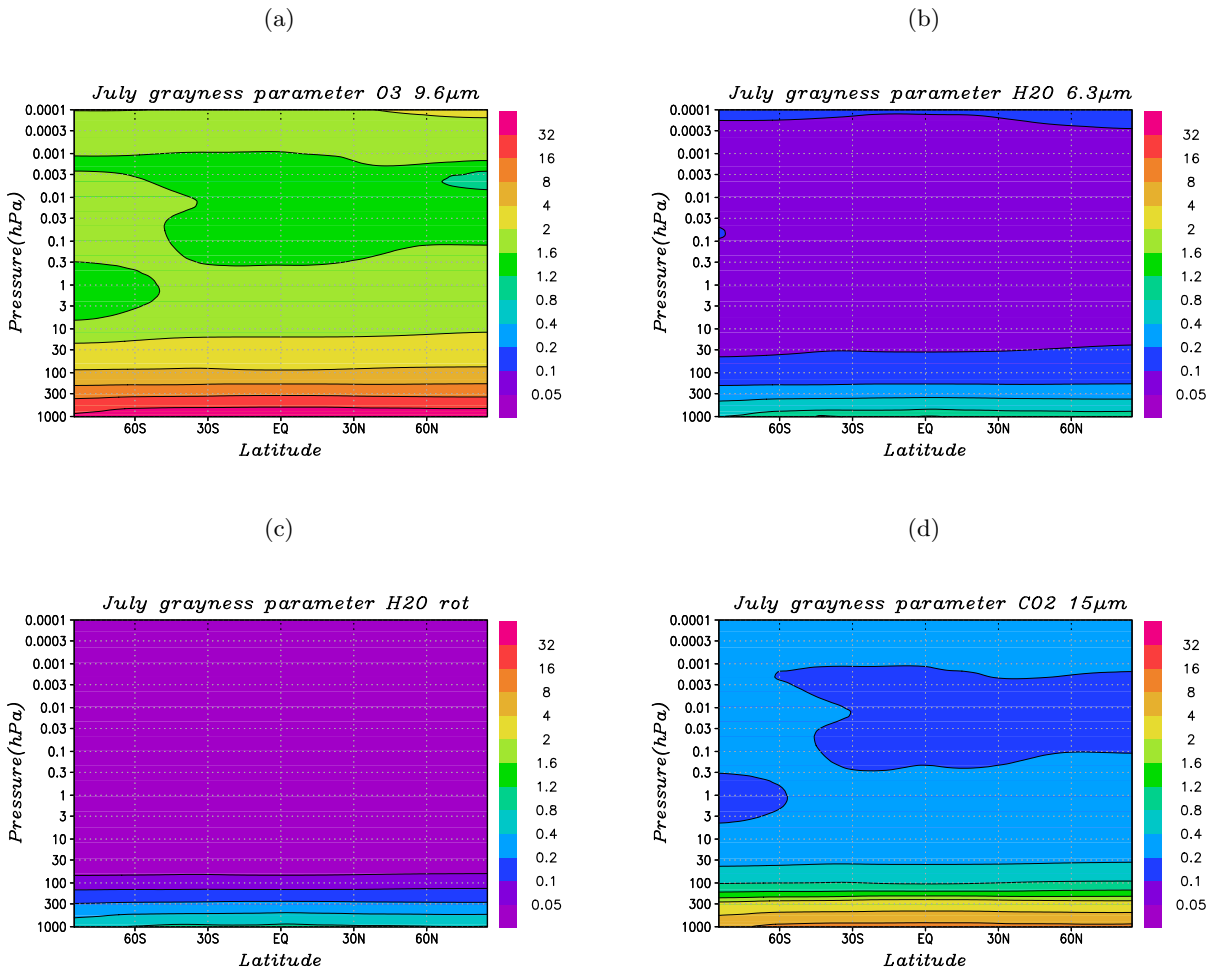

Figure 4.18: July monthly and zonal mean grayness parameter $y = \gamma^k(p,T)/\delta$ for (a) the ozone 9.6 μm band, (b) the water vapor 6.3 μm band, (c) the water vapor rotation band, and (d) the CO_2 15 μm band

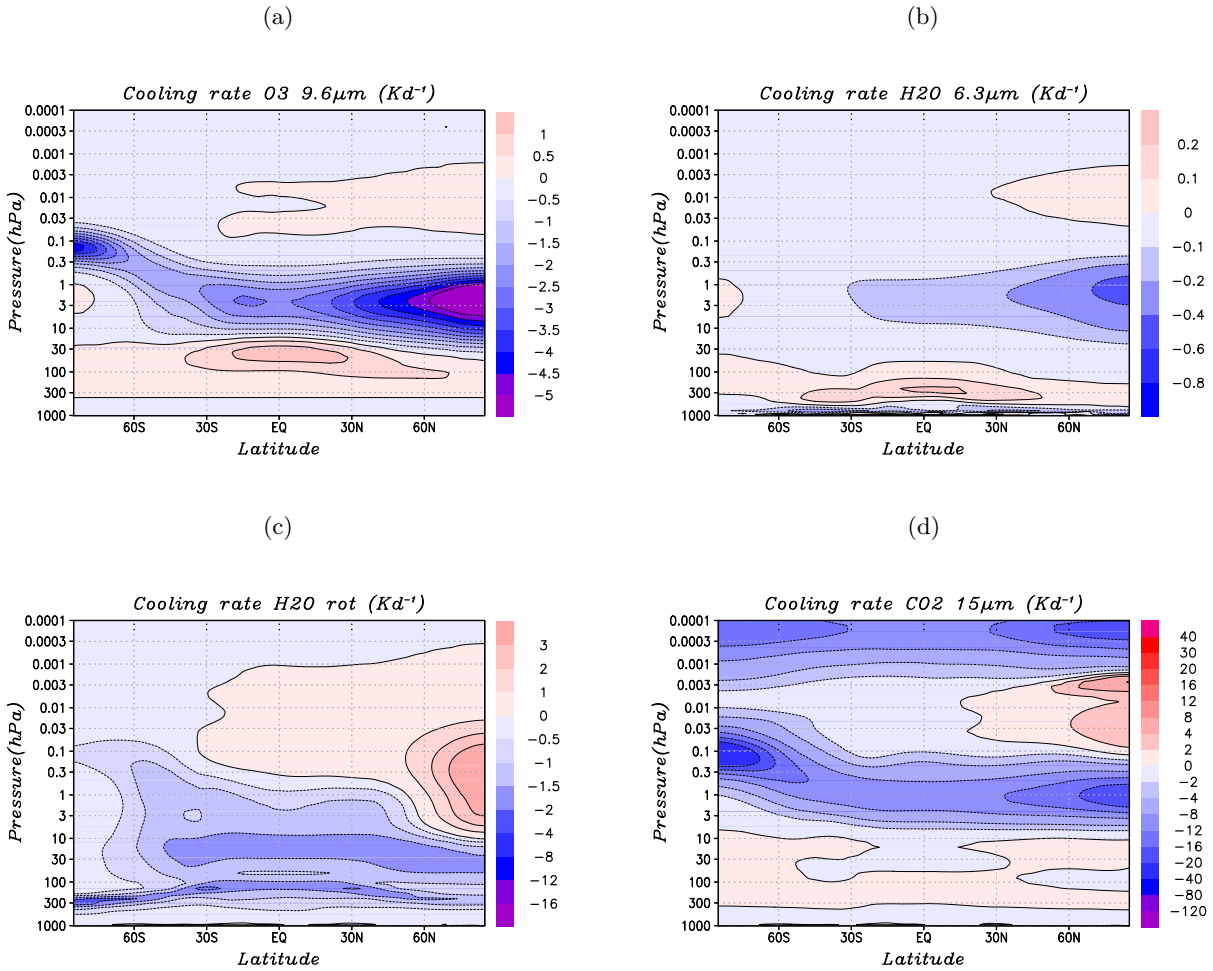

Figure 4.19: July mean long-wave cooling rates for (a) the ozone 9.6 μm band, (b) the water vapor 6.3 μm band, (c) the water vapor rotation band, and (d) the CO_2 15 μm band. All values are given in Kd^{-1}.

Both the cooling and heating in the middle atmosphere are largely overestimated for this band. In the cold summer mesopause region an additional heating of 10 Kd^{-1} occurs and the thermosphere is cooled by 30 Kd^{-1}. These effects depend strongly on the inelastic collisions with atomic oxygen [Fomichev et al., 2002]. Concerning the ozone 9.6 μm band, additional non-LTE effects would be expected on the mesospheric cooling due to an ozone maximum in the mesopause region [London, 1980] (compare panel (a) of Figure 4.17), which is not included in the present model setup. The changes in the water vapor bands are negligible (panel b and c).

Neglecting the frequency variation inside the long-wave absorber band by setting the grayness parameter y to a large value of 1000, our second offline test leads to the cooling rates shown in Figure 4.21. Whereas the cooling of the middle atmosphere by the ozone 9.6 μm band (panel a) and the vater vapor 6.3 μm band (panel b) is only slightly increased, the cooling and heating effects in the water vapor rotation band (panel c, excess cooling of about 16 Kd^{-1} in the stratosphere) and the CO_2 15 μm band (panel d, excess cooling of 100 Kd^{-1} (!) and excess heating of 10 Kd^{-1}) are largely amplified when assuming a gray atmosphere from the surface to the top of the model domain. Indeed, when the grayness parameter is small, emission and absorption is confined to the line centers. Ignoring this fact leads to substantial

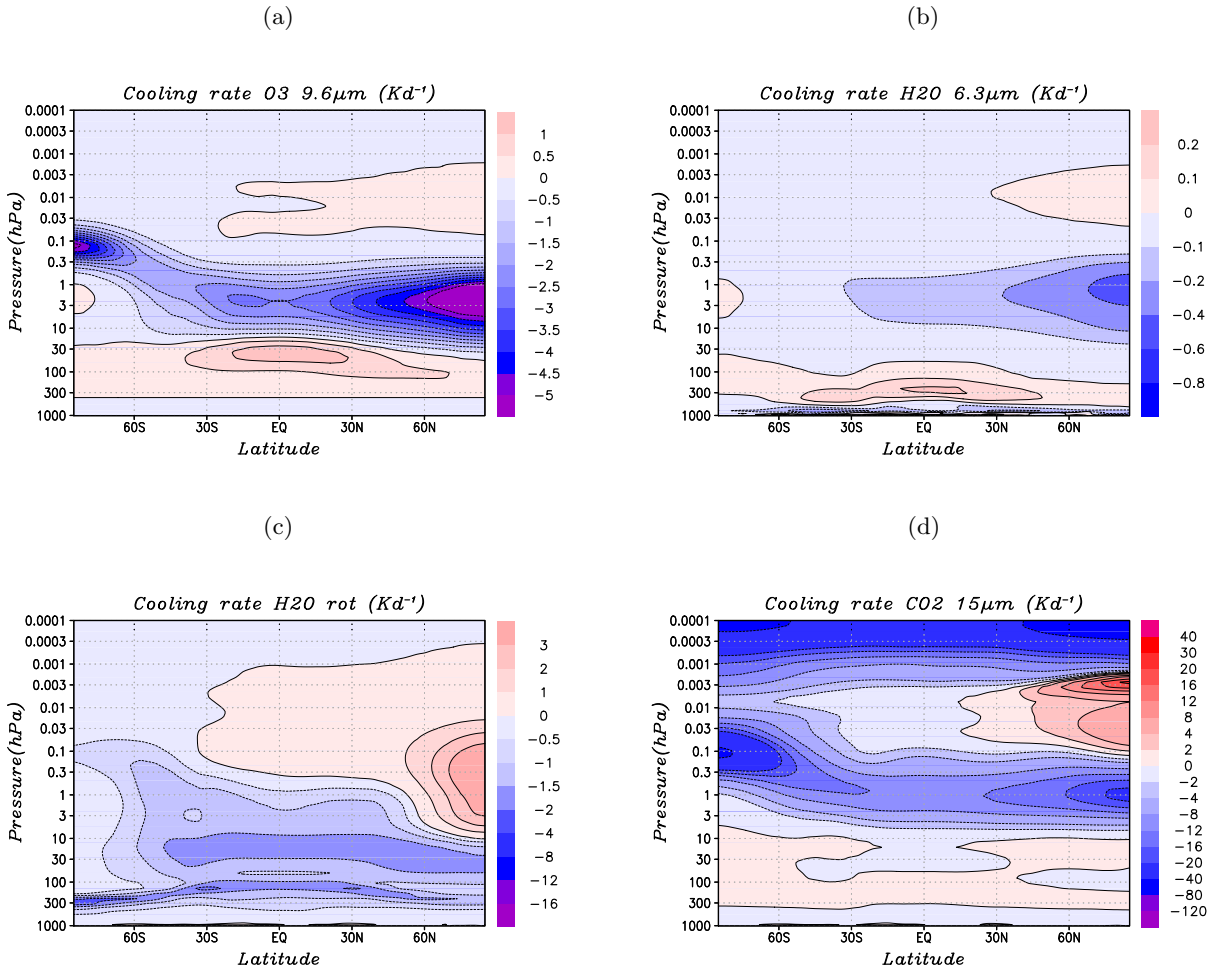

Figure 4.20: July zonal mean long-wave cooling rates corresponding to the doubled inelastic collision rates for (a) the ozone 9.6 μm band, (b) the water vapor 6.3 μm and, (c) the water vapor rotation band, and (d) the CO_2 15 μm band. All values are given in Kd^{-1}.

overestimations of both the heating and the cooling rates in the long-wave regime.

In summary, deviations from LTE are found to be most important for the CO_2 15 μm band whereas deviations from the gray limit have large impacts on the cooling rates of the CO_2 15 μm band and the water vapor rotation band. In the new radiation scheme both effects are consistently included for all long-wave bands.

4.6 Variability

In the following, results from applying the mechanistic model including the new radiation parameterization to investigate some questions concerning climate variability are presented. First, we investigate the annual cycle of the TOA energy balance. After this, the middle atmospheric radiative and dynamical response to an increase of the CO_2 abundance will be evaluated. The impact of doubling the CO_2 amount on the residual circulation is another physical mechanism to be considered here since it can modulate the gravity wave driving in the summer-MLT.

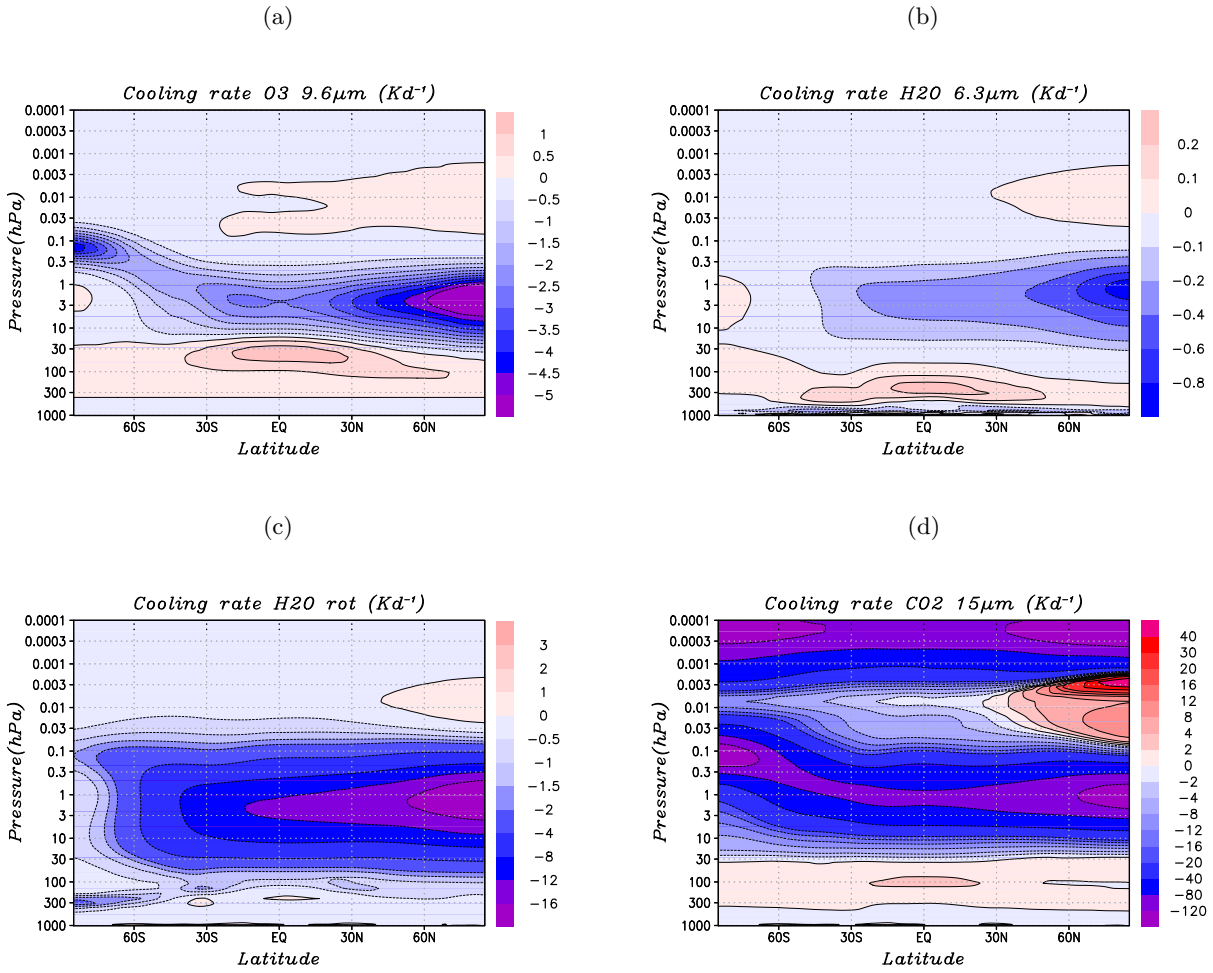

Figure 4.21: July zonal mean cooling rates corresponding to a grayness parameter of $y = 1000$ valid throughout the whole atmosphere for (a) the ozone 9.6 μm band, (b) the water vapor 6.3 μm band, (c) the water vapor rotation band, and (d) the CO_2 15 μm band. All values are given in Kd^{-1}.

(a)

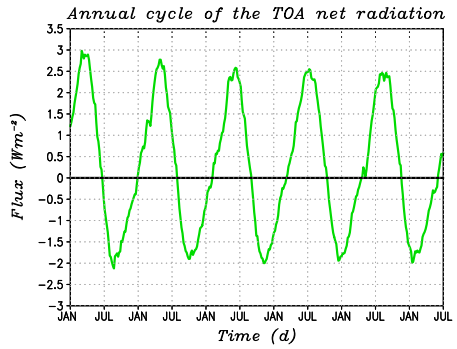

(b)

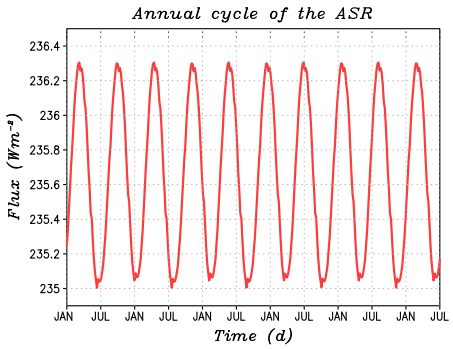

(c)

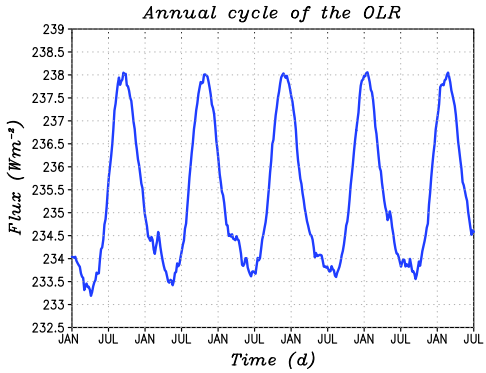

Figure 4.22: Annual cycle of (a) the global mean radiative forcing, (b) the outgoing long-wave radiation, and (c) the absorbed solar radiation. The unit is (Wm^{-2}).

4.6.1 Annual cycle of the TOA radiation budget

In this section the time-dependence of the global-mean net radiation at the TOA is investigated. Figure 4.22 a shows the time variation of the global-mean net radiative forcing at the top of the atmosphere (TOA). A pronounced annual cycle with maxima of about 3 Wm^{-2} during northern hemisphere (NH) late winter and minima of about -1.8 Wm^{-2} during southern hemisphere (SH) late winter can be observed. The absorbed solar radiation shown in panel (b) is characterized by a semiannual cycle with maxima during late NH and SH winter. This time variation of the ASR does not contribute to the annual cycle of the TOA radiation. On the other hand, as can be seen in panel (c), the annual cycle of the outgoing long-wave radiation is anti-correlated with the net radiation. In particular a greater loss of long-wave radiative energy during SH late winter leads to the corresponding minima in the TOA radiation budget, whereas the weaker loss of long-wave radiative energy during NH late winter explains the maxima.

Due to the fact that emission to space is most effective in the tropics compared to higher latitude regions (see the blue curve in Figure 4.5) the annual cycle of the OLR can be expected to depend on the annual cycle of temperature at low latitudes. Such an annual cycle of temperature in the tropical lower stratosphere is for example observed by Yulaeva et al. applying satellite measurements [Yulaeva et al., 1994]. A plausible explanation for the annual cycle of the tropical lower stratospheric temperature can be found in the north-south asymmetry of the midlatitude planetary wave activity during the winter season. Land-sea

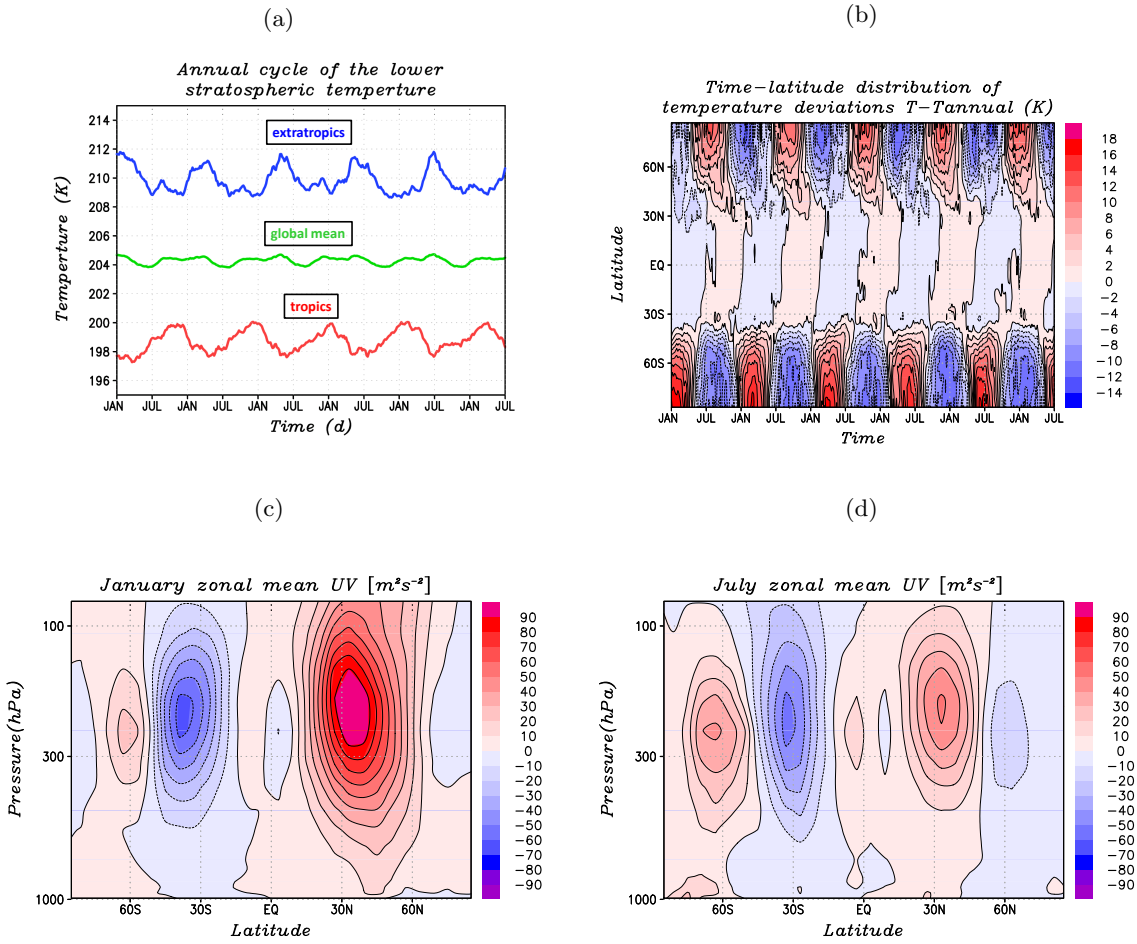

Figure 4.23: (a) Annual cycle of the global mean, tropical (30°S - 30°N) and extratropical (30° - 90°) lower stratospheric temperature (K) computed as averages between 150 and 40 hPa (b) Temperature deviation from the over 5 years averaged mean Temperature (K) (c) and (d) over 5 years averaged monthly means of u^*v^* for January and July (m^2s^{-2})

differences and orography lead to a stronger planetary wave driving of the lower part of the residual circulation in the stratosphere of the northern hemisphere compared to the southern hemisphere. The corresponding stronger upwelling in the tropics explains the lower temperatures observed in the tropical lower stratosphere during NH winter. Also in the troposphere, the annual cycle in the planetary wave activity leads to a more efficient meridional heat transport from the tropics to higher latitudes and hence lower tropical temperatures during late NH winter than during SH winter (not shown).

In the first two panels of Figure 4.23, annual cycles of the lower stratospheric temperature and a latitude-time sections of temperature deviations from the annual mean temperature, as discussed in [Yulaeva et al., 1994], are reproduced from the mechanistic model. In panel (a) the global mean temperature of the lower stratosphere varies only weakly during the course of the year. As expected the annual cycles of the lower stratospheric temperature in the tropics and extratropics are anti-correlated. In general, the lower stratospheric temperature is about 6 K lower in the tropics and about 6 K higher in the extratropics compared to the global mean value. In panel (b) a latitude-time section of temperature deviations from the annual mean temperature is presented. In general, it can again be seen that the temperature in the tropics deviates much less from the annual mean value than in the extratropics. During

the winter seasons of both hemispheres, heat is redistributed from the tropics toward higher latitudes. Finally panels (c) and (d) show latitude-height sections of monthly mean $[u^*v^*]$, which is a measure of Rossby-wave activity, for January and July. Looking at these panels the expected stronger wave activity during northern hemisphere winter is confirmed.

Comparing the results obtained with the mechanistic model to the satellite observations used by Yulaeva et al., the general features concerning the annual cycle of the lower stratospheric temperature and the underlying north-south asymmetry in the planetary wave forcing are reproduced. However, some differences concerning the phase of the annual cycle of the lower stratospheric temperatures should be noted. We attribute this disagreement to the mechanistic character of the general circulation model, especially with regard to the simplistic latent heating.

The differences in magnitude between the maxima and minima of the TOA net radiative forcing (Figure 4.22) are expected to be reduced when the model is integrated further for several years (compare Chapter 2.1.1).

4.6.2 Middle atmospheric response to an increase in CO2 abundance

In this subsection an overview of the expected response of the atmosphere to a doubling of the CO_2 amount is presented. After this some results from a CO_2 doubling experiment obtained using the mechanistic model will be discussed. In this context, our focus lies mainly on the effects in the mesosphere. To reliably simulate the effects of increased CO_2 below the stratopause, an explicit tropospheric moisture cycle must be included in the model first [Frierson et al., 2007]. This is out of the scope of this work.

The response of the atmosphere to an increase of the CO_2 amount can generally be divided into a radiative-photochemical effect and into changes of the dynamics resulting from the temperature increase in the troposphere [Fomichev et al., 2007]. Considering the sensitivity to a doubling of the CO_2 amount in a simple radiative-convective framework, a radiative forcing of about $4\mathrm{Wm}^{-2}$ at the tropopause and a corresponding height independent temperature increase in the troposphere of about 1 K is obtained, compare [Held and Soden, 2000] their Figure 1. Allowing for a water vapor feedback by assuming a fixed relative humidity leads to a temperature increase of about 1.7K. Including in addition the ice-albedo and other feedbacks within the framework of comprehensive climate models results in a global mean temperature change of about 1.5 - 4.5K, see Figure 4 of [Held and Soden, 2000]. Therefore, to obtain this magnitude of the surface temperature change, which corresponds to the predictions summarized in the IPCC report 2007 [Forster et al., 2007], it is indispensable to include the water vapor feedback. The water vapor feedback can be explained as follows: Due to the strong increase of the saturation water vapor pressure with increasing temperature (Clausius-Clapeyron relation), a for example purely CO_2 induced warming of the troposphere by 1K is expected to result in an increased relative humidity of about 7%. The additional water vapor is brought into the atmosphere by stronger evaporation and convection and reinforces the tropospheric greenhouse effect. Such a mechanism is called a positive feedback loop. In addition, the increased water vapor content of the troposphere is responsible for a stronger absorption of solar radiation, leading possibly to stronger sources of thermal tides [Lindzen, 1990]. The water vapor feedback leads to uncertainties in many state-of-the-art climate models [Held and Soden, 2000].

Above the tropopause, a doubling of the CO_2 amount leads to an additional long-wave cooling to space and therefore to a temperature decrease in most parts of the middle atmosphere. Fomichev et al. obtain a maximum temperature reduction of about 10K at the stratopause when applying the CMAM to investigate the sensitivity to a CO_2 increase, [Fomichev et al.,

2007], their Figure 10a. This temperature reduction is compensated on the one hand by a decrease of the cooling in the O_3 9.6 μm band and on the other hand by an increase in solar heating due to CO_2. At the summer mesopause, the heating due to absorption of upwelling long-wave radiation exceeds the increase in the cooling to space, leading to LW warming in this height region due to a CO_2 doubling.

In response to the changes in the troposphere induced by an increased amount of CO_2, a number of dynamical effects are expected and partially observed already. Due to an increased wave driving the Brewer-Dobson circulation in the stratosphere presumably intensifies [Garcia and Randel, 2008] their Figure 1. As shown by McLandress and Shepherd, an upward shift of the location of critical layers within the subtropical lower stratosphere can robustly and in a unified manner explain how different waves (planetary- and synoptic-scale Rossby waves, as well as parameterized orographic gravity waves) can contribute to a strengthening of the Brower-Dobson circulations [Shepherd and McLandress, 2010]. The underlying mechanism can be explained as follows: The warming of the troposphere predicted by climate models leads to an strengthening of the upper flanks of the subtropical jets, compare Figure 1 of Shepherd and McLandress, which in turn leads to an upward-shift of the critical layers on the equatorward side of the subtropical jets. This allows a deeper penetration of Rossby waves and orographic GWs into the stratosphere and thereby leads to an enhanced wave driving. However, observational estimates of the age of air by Engel et al. [Engel et al., 2009] do neither confirm nor falsify the model predictions for this quantity as deduced from the altered Brewer-Dobson circulation [Bönisch et al., 2011].

The mesospheric part of the residual circulation is expected to change as well in response to an increased amount of CO_2: Caused by a CO_2-induced acceleration of the tropospheric westwind jets, Fomichev and colleagues noted an increased filtering of eastward propagating gravity waves in middle latitudes [Fomichev et al., 2007]. As a result, the residual circulation in the summer mesopause region slows down and a warming of the summer mesopause takes place in accordance with the corresponding reduction of the adiabatic cooling. Conversely, using a previous version of the mechanistic general circulation model with resolved GWs, it was shown that changes of the tropospheric static stability and the latent heating, which result from the tropospheric climate change, can lead to a stronger dissipation of mesoscale kinetic energy in the troposphere. This furthermore implies an accelerated tropospheric Lorenz energy cycle (globally integrated dissipation increased from 2.29 $\mathrm{Wm}^{-}2$ to 2.68 Wm^{-2}) which in turn is related to a stronger generation of gravity waves. These larger amplitude GW waves are damped lower down in the mesosphere and deposit more momentum on the mean flow compared to the unperturbed situation. Therefore, the middle atmospheric residual circulation is intensified and shifted downward [Becker, 2009].

In the following, some results applying the mechanistic model to investigate the sensitivity of the middle atmosphere to an increase of the CO_2 amount from 480 ppmv to 960 ppmv are presented. Since the present model setup includes no explicit parameterization of the hydrological cycle and chemistry or tracer transport, the water vapor feedback, the chemical response, and cloud effects are not considered in the following discussion. In Figure 4.24 the mesospheric model response to doubling the CO_2 amount is shown in terms of latitude-height distributions of January zonal-mean changes in the temperature (a), the zonal wind (b), the radiative heating in the CO_2 15 μm band (e), the large-scale dynamic heating (c) and the subscale heating (e). The subscale heating contains contributions from vertical and horizontal diffusion and dissipation as well as the direct thermal effects of parameterized gravity waves [Becker and McLandres, 2009]. The warming of the cold summer mesopause due to absorption of upwelling long-wave radiation, and the cooling of the summer stratopause in the CO_2 15 μm band (compare Figure 4.13 panel (d)) are both amplified due to the doubled CO_2 amount,

as can be seen in panel (e) of Figure 4.24. Considering the changes in the large-scale dynamic heating rates, panel (c), an additional heating of about 8 Kd^{-1} in the high latitude winter mesosphere and a narrow layer of strong dynamic cooling (about -28 Kd^{-1}) in the summer mesopause are the most prominent features. The subscale heating, panel (d), shows a strong narrow maximum (about 32 Kd^{-1}) at the could summer mesopause. Some smaller heating maxima can be seen in the lower latitude thermosphere and some cooling is seen in the winter lower mesosphere and above the heating maximum in the polar summer mesopause region. The maxima and minima in panels (c) and (d) are possibly associated with an enhanced upward propagation of gravity waves due to changed propagation conditions.

In panel (a) of Figure 4.24 the temperature response to a doubling the of the CO_2 amount is presented. The most important radiative and dynamic effects discussed above are reflected by the corresponding changes seen in the temperature structure. Apart from the region of temperature increase around the summer mesopause, a general cooling of the middle atmosphere can be observed as expected. The corresponding changes of the zonal-mean wind (gradient wind balance see Appendix A) are displayed in panel (b). The additional warming of the polar summer mesosphere leads to an anomalous easterly wind component whereas the enhancement of the westerly winds in the winter mesosphere is associated with the cooling of the winter stratopause. The large scale dynamic heating response and the subscale heating response seem to counteract, but do not compensate each other, as can be seen for example in the summer mesopause region and in the winter mesosphere. The January zonal mean wind response to a doubling of CO_2 generally shows a strong inter-annual variability, which is also the case in the present model (not shown). Comparing the temperature response shown in panel (a) to the comprehensive study done by Fomichev 2007 [Fomichev et al., 2007], the result is roughly comparable to their simulation (their Figure 10c). We note that the present model also shows a warming below 5 hPa (not shown) which is not seen by Fomichev et al.

In Figure 4.25 the modulation of the gravity wave driving of the residual circulation induced by a doubling of the CO_2 amount is analyzed with the focus lying on the southern summer MLT. The radiatively induced temperature increase in the summer mesopause region (panel a) leads to an anomalous easterly wind component, as shown in panel (b). Therefore eastward propagating gravity waves can propagate farther upward (compare Figure A.1 in Appendix A) such that the level of momentum deposition is shifted upward too. This explains the dipole structure in the gravity-wave drag response in panel (d). Accordingly, also the residual circulation is shifted upward, which can be seen for example from the changes of the residual meridional wind panel (c).

This upward shift of the residual circulation induced by the radiative part of the response to an increase of the CO_2 amount with fixed parameterized gravity wave sources (replotted in panel (a) of Figure 4.26) can be compared to the effects on the dynamics of the middle atmosphere assuming no changes in the CO_2 amount but prescribing changes of the latent heat sources and the static stability in the troposphere (panel (b) of Figure 4.26) [Becker, 2009]. The corresponding model response was calculated applying a different setup of the mechanistic model with temperature relaxation as a surrogate for a radiation parameterization and high resolution to resolve part of the gravity wave spectrum as mentioned earlier in this subsetion. The model showed an enhancement of the Lorenz energy cycle in tandem with stronger GW sources in the troposphere [Becker, 2009]. As a consequence the large amplitude upward propagating waves break lower down, which in turn leads to a downward shift of the residual circulation as seen in panel (b) of Figure 4.26. Correspondingly the adiabatic cooling region below the mesopause is stronger and leads to lower temperatures in accordance with the downward control principle [Haynes et al., 1991].

In summary, the two possible impacts of doubling the CO_2 amount on the summer MLT

(a)

(b)

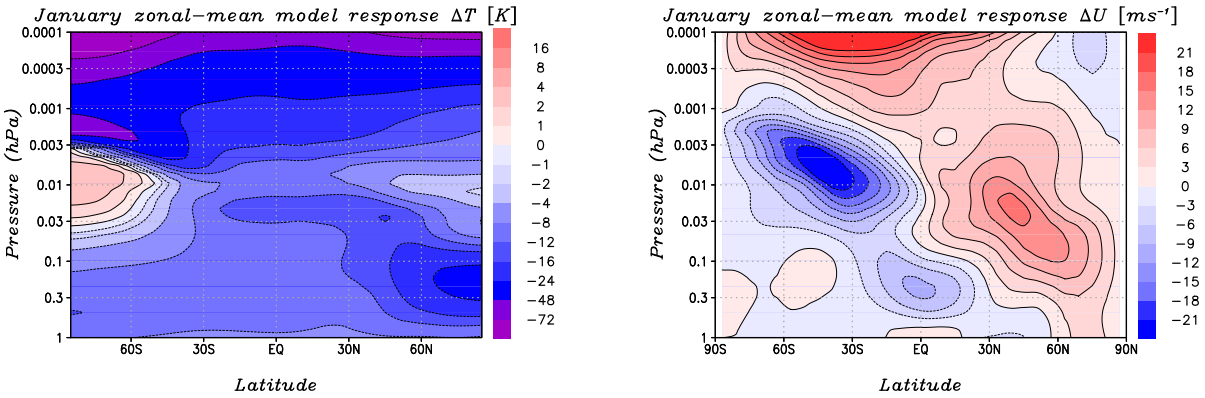

(c)

(d)

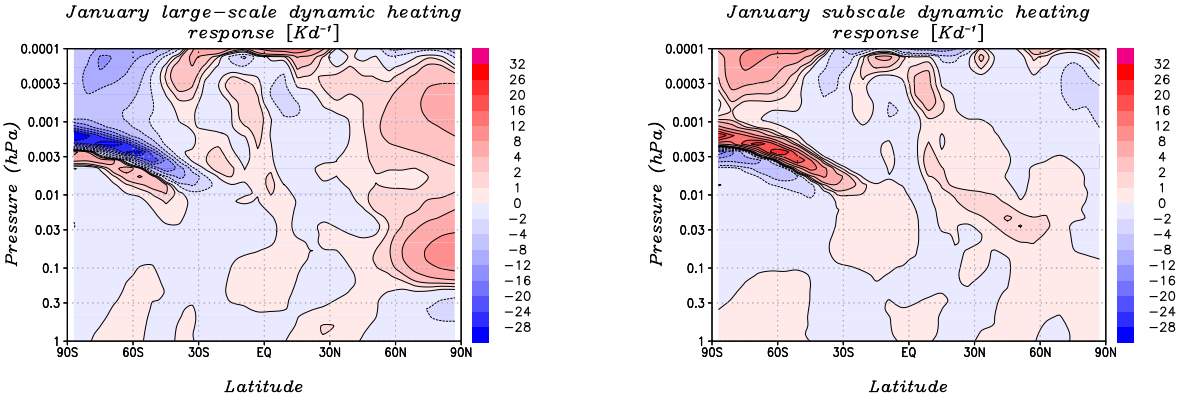

(e)

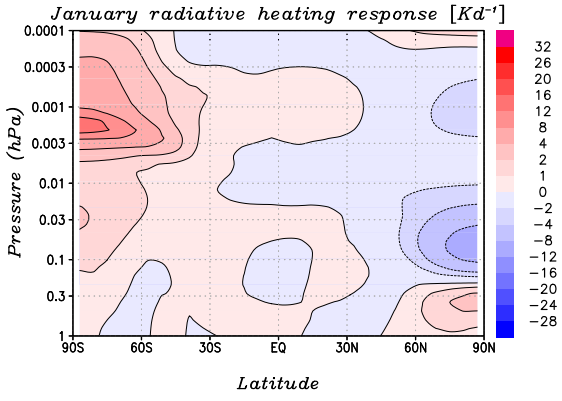

Figure 4.24: Five-year average of the January zonal-mean model response to an increase of CO_2 from 480 ppmv to 960 ppmv for the zonal mean temperature (K) panel (a), the zonal mean wind (ms^{-1}) panel (b), the large scale dynamic heating rate (Kd^{-1}) panel (c), the subscale dynamic heating rate (Kd^{-1}) panel (d), and the radiative heating rate for the CO_2 15μm band (Kd^{-1}) panel (e).

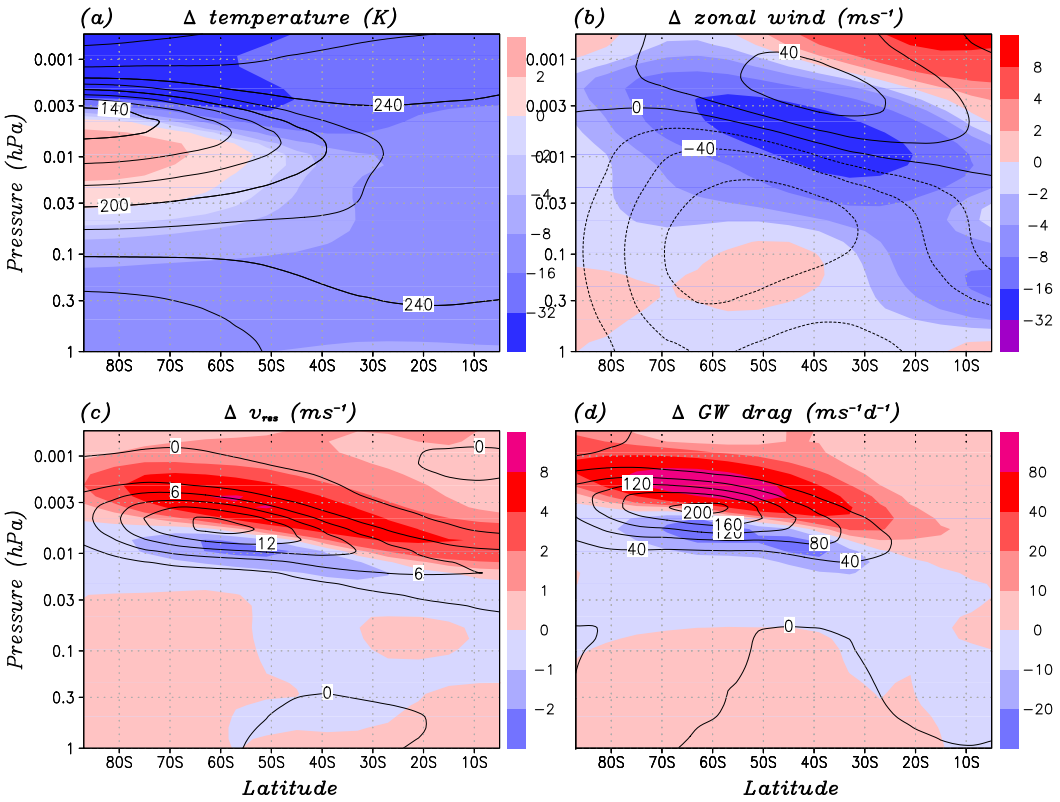

Figure 4.25: Five-year average of the January zonal-mean model response of the southern summer MLT to a doubling of the CO_2 amount from 480 to 960 ppmv. The climatological distribution of the variables plotted is given by the black isolines and the model response is denoted in colors. Panel (a) shows the temperature response and in panel (b) the corresponding change of the zonal wind is displayed. Panels (c) and (d) illustrate the upward shift of the mean meridional circulation as seen in the changes of the residual meridional wind and the gravity wave drag, respectively.

(a) (b)

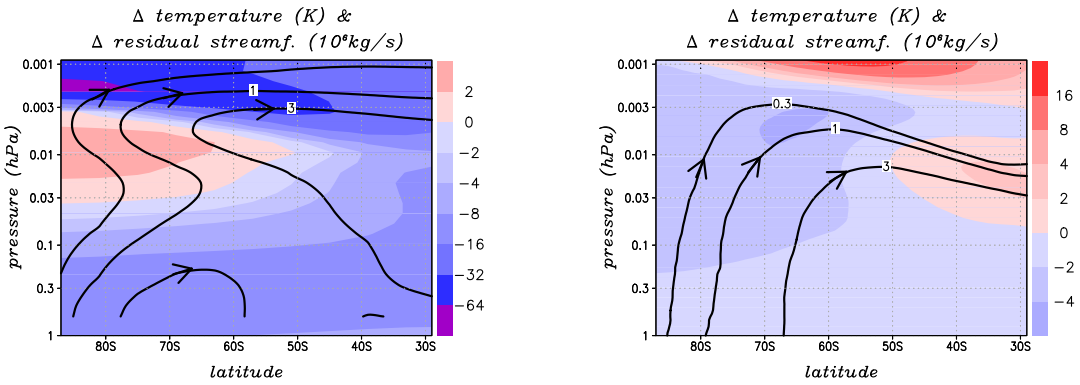

Figure 4.26: (a) Five-year average of the January model response in the summer MLT to an increase of the CO_2 amount from 480 ppmv to 960 ppmv for the zonal mean temperature (K) and the residual steam function (10^9 kg s^{-1}). Panel (b) the same as in panel (a) but with the relaxation temperature held fixed and altered tropospheric gravity wave sources [Becker, 2009].

region considered here counteract each other. The resulting possibility for cancelation of the two effects possibly explains the small temperature changes observed in the vicinity of the summer mesopause [Lübken, 2000; Becker, 2011]. Other processes not discussed here which impact this atmospheric region are for example the interaction between GWs and tides. The asymmetry in the efficiency of Doppler-shifting of GWs by thermal tides leads to a downward shift of the residual circulation and to a warming of the mesopause [Becker, 2011]. Further mechanism affecting the GW driving in the summer MLT result from interhemispheric coupling [Becker and Fritts, 2006; Karlsson et al., 2009] or changes in GW filtering in the stratosphere [Smith et al., 2011].

Chapter 5

Summary

The main purpose of this work was to develop a new continuous radiation scheme of medium complexity for use in a mechanistic atmospheric general circulation model from the surface to the mesopause region. Our method consists of each one set of idealized transfer equations for the long-wave and short-wave regime. These transfer equations extend continuously from the surface up to the lower thermosphere, including deviations from the gray limit and LTE in the long-wave regime, as well as the complete surface energy budget. Our strategy is to account for the fundamental differences between the troposphere and middle atmosphere with regard to the radiative transfer problem in a general and straight-forward fashion, i.e., by one set of transfer equations that holds for the entire altitude range from the surface to the mesopause region. The new scheme was implemented in a mechanistic general circulation model and test simulations with prescribed concentrations of the radiatively active constituents show quite reasonable results.

In Chapter 2 the primitive equations and the radiative transfer equation, which are solved by the mechanistic model, were derived in a unified manner from statistical mechanics and therewith put into a broader theoretical and conceptual framework. Such fundamental considerations as presented there can be useful to extend the physical scope and vertical extent of the model, or to improve existing parameterizations in a consistent manner. In addition the statistical mechanical concepts of TE, LTE, and nonequilibrium, which can be applied to the atmosphere and the radiation field separately, were reviewed and distinguished from the definition of LTE and non-LTE used in radiative transfer calculations. To highlight the specific advantages of the new radiation parameterization developed in this work, a short outline of conventional integral solution methods was presented at the end of Chapter 2.

The technical details of the new radiation scheme were explained in Chapter 3. In the long-wave regime, simple transfer equations for the upward and downward radiative flux densities in broad absorber bands were derived and afterwards integrated numerically in the vertical (over the optical path). The equations invoke the plan-parallel approximation and include isotropic scattering. The dependence on the azimuth angle is neglected and the Eddington approximation is used to parameterize the dependence on the zenith angle. This leads to monochromatic Eddington-type transfer equations. Taking the mean over the frequency bands results in additional covariance terms. These are parameterized applying the Elsasser band model modulated by an arbitrary envelope function for both the extinction coefficient and the spectral energy flux densities. By this method, additional transfer equations for the perturbation radiative fluxes are derived which can be solved along with the frequency-averaged transfer equations. An approximation to the Voigt line width is considered to calculate the grayness parameter [Olivero and Longbothum, 1977]. The temperature-dependent mean band strengths are taken from HITRAN [Rothman et al., 2004] and the correspond-

ing absorber mixing ratios are prescribed. Non-LTE is included by single scattering albedos which are computed from the two-level model for each absorber band, cf. Ch.4.4 in the text of Thomas and Stamnes [2002]. The short-wave radiation is described by simple absorption of the incoming solar radiation in four energetically defined bands. An additional short-wave band contains the energy that is directly transmitted to the surface without loss. This parameterization mimicks absorption of solar radiation by molecular oxygen above the mesopause, by ozone in the stratosphere and around the stratopause, as well as by water vapor in the troposphere.

By performing the numerical integration over the optical path as the last step of our long-wave scheme and introducing all the approximations and simplifications in an analytical fashion first, we easily accommodate all the nonlocal and nonlinear dependencies of the radiative fluxes on the whole atmospheric column. In addition, we avoid the calculation of derivatives of complicated pressure and temperature-dependent flux transmission functions, which govern the heating rate calculations of conventional integral solution approaches, like the Curtis-matrix method for instance [Zhu, 1994]. Furthermore, our new approach to parameterize the frequency variation inside broad absorber bands by some kind of "Reynolds decomposition" and applying the Elsasser band model to achieve a first order closure of the perturbation transfer equations allows us to circumvent further frequency integrations. Using the single scattering albedo as non-LTE parameter that extends over the whole atmospheric column, we don't need to explicitly define appropriate non-LTE source functions [Lopez-Puertas and Taylor, 2001] or to resort to slowly converging iterations between the integrated RTE and statistical equilibrium equations [Wintersteiner et al., 1992; Kutepov et al., 1998]. In particular, we calculate the radiative fluxes continuously from the surface up to the mesopause region. This is presently not done in the comprehensive methods used in other middle atmospheric GCMs [Richter et al., 2008; Garcia et al., 2007; Schmidt et al., 2006; Fomichev et al., 2002; Wehrbein and Leovy, 1982]. Furthermore, we simulate the radiation together with the dynamics and other physical parameterizations with the same spatial and temporal numerical resolutions.

In Chapter 4, results obtained from applying the radiation scheme in the context of a mechanistic general circulation model were presented. The model is characterized by semi-realistic dynamics and a state-of-the-art gravity-wave parameterization for dynamical control of the mesosphere and mesopause region together with a simple parameterization of the orographic gravity-wave drag important in the winter stratosphere. The simulated climatology and variability turns out to be quite reasonable. The radiative heating and cooling rates are comparable to the results of other comprehensive GCMs [Fomichev et al., 2002]. The long-wave radiative fluxes show the expected characteristics, with water vapor absorption and emission mainly relevant in the troposphere, as well as ozone and CO_2 absorption and emission dominating in the stratosphere. The tropospheric greenhouse effect due to our LW absorbers is simulated quite reasonably, showing that water vapor dominates the long-wave downward radiation. Our non-LTE parameterization compares well to results of Dickinson [1984] when we consider the relative source function for the CO_2 15 μm band. Model deficits worth mentioning occur in the polar winter mesosphere, which is too warm and where the dynamically induced stratopause is located too high, and in the lower thermosphere, where the tuned short-wave heating is too weak. The primary benefit of the new formalism in combination with the consistent treatment of all energy conversion processes in the model is a simulation of the atmospheric general circulation up to the mesopause region where the radiation budget at the TOA is balanced in conjunction with a balanced surface energy budget and continuous radiative energy flux densities. Analyzing the global annual-mean energy budget at the TOA and the global annual-mean surface energy budget, our model compares

favorably to other results [Trenberth et al., 2009]. The imbalances in the present simulation amount to an excess of about 0.3 Wm^{-2} at the TOA and 1.4 Wm^{-2} at the surface. The radiation budget at the TOA shows a pronounced annual cycle with maxima of about 3 Wm^{-2} during northern hemisphere (NH) late winter and minima of about -1.8 Wm^{-2} during southern hemisphere (SH) late winter. This annual cycle can possibly be attributed to the north-south asymmetry in the late-winter Rossby-wave activity, which leads to differences in the redistribution of heat from the tropics toward higher latitudes and to a corresponding annual cycle of the tropical lower stratospheric temperature [Yulaeva et al., 1994]. Two offline experiments were analyzed to investigate the sensitivity of the long-wave heating rates to deviations from the gray limit and from LTE. It was shown that deviations from LTE are most important for the CO_2 15 μm band, as expected, and that deviations from the gray limit have the largest impacts again on the CO_2 15 μm band and the water vapor rotation continuum. Doubling the CO_2 amount in the present model setup was shown to lead to a warming of the summer mesopause. Due to the gradient wind balance this results in an anomalous easterly wind component which alters the propagation conditions for GWs and leads to an upward shift of equator ward branch of the residual circulation. This purely radiative effect can, together with the converse impact on the residual circulation of climate change-induced stronger tropospheric GW sources [Becker, 2009], provide a possible explanation for the small long-term temperature changes observed in the vicinity of the summer mesopause [Lübken, 2000; Becker, 2011].

Some additional simplifications and shortcomings of the present radiation scheme and the present model setup should be mentioned. In our clear air calculations of solar radiation, scattering and reflection are neglected. Furthermore, instead of a comprehensive treatment of the effects of clouds [Bergman and Hendon, 1998; Cheng et al., 1999; Khvorostyanov and Sassen, 1998a, b; Lohmann et al., 2007], the present radiation scheme crudely includes only the two main effects: Reflection of solar radiation and LW cooling of the upper troposphere. The first effect is accounted for in terms of an increased surface albedo when compared to other models and measurements [Trenberth et al., 2009] while the LW cooling is represented by a prescribed cooling rate. Note that neglecting the reflection of SW radiation by clouds would lead to a strong overestimation of the surface temperature while omitting the LW cooling would lead to an underestimation of the outgoing LW radiation [Held and Soden, 2000]. The cloud greenhouse effect is not yet taken into account. Therefore, the overall greenhouse effect is possibly underestimated in the present test simulation. Another issue is the large underestimation by a factor ten of the radiative forcing of the troposphere due to doubling the CO_2 amount in the present model (not shown) compared to what is expected from other studies [Held and Soden, 2000]. This deficit can possibly be attributed to the saturation of the very strong absorption lines of this band which lead to deviations from Beer-Bougert-Lamberts law that may not be captured in the treatment of deviations from the gray limit in the present radiation scheme, see for example [Thomas and Stamnes, 2002] p. 388 or [Smith, 2010]. In this context we also emphasize that parameterizing the frequency variation inside a broad long-wave absorber band by the Elsasser band model is a crude approach. A statistical band model like the random Lorentz-Malkmus model would be much more appropriate to describe the frequency variations, cf. chapter 10.3 in the text of Thomas and Stamnes [2002], but it would also render the scheme more complicated. Another simplification of the present radiation scheme is that our short-wave band strengths are just tuning parameters and independent from other variables like temperature for instance. However, a self-consistent calculation from spectroscopic parameters in the short-wave regime, including an appropriate absorption efficiency due to the reduced number of inelastic collisions in the upper atmosphere [Lopez-Puertas and Lopez-Valverde, 1989] is out of the scope of this work. Furthermore,

comparing our global mean short-wave heating rates to London's results, the most noticeable differences to our radiation scheme are 1) the lack of a secondary ozone maximum, responsible for an additional solar ozone heating rate in the mesosphere, 2) the neglect of solar absorption by CO_2, and 3) the weak short-wave heating in the thermosphere. An explanation for and mitigation of these shortcomings is subject to ongoing research.

The proposed mechanistic model concept may be useful in future studies of the climate sensitivity of the middle atmosphere. For this purpose the radiation scheme should be improved and further validated along the lines already mentioned. Furthermore, the model must be completed by an explicit tropospheric hydrological cycle and a realistic distribution of the oceanic heat flux divergence. In addition, transport and chemistry of other minor constituents may be explicitly included. The LW radiative transfer of clouds can be parameterized by including an additional gray band into the LW scheme. Due to the numerical efficiency of our model, it would be possible to run high resolutions that allow us to simulate gravity-wave effects in the middle atmosphere explicitly. Note that this has already been possible with a more simple model setup [Becker, 2009]. The new continuous parameterization of the radiative fluxes will allow to resolve the full nonlinear interaction between gravity waves and the radiation field. Coupled dynamical-radiative processes that extend over the whole atmospheric column will be subject to future applications. In this context, the question of the relative importance of radiative and dynamically induced climate changes in the middle atmosphere will be further investigated. Other possible future applications of the new radiation scheme in the context of the mechanistic model completed by additional physical processes as mentioned above is for example to study the impact of solar variations on the dynamics and the state of the middle atmosphere.

Appendix A

Wave-mean-flow interaction

The wave mean-flow interaction responsible for the observed deviations of the atmosphere from the hypothetical radiatively determined state can be understood considering the transformed Eulerian mean equations (TEM). This set of equations (given in z-coordinates here) is obtained by taking the time and zonal mean of the primitive equations (2.58) and subtracting the quasi-linear Stokes drift from the Eulerian mean meridional and zonal velocities [Andrews et al., 1987]

$$\begin{aligned} \frac{\partial}{\partial t}[u] &= f v_{res} + [q^* v^*] - \frac{1}{\rho_r}\frac{\partial}{\partial z}(\rho_r[\overline{u'w'}]) \\ \frac{1}{\cos\phi}\frac{\partial}{\partial y}(\cos\phi v_{res}) + \frac{1}{\rho_r}\frac{\partial}{\partial z}(\rho_r w_{res}) &= 0 \\ \frac{\partial}{\partial t}[T] &= -\frac{g}{c_p}w_{res} - \frac{[T]-T_e}{\tau} \\ \frac{\partial}{\partial z}[u] &= -\frac{g}{f}\frac{\partial}{\partial y}\left([T]\right). \end{aligned} \tag{A.1}$$

The brackets indicate zonal averaging and stars deviation from the zonal mean. The apostrophe denotes perturbations due to gravity waves and the overbar an average over gravity wave scales, q^* is the wave quasi-geostrophic potential vorticity. The other symbols have their usual meaning. The second and third terms on the right-hand side of the first equation are the zonal mean accelerations resulting from momentum deposition of quasi geostrophic and gravity waves. The effective exchange of tracers and heat between high and low latitudes is given by the closed circulation defined by the residual meridional and vertical velocities v_{res} and w_{res}. The wave driving of this mean meridional circulation can be understood using the following line of arguments. Assuming a hypothetical climatological equilibrium state without any wave activity, the time derivativives and the wave terms in the TEM equations vanish. This implicates that in the zonal momentum equation, the meridional residual velocity v_{res} and due to the continuity equation the vertical residual velocity w_{res} both are zero. Considering the thermodynamic equation, the zonal mean temperature $[T]$ then equals the radiative equilibrium temperature T_e in this situation which is not observed in the atmosphere. Conversely, if atmospheric waves are present (not vanishing momentum deposition terms), they induce a mean residual circulation, as is observed in the real atmosphere. This circulation drives the temperature, and via the thermal wind balance the zonal wind too, away from the hypothetic radiatively determined state.

Considering quasi-geostrophic waves, their momentum deposition can be expressed using

the divergence of the quasi-geostrophic Eliassen-Palm flux $\overrightarrow{EPF}_{qg}$

$$[q^* v^*] = \frac{1}{a\cos\phi}\nabla(\overrightarrow{EPF}_{qg}) = \frac{\left([q^*\delta^*] - \frac{\partial}{\partial t}[\frac{q^{*2}}{2}]\right)}{\frac{\partial}{\partial y}[q]}. \tag{A.2}$$

The Eliassen-Palm flux vector is defined as

$$\overrightarrow{EPF}_{qg} = a\cos\phi\rho_r\left(-[u^* v^*]\vec{e}_y + \frac{c_p f_0}{g}[T^* v^*]\vec{e}_z\right). \tag{A.3}$$

From (A.2) it can be seen that the momentum deposition on the mean flow is zero assuming linear ideal waves propagating conservatively and excluding dissipative damping processes or critical levels (Charney-Draizin Theorem) [Lindzen, 1990].

For hydrostatic, weakly damped mid-frequency gravity waves propagating in a slowly varying background atmosphere

$$f^2 \ll \omega_I^2 = \frac{N^2(k^2+l^2)}{m^2 + 1/(4H^2)} \ll N^2, \tag{A.4}$$

the vertical dependence of the gravity wave flux $\frac{1}{\rho_r}(\rho_r[\overline{u'w'}]) \doteq F(z)$ can be calculated analytically. Here k, l, and m denote the zonal, meridional, and vertical wavenumber respectively, N, H, and ω_I are the buoyancy frequency, the scale height, and the intrinsic frequency of the gravity wave, and ρ_r indicates a reference density profile. Assuming that the mean zonal wind $u(z)$ and the damping α vary only slowly with height (WKB assumption) leads to

$$F(z) = F(z_0)\exp\left\{-\int_{z_0}^{z} 2m_i dz'\right\} \tag{A.5}$$

with

$$F(z_0) = \frac{\rho_0 B^2 N(z_0)}{2k(c-u(z_0))} \tag{A.6}$$

and

$$m_i(z) = \frac{\alpha(z)N(z)}{k(u(z)-c)^2} = \frac{D(z)N(z)^3}{k(u(z)-c)^4}. \tag{A.7}$$

Subscripts $_0$ denote values of the quantities at the launch level of the gravity wave and D is the diffusion coefficient which corresponds to the damping α. For vertically propagating gravity waves, the momentum flux changes with height only if the imaginary part of the vertical wave number $m_i(z)$ does not vanish. The imaginary part of the vertical wavenumber depends on the static stability of the atmosphere $N(z)$, the difference between the zonal background wind and the phase velocity of the wave $U(z) - c$, the presence of irreversible damping processes $\alpha(z)$ (such as momentum diffusion or radiative damping for example) and on the zonal wave number k. In order to give rise to a vertical variation of the gravity wave flux, and therefore to a nonzero momentum deposition on the mean flow, similar preconditions as those implied by the Charney-Draizin theorem for quasi-geostrophic waves must be satisfied.

The filtering of gravity waves by the mean background wind can be understood by considering the real part the vertical wave number (dispersion relation)

$$m_r = \frac{N}{U-c} = \frac{1}{\lambda_z}. \tag{A.8}$$

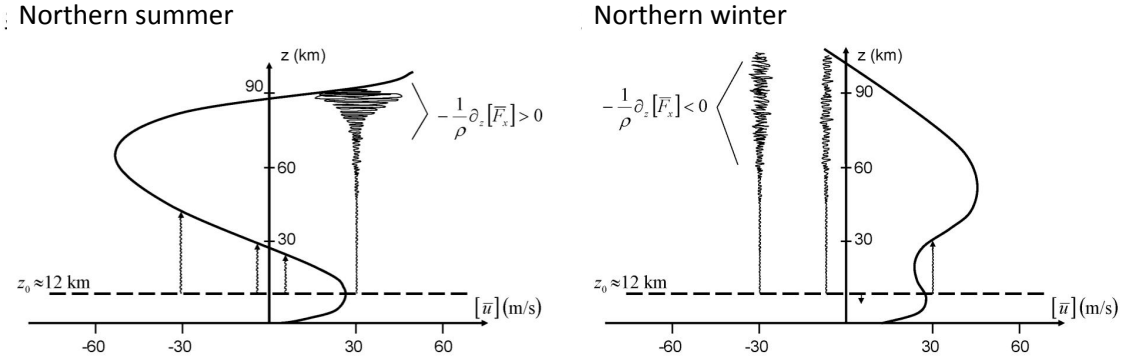

Figure A.1: Wave filtering by the mean background zonal wind according to the disperion relation A.8 for typical norther summer (left) and winter (right) zonal mean wind profiles. In northern summer, only gravity waves with large eastward phase speed propagate into the mesosphere and lead to a reversal of the summer easterlies to westerlies in the mesopause region. Conversely in winter, all of the gravity waves with westward phase velocity can propagate up to the mesopause, where the wind is reversed from westerlies to easterlies. Schematic representation from [Becker, 2011].

For waves approaching a critical level where the background wind U equals the phase speed c, the vertical wavelength λ_z goes to zero and the vertical wave number becomes infinitely large. At such a critical level, the group velocity vanishes and therefore the energy of the wave is completely deposited on the mean flow. A summary of the seasonally varying propagation conditions for gravity waves due to different background wind profiles in the summer and winter hemisphere is illustrated in Figure A.1.

Concerning the amplitudes of vertical propagating gravity waves, they do not just increase exponentially with decreasing density. As can be derived applying the corresponding polarization relations and assuming the WKB approximation, the zonal wind $A_u(z)$, vertical wind $A_w(z)$, and temperature $A_T(z)$ amplitudes of a gravity wave of a certain horizontal wave number k depend strongly on the zonal mean background wind and the static stability of the

atmosphere

$$
\begin{aligned}
A_u(z) &= \frac{N(z)B}{k\sqrt{2(c-U(z_0))}}\,\frac{1}{\sqrt{(c-U(z))}}\sqrt{\frac{\rho_0}{\rho(z)}} \\
A_w(z) &= \frac{B}{\sqrt{2(c-U(z_0))}}\,\sqrt{(c-U(z))}\sqrt{\frac{\rho_0}{\rho(z)}} \\
A_T(z) &= \frac{T(z)N(z)^2B}{gk\sqrt{2(c-U(z_0))}}\,\frac{1}{\sqrt{(c-U(z))}}\sqrt{\frac{\rho_0}{\rho(z)}}.
\end{aligned}
\tag{A.9}
$$

Appendix B

Example of a nonequilibrium emission function

In this section, the method of calculating a nonequilibrium statistical operator described in section 2.2.2 is applied to the radiation field to obtain corrections to Planck's law for thermal emission [Fort et al., 1999b]. The corrected emission function can then be applied to states which deviate not too strongly from thermodynamic equilibrium. Like in the calculation of the equilibrium spectral energy density, the mean total energy of the radiation field is used to constrain the maximization of the information entropy

$$E = \frac{2 \cdot V}{(2\pi\hbar)^3} \int d^3p \, pc \, \langle n_p \rangle. \tag{B.1}$$

Adding the energy flux $\overrightarrow{F}$

$$\overrightarrow{F} = \frac{2 \cdot V}{(2\pi\hbar)^3} \int d^3p \, pc\vec{c} \, \langle n_p \rangle \tag{B.2}$$

and the photon flux

$$\overrightarrow{J_N} = \frac{2 \cdot V}{(2\pi\hbar)^3} \int d^3p \, \vec{c} \, \langle n_p \rangle \tag{B.3}$$

as additional constraints it can be found that the Bose distribution (2.73) must be replaced by [Fort et al., 1999b]

$$\langle n_p \rangle = \frac{1}{\exp\left(\beta\varepsilon_p - \vec{\gamma} \cdot pc\vec{c} + \vec{\delta} \cdot \vec{c}\right) - 1}. \tag{B.4}$$

Here $\vec{\gamma}$ and $\vec{\delta}$ are the additional thermodynamic parameters $F_n(t)$ (Lagrange multipliers) which correspond to the energy flux and the photon flux respectively and $\vec{c}$ is the velocity of light vector.

To evaluate this mean occupation number distribution function for a specific example a box with highly absorbing walls which emit thermal radiation through small apertures at the bottom and the top respectively is considered, see Figure B.1. The temperature inside the cavity is assumed to increase with height. Evaluating (B.4) for this specific example with the aid of the plane-parallel approximation and applying the generally valid relation $I_\nu = \frac{2h\nu^3}{c^2}\langle n_p \rangle$, the intensity of the radiation field can be approximated by the sum of the Planck function plus first $\Phi^{(1)}$ and second $\Phi^{(2)}$ order correction terms (compare [Fort et al., 1999b] for the detailed calculations)

$$I_\nu(z, \vartheta) = B_\nu(T(z)) \left(1 + \Phi^{(1)} \cos\vartheta + \Phi^{(2)} \cos^2\vartheta\right). \tag{B.5}$$

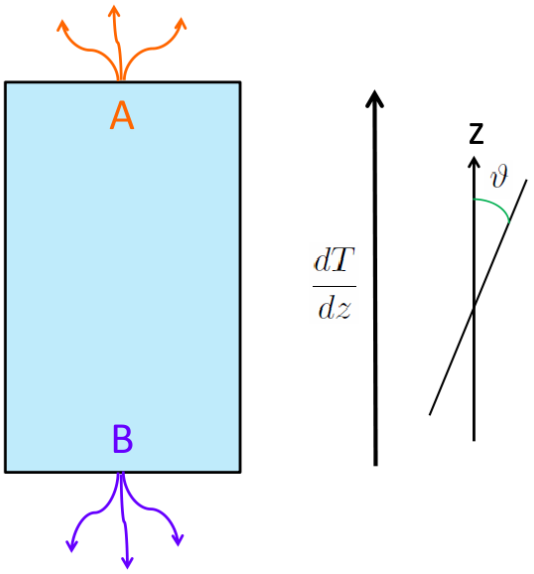

Figure B.1: Schematic to define anisotropic nonequilibrium emission functions [Fort et al., 1999b]. The cavity depicted consist of highly absorbing walls. Radiation is emitted through small apertures at A and B. Temperature increases with height.

ϑ denotes the "zenith" angle. Integration of this intensity over the upper and lower half space respectively leads to an anisotropic thermal emission function composed of an upward (point A in Figure B.1)

$$B_\nu^\uparrow = \pi B_\nu(T(z)) \left(1 + \frac{2}{3}\Phi^{(1)} + \frac{1}{2}\Phi^{(2)}\right) \tag{B.6}$$

and a downward emission part (point B in Figure B.1)

$$B_\nu^\downarrow = \pi B_\nu(T(z)) \left(1 - \frac{2}{3}\Phi^{(1)} + \frac{1}{2}\Phi^{(2)}\right). \tag{B.7}$$

The height dependent correction terms $\Phi^{(1)}$

$$\Phi^{(1)} = -\left\{\left(pc^2 - \frac{18k_BTc\zeta(3)}{\pi^2}\right)\gamma + \frac{9c^2h^3}{8\pi^3k_B^3T^3}J_N\right\}\frac{e^\chi}{e^\chi - 1} \tag{B.8}$$

and $\Phi^{(2)}$

$$\Phi^{(2)} = \left\{\left(pc^2 - \frac{18k_BTc\zeta(3)}{\pi^2}\right)\gamma + \frac{9c^2h^3}{8\pi^3k_B^3T^3}J_N\right\}^2\frac{e^\chi(e^\chi+1)}{2(e^\chi-1)^2} \tag{B.9}$$

in turn depend on the z-component of the heat flux parameter γ

$$\gamma = -\frac{1}{1 - \frac{405}{\pi^6}[\zeta(3)]^2}\frac{1}{\sigma c k_B T^2}\left(\frac{dT}{dz} + \frac{27\zeta(3)\sigma k_B}{2\pi^2 acT^2}J_N\right) \tag{B.10}$$

and the z-component of the photon flux J_N

$$J_N = -\frac{48\zeta(3)k_B^3T^2}{h^3c^2\sigma}\frac{dT}{dz}. \tag{B.11}$$

Here χ is an abbreviation for $e^{\frac{h\nu}{k_BT}}$, a denotes the Stefan Boltzmann constant, σ is the absorption coefficient measured in m^{-1} and $\zeta(3)$ is the Riemann Zeta function. The anisotropic

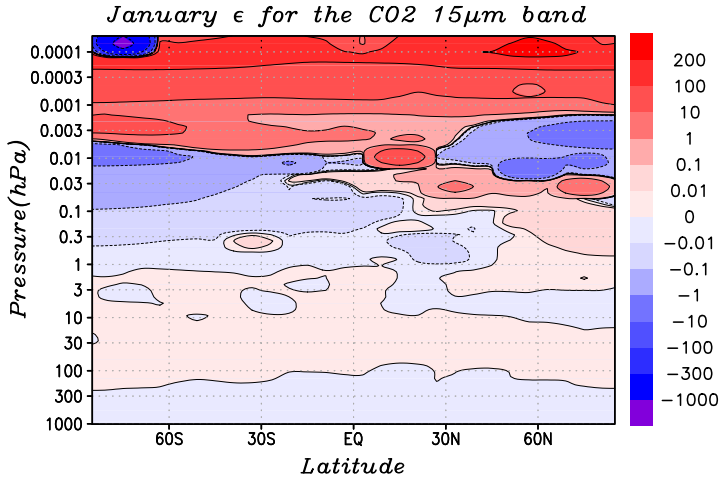

Figure B.2: Criterion (B.12) for the CO_2 15μm band in January. Above the stratopause the corrections to the Planck function (B.6) and (B.7) are not valid due to $|\epsilon| > 0.1$. The data are taken from the same model run which is applied to obtain the results in Chapter 4

emission functions $B_\nu^\uparrow$ and $B_\nu^\downarrow$ therefore depend in addition to temperature on $\frac{dT}{dz}$, and due to the relation $\sigma = \rho\kappa_\nu$ on the air density and the mass absorption coefficient. In order to derive a nonequilibrium emission function by applying just two additional constrains to derive first and second order corrections to the Planck function, the deviations from thermodynamic equilibrium must not be too strong. The following condition must hold for the corrections given above to be applicable [Fort, 1997]:

$$|\epsilon| \doteq |\frac{dT/dz}{T\rho\kappa_\nu}| \ll 1. \tag{B.12}$$

Considering the atmosphere from the surface up to the lower thermosphere this condition is usually not fulfilled, see Figure B.2. To describe the strong deviations from thermal equilibrium observed in the atmosphere, a large number of additional variables A_n and possibly higher order corrections have to be included [Luzzi et al., 1998] which make the approach practically unfeasible.

List of Figures

List of Tables

Bibliography

Andrews, D. G., Holton, J. R., and Leovy, C. B.: Middle Atmosphere Dynamics, International Geophysics Series, Academic Press, 1987.

Batchelor, G. K.: An Introduction to Fluid Dynamics, Cambridge University Press, 2001.

Beagley, S. R., de Grandpre, J., Koshik, H. N., Mc Farlane, N. A., and Shepherd, T. G.: Radiative-Dynamical Climatology of the First-Generation Canadian Middle Atmosphere Model, Atmosphere-Ocean, 35, 293–331, 1997.

Becker, E.: Frictional Heating in Global Climate Models, Monthly Weather Review, 131, 508–520, 2003a.

Becker, E.: Energetics of turbulent momentum diffusion and gravity wave breakdown in general circulation models of the atmosphere, Habilitationsschrift, Universität Rostock, Leibniz Institut für Atmosphärenphysik, Kühlungsborn, 2003b.

Becker, E.: Sensitivity of the upper mesosphere to the Lorenz energy cycle of the troposphere, Journal of Atmospheric Sciences, 66, 647–666, 2009.

Becker, E.: Dynamical control of the middle atmosphere, Space Science Reviews, submitted, 2011.

Becker, E. and Burkhardt, U.: Nonlinear Horizontal Diffusion for GCMs, Monthly Weather Review, 135, 1439–1454, 2007.

Becker, E. and Fritts, D. C.: Enhanced Gravitiy-Wave Activity and Interhemispheric Coupling During MaCWAVE/MIDAS Northern Summer Program 2002, Annales Geophysicae, 24, 1175–1188, 2006.

Becker, E. and McLandres, C.: Consistent Scale Interaction of Gravity Waves in the Doppler Spread Parameterization, Journal of the Atmospheric Sciences, 66, 1434–1449, 2009.

Becker, E. and von Savigny, C.: Dynamical heating of the polar summer mesopause induced by solar proton events, Journal of Geophysical Research, 115, 2010.

Bergman, J. W. and Hendon, H. H.: Calculating Monthly Radiative Fluxes and Heating Rates From Monthly Cloud Observations, Journal of the Atmospheric Sciences, 55, 3471–3491, 1998.

Bönisch, H., Engel, A., Birner, T., Hoor, P., Tarasick, D. W., and Ray, E. A.: On the structural changes in the Brewer-Dobson circulation after 2000, Atmospheric Chemistry and Physics, 11, 3937–3948, 2011.

Callies, U. and Herbert, F.: On thermodynamic evolution criteria with radiation effects of the global climate system, Annales Geophysicae, 6, 645–658, 1988a.

Callies, U. and Herbert, F.: Radiative Processes and Non-Equilibrium Thermodynamics, Journal of Applied Mathematics and Physics, 39, 242–265, 1988b.

Casas-Vazquez, J. and Jou, D.: Temperature in non-equilibrium states: a review of open problems and current proposals, Rep. Prog. Phys., 66, 1937, 2003.

Chandrasekhar, S.: Radiative Transfer, Dover Publicatins Inc. New York, 1960.

Cheng, T., Zhang, Y., and Rossow, W. B.: Sensitivity of Atmospheric Radiative Heating Rate Profiles to Variations of Cloud Layer Overlap, Journal of Climate, 13, 2941–2959, 1999.

Clough, S. A. and Iocono, M.: Line-by-Line calculation of atmospheric fluxes and cooling rates 2. Application to carbon dioxide, ozone, methane, nitrous oxide and halocarbons, Journal of Geophysical Research, 100, 16 519–16 535, 1995.

Clough, S. A., Iacono, M. J., and Moncet, J.-L.: Line-by-Line Calculations of Atmospheric Fluxes and Cooling Rates: Application to Water Vapor, Journal of Geophysical Research, 97, 15 761–15 785, 1992.

Collins, W. D., Rasch, P. J., Boville, B. A., Hack, J. J., McCaa, J. R., Williamson, D. L., Kiehl, J. T., and Briegleb, B.: Description of the NCAR Community Atmosphere Model (CAM3.0), Tech. rep., National Center For Atmospheric Research Boulder Colorado, 2004.

de Groot, S.: Thermodynamik Irreversibler Prozesse, Bibliographisches Institut Mannheim Hochschultaschenbücher-Verlag, 1960.

Dickinson, R. E.: Infrared Radiative Cooling in the Mesosphere and Lower Thermosphere, Journal of Atmospheric and Terrestrial Physics, 46, 995–1008, 1984.

ECMWF: MARS User Guide, European Centre for Medium-Range Weather Forecasts, 2010.

Engel, A., Möbius, T., Bönisch, H., Schmidt, U., Heinz, R., Levin, I., Atlas, E., Aoki, S., Nakazawa, T., Sugawara, S., Moore, F., Hurst, D., Elkins, J., Schauffler, S., Andrews, A., and Boering, K.: Age of stratospheric air unchanged within uncertainties over the past 30 years, Nature Geoscience, 2, 28–31, 2009.

Eu, B. C. and Mao, K.: Kinetic Theory Approach to Irreversible Thermodynamics of Radiation and Matter, Physica A, 180, 65–114, 1992.

Fels, S. B.: A Parameterization of Scale-Dependent Radiative Damping Rates in the Middle Atmosphere, Journal of the Atmospheric Sciences, 39, 1141–1152, 1982.

Fels, S. B.: The Radiative Damping of Short Vertical Scale Waves in the Mesosphere, Journal of the Atmospheric Sciences, 41, 1755–1764, 1984.

Fleming, E., Chandra, S., Barnett, J., and Corney, M.: Zonal mean temperature, pressure, zonal wind and geopotential height as functions of latitude, Adv. Space Res., 10, 11–59, 1990.

Fomichev, V. and Blanchet, J.-P.: Matrix Parameterization of the 15 μm CO2 Band in the Middle and Upper Atmosphere for Variable CO2 Concentration, Journal of Geophysical Research, 103, 11 505–11 528, 1998.

Fomichev, V. I. and Blanchet, J. P.: Development of the New CCC/GCM Longwave Radiation Model for Extension Into the Middle Atmosphere, Atmosphere-Ocean, 33, 513–531, 1995.

Fomichev, V. I. and Shved, G. M.: Net Radiative Heating in the Middle Atmosphere, Journal of Atmospheric and Terrestrial Physics, 50, 671–688, 1988.

Fomichev, V. I. and Shved, G. M.: On the Closeness of the Middle Atmosphere to the State of Radiative Equilibium: An Estimation of Net Dynamical Heating, Journal of Atmospheric and Terrestrial Physics, 56, 479–485, 1994.

Fomichev, V. I., Shved, G. M., and Kutepov, A. A.: Radiative Cooling of the 30-100km Atmospheric Layer, Journal of Atmospheric and Terrestrial Physics, 48, 529–544, 1986.

Fomichev, V. I., Ward, W. E., Beagley, S. R., McLandress, C., McConnell, J. C., McFarlane, N. A., and Shepherd, T. G.: Extended Canadian Middle Atmosphere Model: Zonal-mean climatology and physical parameterizations, Journal of Geophysical Research, 107, ACL9–1 ACL9–16, 2002.

Fomichev, V. I., Jonsson, A. I., deGrandpre, J., Beagley, S. R., McLandress, C., Semeniuk, K., and Shepherd, T. G.: Response of the Middle Atmosphere to CO2 Doubling: Results from the Canadian Middle Atmosphere Model, Journal of Climate, 20, 1121–1144, 2007.

Forster, P., Ramaswamy, V., Artaxo, P., Bernsten, T., Betts, R., Fahey, D., Haywood, J., Lean, J., Lowe, D., Myrhe, G., Nganga, J., Prinn, R., Raga, G., Schulz, M., and Van Dorland, R.: Climate Change 2007: The Physical Science Bases. Contribution of Working Group I to the Fourth Assessment Report of the Intergovernmental Panel on Climate change, chap. Changes in Atmospheric Constituents and in Radiative Forcing, pp. 131–234, Cambridge University Press, Cambridge, United Kingdom and New York, NY, USA, 2007.

Fort, J.: Information-Theoretical Approach to Radiative Transfer, Physica A, pp. 275–300, 1997.

Fort, J.: On the Nonequilibrium Generalization of the Wien Displacement, Physical Letters A, pp. 266–272, 1999a.

Fort, J.: Predictions from Information-Theoretical Models of Nonequilibrium Radiation, Physical Review E, 59, 3710–3713, 1999b.

Fort, J. and Lebot, J. E.: Information-theoretical derivation of an extended thermodynamical description of radiative systems, J.Math.Phys, 39, 345–354, 1998.

Fort, J., Jou, D., and Lebot, J. E.: Measurable temperatures in radiation nonequilibrium systems, Physica A, 248, 97–110, 1998.

Fort, J., Gonzales, J. A., Lebot, J., and Saurina, J.: Information Theory and Blackbody Radiation, Contemporary Physics, 40, 57–70, 1999a.

Fort, J., Jou, D., and Lebot, J.: Temperature and measurement: comparition between two models of nonequilibrium radiation, Physica A, 269, 439–454, 1999b.

Fort, J., Lebot, J. E., and Pujol, T.: Extended Thermodynamics of Heat Transport and Energy Equilibration in Radiation Systems, J.Phys.A: Math.Gen, 32, 3095–3104, 1999c.

Fraedrich, K., Kirk, E., and Lunkeit, F.: Portable University Model of the Atmosphere, Tech. rep., Meteorologisches Institut, Universitt Hamburg, 1998.

Frierson, D. M. W., Held, I. M., and Zurito-Gotor, P.: A Gray-Radiation Aquaplanet Moist GCM. Part1: Static Stability and Eddy Scale, Journal of the Atmospheric Sciences, 63, 2548–2566, 2006.

Frierson, D. M. W., Held, I. M., and Zurito-Gotor, P.: A Gray-Radiation Aquaplanet Moist GCM. Part2: Energy Transport in Altered Climates, Journal of the Atmospheric Sciences, 64, 1680–1693, 2007.

Fritts, D. C. and Alexander, M. J.: Gravity Wave Dynamics and Effects in the Middle Atmosphere, Review of Geophysics, 1, 1–64, 2003.

Garcia, R. R. and Randel, W. J.: Acceleration of the Brewer-Dobson Circulation Due to Increases in Greenhouse Gases, Journal of the Atmospheric Sciences, 65, 2731–2739, 2008.

Garcia, R. R., Marsh, D. R., Kinnison, D., Boville, B. A., and Sassi, F.: Simulation of Secular Trends in the Middle Atmosphere, 1950-2003, Journal of Geophysical Research, 112, 1–23, 2007.

Gerakines, P. A., Schutte, W., Greenberg, J. M., and van Dishoeck, E. F.: The Infrared and Strengths of H2O, CO and CO2 in Laboratory Simulations of Astrophysical Ice Mixtures, Astronomy and Astrophysics, 296, 810–818, 1995.

Gerding, M., Höffner, J., Lautenbach, J., Rauthe, M., and Lübken, F.-J.: Seasonal variation of nocturnal temperatures between 1 and 105 km altitude at 54N observed by lidar, Atmospheric Chemistry and Physics, 8, 7465–7482, 2008.

Grygalashvyly, M., Sonnemann, G. R., and Hartogh, P.: Long-Term Behaviour of the Concentration of the Minor Constituents in the Mesosphere - A Model Study, Atmospheric Chemistry and Physics, 9, 2779–2792, 2009.

Hamilton, K. and Ohfuchi, W.: High Resolution Numerical Modelling of the Atmosphere and Ocean, Springer Verlag, 2008.

Hartmann, D. L.: Global Physical Climatology, vol. 56 of *International Geophysics Series*, Academic Press, 1994.

Haynes, P., Marks, H. J., McIntyre, M. E., Shepherd, T. G., and Shine, K. P.: On the "downward control" of extratropical diabatic circulations by eddy-indued mean zonal forces., Journal of the Atmospheric Sciences, 48, 651–678, 1991.

Held, I. M.: On the Height of the Tropopause and the Static Stability, Journal of the Atmospheric Sciences, 39, 412–417, 1982.

Held, I. M. and Soden, B. J.: Water Vapor Feedback and Global Warming, Annual Reiew of Energy and the Environment, 25, 441–475, 2000.

Held, I. M. and Suarez, M. J.: A Proposal for the Intercomparition of the Dynamical Cores of Atmospheric General Circulation Models, Bulletin of the American Meteorological Society, 75, 1825–1830, 1994.

Held, I. M., Helmer, R. S., and Ramaswamy, V.: Radiative-Convective Equilibrium with Explicit Two-Dimensional Moist Convection, Journal of the Atmospheric Sciences, 50, 3909–2928, 1993.

Herbert, F. and Pelkowski, J.: Radiation and Entropy, Beitr. Phys. Atmos., 63, 134–140, 1990.

Hignett, P., White, A. A., Carter, R. D., Jackson, W. D. N., and Small, R. M.: A Comparition of Laboratory Measurements and Numerial Simulations of Baroclinic Wave Flows in a Rotating Cylindrical Annulus, Quarterly Journal of the Royal Meteorological Society, 111, 131–154, 1985.

Hoffmann, P., Becker, E., Singer, W., and Placke, M.: Seasonal variation of mesospheric waves at norhern middle and high latitudes, Journal of Atmospheric and Solar-Terrestrial Physics, 72, 1068–1079, 2010.

Holton, J. R.: An Introduction to Dynamic Meteorology, vol. 48 of *International Geophysics Series*, Academic Press, 3 edn., 1992.

Imamura, T. and Ogawa, T.: Radiative damping of gravity waves in the terrestrial planetary atmospheres, Geophysical Research Letters, 22, 267–270, 1995.

Jou, D., Casas-Vazquez, J., R.Madureira, J., R.Vasconcellos, A., and Luzzi, R.: Energy Transport in a Mesoscopic Thermo-Hydrodynamics, International Journal of Modern Physics B, 15, 4211–4222, 2001.

Karlsson, B., McLandress, C., and Shepherd, T. G.: Inter-hemispheric mesospheric coupling in a comprehensive middle atmosphere model, Journal of Atmospheric and Solar-Terrestrial Physics, 71, 518–530, 2009.

Khvorostyanov, V. I. and Sassen, K.: Cirrus Cloud Simulation Using Explicit Microphysics and Radiation. Part 1: Model Description, Journal of the Atmospheric Sciences, 55, 1808–1821, 1998a.

Khvorostyanov, V. I. and Sassen, K.: Cirrus Cloud Simulation Using Explicit Microphysics and Radiation. Part 2: Microphysics, Vapor and Ice Mass Budgets, and Optical and Radiative Properties, Journal of the Atmospheric Sciences, 55, 1822–1845, 1998b.

Körnich, H., Schmitz, G., and Becker, E.: The Role of Stationary Waves in the Maintenance of the Northern Annular Mode as Deduced From Model Experiments, Journal of the Atmospheric Sciences, 63, 2931–2947, 2006.

Koshyk, J. N. and Hamilton, K.: The Horizontal Kinetic Energy Spectrum and Spectral Budget Simulated by a High-Resolution Troposphere-Stratosphere-Mesosphere GCM, Journal of the Atmospheric Sciences, 58, 329–348, 2000.

Kutepov, A. A., Gusev, O. A., and Ogibalov, V. P.: Solution of the non-LTE Problem for the Molecular Gas in Planetary Atmospheres: Superiority of the Accelerated Lambda Iteration, Journal of Quantitative Spectroscopy and Radiative Transfer, 60, 199–220, 1998.

Landau, L. D. and Lifschitz, E. M.: Lehrbuch der Theoretischen Physik III Quantenmechanik, Akademie-Verlag Berlin, 1979.

Landau, L. D. and Lifschitz, E. M.: Hydrodynamik, Prof. Dr. habil. Wolfgang Weller, 1986.

Landau, L. D. and Lifschitz, E. M.: Lehrbuch der theoretischen Physik 1 Mechanik, Wissenschaftlicher Verlag Harri Deusch, 14 edn., 2004.

Landsberg, P.: Thermodynamic Energy Conversion Efficiency, Journal of Applied Physics, 51, R1–R20, 1980.

Lindzen, R. S.: Dynamics in Atmospheric Physics, Cambridge University Press, 1990.

Liou, K. N.: An Introduction to Atmospheric Radiation, vol. 84 of *International Geophysics Series*, Academic Press, 2002.

Lohmann, U., Stier, P., Hoose, C., Ferrachat, S., E., R., and Zhang, J.: Cloud Microphysics and Aerosol Indirect Effects in the Global Climate Model ECHAM5-HAM, Atmos.Chem.Phys, 7, 3425–3446, 2007.

London, J.: Radiative Energy Sources and Sinks in the Stratosphere and Mesosphere, Atmos.Ozone.Proc, pp. 703–721, 1980.

Lopez-Puertas, M. and Lopez-Valverde, M. A.: Studies of Solar Heating by CO2 in the Upper Atmosphere Using a Non-LTE Model and Satellite Data, Journal of the Atmospheric Sciences, 47, 809–922, 1989.

Lopez-Puertas, M. and Taylor, F. W.: Non-LTE Radiative Transfer in the Atmosphere, vol. 3 of *Series on Atmospheric, Oceanic and Planetary Physics*, World Scientific Singapore, 2001.

Lopez-Puertas, M., Zaragoza, G., Lopez-Valverde, M., Martin-Torres, F., Shved, G., Manuilova, R., Kutepov, A., Gusev, O., von Clarmann, T., Linden, A., Stiller, G., Wegner, A., Oelhaf, H., Edwards, D., and Flaud, J.-M.: Non-Loal Thermodynamic Equilibtium Limb Radiances for the MIPAS Instrument on ENVISAT-1, Journal of Quantitative Spectroscopy and Radiative Transfer, 59, 377–403, 1998.

Lorenz, E. N.: Deterministic Nonperiodic Flow, Journal of the Atmospheric Sciences, 20, 130–141, 1963.

Lorenz, E. N.: The Nature and Theory of the General Circulation of the Atmosphere, 218, WMO Publication, 1964.

Lübken, F.-J.: Nearly zero temperature trend in the polar summer mesosphere, Geophysical Research Letters, 27, 3603–3606, 2000.

Luzzi, R., Vasconcellos, A. R., Casas-Vazquez, J., and Jou, D.: Characterization and Measurement of Nonequilibrium Temperature-Like Variables in Irreversible Thermodynamics, Physica A, pp. 699–714, 1997a.

Luzzi, R., Vasconcellos, A. R., Jou, D., and Casas-Vazquez, J.: Thermodynamic variables in the context of a nonequilibrium statistical ensemble approach, Atm.Chem.Phys., 107, 7383–7396, 1997b.

Luzzi, R., Vasconcellos, A. R., Casas-Vazquez, J., and Jou, D.: On the Selection of the State Space in Nonequilibrium Thermodynamics, Physica A, 248, 111–137, 1998.

Madureira, J. R., Vasconcellos, A. R., and Luzzi, R.: A Nonequilibrium Statistical Grand-Canonical Enesmble: Description in Terms of Flux Operators, Journal of Chemical Physics, 109, 2099–2110, 1998.

Manuilova, R. O., Gusev, O. A., Kutepov, A. A., von Clarmann, T., Oelhaf, H., Stiller, G. P., Wegner, A., Lopez-Puertas, M., Martin-Torres, F. J., Zaragoza, G., and Flaud, J. M.: Modelling of Non-LTE Limb Spectra of i.r.Ozone Bands for the MIPAS Space Experiment, Journal of Quantitative Spectroscopy and Radiative Transfer, 59, 405–422, 1998.

McLandress, C., Ward, W. E., Fomichev, V. I., Semeniuk, K., Beagley, S. R., McFarlane, N. A., and Shepherd, T. G.: Large Scale Dynamics of the Mesosphere and Lower Thermosphere: An Analysis Using the Extended Canadian Middle Atmosphere Model, Journal of Geophysical Research, 111, D17 111(1)–D17 111(16), 2006.

Mlawer, E. J., Taubman, S. J., Brown, P. D., Iacono, M. J., and Clough, S. A.: Radiative transfer for inhomogenous atmospheres RRTM, a validated correlated-k model for the longwave, Journal of Geophysical Research, 102, 16 663–166 682, 1997.

Nolting, W.: Grundkurs Theoretische Physik 6 Statistische Mechanik, Springer Verlag, 2004.

Oeberg, K. I., Fraser, H. J., Boogert, A. A. C., Bisschop, S. E., Fuchs, G. W., van Dishoeck, E. F., and Linnartz, H.: Effects of CO2 on H2O Band Profiles and Band Strengths in Mixed H2O:CO2 Ices, Astronomy and Astrophysics, 462, 1187–1198, 2007.

Olivero, J. J. and Longbothum, R. L.: Empirical Fits to the Voigt Line Width: A Brief Review, Journal of Quantitative Spectroscopy and Radiative Transfer, 17, 233–236, 1977.

Phillips, N. A.: The equations of motion for a shallow rotating atmosphere and the "traditional approximation", Journal of the Atmospheric Sciences, 23, 626–628, 1966.

Phillips, N. A.: Principles of large scale numerical weather prediction, Reidel Publishing Company, 1973.

Pichler, H.: Dynamik der Atmosphäre, B.I.- Wissenschaftsverlag, Zürich, 1986.

Ramos, J., R.Vasconcellos, A., and Luzzi, R.: A Nonequilibrium Ensemble Formalism: Criterion for Truncation of Description, Physica A, 112, 2692 2700, 2000.

Richter, J. H., Sassi, F., Garcia, R. R., Matthes, K., and Fischer, C. A.: Dynamics of the Middle Atmosphere as Simulated by the Whole Atmosphere Community Model, Version 3(WACCM3), Journal of Geophysical Research, 113, 1–21, 2008.

Roeckner, E., Buml, G., Bonaventura, L., Brokopf, R., and Esch, M.: The atmospheric general circulation model Echam5 Part I, Model description, Tech. Rep. 349, Max-Planck-Institut für Meteorologie Hamburg, 2003.

Röpke, G.: Quantenphysik, VEB Deutscher Verlag der Wissenschaften, 1983.

Röpke, G.: Statistische Mechanik für das Nichtgleichgewicht, Deutscher Physik Verlag, 1987.

Rothman, L., Gordon, I. E., Barbe, A., Benner, C. D., Bernath, P. F., Birk, M., Boudom, V., Brown, L. R., Campargue, A., Cjampion, J. P., Chance, K., Coudert, L. H., Dana, V., Devi, V. M., Fally, S., Flaud, J. M., Gamache, R. R., Goldman, A., Jacquemart, D., Kleiner, I., Lacome, N., Lafferty, W. J., Mandin, J. Y., Massie, S. T., Mikhailenko, S. N., Miller, C. E., Moazzen-Ahmadi, N., Naumenko, A. V., Nikitin, J., Orphal, J., Perevalov, A. Predio-Cross, A., Rinsland, C. P., Rotger, M., Simeckova, M., Smith, M. A. H., Sung, K., Tashkun, J. T., Toth, R. A., Vandaele, A. C., and Vander Auwera, J.: The HITRAN 2008

Molecular Spectroscopic Database, Journal of Quantitative Spectroscopy and Radiative Transfer, 110, 533–572, 2009.

Rothman, L. S., Rinsland, C. P., Goldman, A., Massie, S. T., Edwards, D. P., Flaud, J. M., Perrin, A., Camy-Peyret, C., Dana, V., Mandin, J. Y., Schroeder, J., McCann, A., Gamache, R. R., Wattson, R. B., Yoshino, K., Chance, K. V., Jucks, K. W., Brown, L. R., Nemtchinov, V., and Varanasi, P.: The HITRAN Molecular Spectroscopic Database and HAWKS (HITRAN ATMOSPHERIC WORKSTATION) 1996 Edition, Journal of Quantitative Spectroscopy and Radiative Transfer, 60, 665–710, 1998.

Rothman, L. S., Jacquemart, D., Barbe, A., Benner, C. D., Birk, M., Brown, L. R., Carleer, M. R., C., C. J., Chance, K., Coudert, L. H., Dana, V., Devi, V. M., Flaud, J. M., Gamache, R. R., Goldman, A., Hartmann, J. M., Jucks, K. W., Maki, A. G., Mandin, J.-Y., Massie, S. T., Orphal, J., Perrin, A., Rinsland, C. P., Smith, M. A. H., Tennyson, J., Tolchenov, R. N., Toth, R. A., Vander Auwera, J., Varanasi, P., and Wagner, G.: The HITRAN 2004 molecular spectroscopic database, Journal of Quantitative Spectroscopy and Radiative Transfer, 96, 139–204, 2004.

R.Vasconcellos, A., J.Fort, D.Jou, and Luzzi, R.: Thermodynamics of Nonequilibrium Radiation (II). Irreversible Evolution and Experimental Setup, Physica A, 300, 403–416, 2001.

Schmidt, H., Brasseur, G. P., Charron, M., Manzini, E., Giorgetta, M. A., Diehl, T., Fomichev, V. I., Kinnison, D., Marsh, D., and Walters, S.: The Hammonia Chemistry Climate Model: Sensitivity of the Mesopause Region to the 11-Year Solar Cycle and CO2 Doubling, Journal of Climate - Special Section, 19, 3903–3931, 2006.

Schunk, R. W. and Nagy, A. F.: Ionospheres: Physics, Plasma Physics and Chemistry, Cambridge Atmospheric and Space Science Series, Campridge University Press, 2001.

Scinocca, J. F. and McFarlane, N. A.: The Variability of Modelled Tropical Precipitation, Journal of the Atmospheric Sciences, 61, 1993–2015, 2004.

Semeniuk, K. and Shepherd, T. G.: The Middle Atmosphere Hadley Circulation and Equatorial Inertial Adjustment, Journal of the Atmospheric Sciences, 58, 3077–3096, 2001.

Semeniuk, K. and Shepherd, T. G.: The Effect of Non-Uniform Radiative Damping on the Zonal-Mean Dynamics of the Extratropical Middle Atmosphere, Quarterly Journal of the Royal Meteorological Society, 128, 259–284, 2002.

Serin, J.: Mathematical Principles of Classical Fluid Mechanics, Springer Verlag, 1959.

Serrin, J.: Encyclopedia of Physics, chap. Mathematical Principle of Classical Fluid Mechanics, pp. 125–262, Springer Verlag, 1959.

Shaw, T. A. and Shepherd, T. G.: Angular Momentum Conservation and Gravity Wave Drag Parameterization: Implications for Climate Models, Journal of the Atmospheric Sciences, 64, 190–203, 2007.

Shepherd, T. G. and McLandress, C.: A Robust Mechanism for Strengthening of the Brewer-Dobson Circulation in Response to Climate Change: Critical-Layer Control of Subtropical Wave Breaking, Journal of the Atmospheric Sciences, 68, 784–797, 2010.

Shine, K. P.: The middle atmosphere in the absence of dynamical heat fluxes, Q.J.R. Meteorol. Soc., 113, 603–633, 1987.

Simeckova, M., Jacquemart, D., Rothman, L. S., Gamache, R. R., and Goldman, A.: Einstein A-Coefficients and Statistical Weights for Molecular Absorption Transitions in the HITRAN Database, Journal of Quantitative Spectroscopy and Radiative Transfer, 98, 130–155, 2006.

Simmons, A. J. and Burridge, D. M.: An Energy and Angular-Momentum Conserving Vertical Finite-Difference Scheme and Hybrid Vertical Coordinates, Monthly Weather Review, 109, 758–766, 1981.

Smith, A. K., Garcia, R. R., Marsh, D. R., and Rihter, J. H.: WACCM simulations of the mean circulation and trace species transport in the winter mesosphere, Journal of Geophysical Research, 999, 1–2, 2011.

Smith, D. C.: Line by Line Analysis of Carbon Dioxide Absorption for Predicting global Warming, AGU Fall Meeting Abstracts, pp. B690+, provided by the SAO/NASA Astrophysics Data System, 2010.

Thomas, G. E. and Stamnes, K.: Radiative Transfer in the Atmosphere and Ocean, Cambridge Atmospheric and Space Science Series, Cambridge University Press, 2002.

Tiedke, M.: Parameterization of Cumulus Convection in Large-Scale Models, in: Physically-Based Modelling and Simulation of Climate and Climate Change-Part I, pp. 375–431, Kluwer Academic Publishers, 1988.

Trenberth, K. E.: Using Atmospheric Budgets as a Constraint on Surface Fluxes, Journal of Climate, 10, 2796–2809, 1997.

Trenberth, K. E., Fasullo, J. T., and Kiel, J.: Earth Global Energy Budget, Bulletin of the American Meteorological Society, 90, 311–323, 2009.

Vasconcellos, A. R., Luzzi, R., and Lebot, G.: Heat Transport in a Boson System: An Information-Theoretical Approach, Physical Review E, 54, 4738–4747, 1996.

Vasconcellos, A. R., Fort, J., Jou, D., and Luzzi, R.: Thermodynamics of Nonequilibrium Radiation (I). General Theory, Physica A, 300, 386–402, 2001.

Vasconcellos, A. R., Ramos, J., and Luzzi, R.: Ensemble Formalism for Nonequilibrium Systems and an Associated Irreversible Statistical Thermodynamics, Brazilian Journal of Physics, 35, 689–717, 2005.

Wehrbein, W. M. and Leovy, C. B.: An Accurate Radiative Heating and Cooling Algorithm for Use in a Dynamical Model of the Middle Atmosphere, Journal of the Atmospheric Sciences, 39, 1532–1544, 1982.

Wintersteiner, P. P., Picard, R. H., Sharma, R. D., Winik, J. R., and Joseph, R. A.: Line by Line Radiative Excitation Model for the Non-Equilibrium Atmosphere: Application to the CO2 15μm Emission, Journal of Geophysical Research, 97, 18 083–18 117, 1992.

Yulaeva, E., Holton, J. R., and Wallace, J. M.: On the Cause of the Annual Cycle in Tropical Lower-Stratospheric Temperatures, Journal of the Atmospheric Sciences, 51, 169–174, 1994.

Zee, A.: Quantum Field Theory in a Nutshell, Princeton University Press, 2003.

Zhu, X.: Radiative Damping Revisited: Parameterization of Damping Rate in the Middle Atmosphere, Journal of the Atmospheric Sciences, 50, 3008–3021, 1993.

Zhu, X.: An Accurate and Efficient Radiation Algorithm for Middle Atmosphere Models, Journal of the Atmospheric Sciences, 51, 3593–3614, 1994.

Zhu, X. and Strobel, D. F.: Radiative Damping in the Upper Mesosphere, Journal of the Atmospheric Sciences, 48, 184–199, 1991.